Aerodynamics, Aeroelasticity, and Stability of Hang Gliders - Experimental Results

Ilan M. Kroo

April 1981

NASA

National Aeronautics and
Space Administration

Aerodynamics, Aeroelasticity, and Stability of Hang Gliders - Experimental Results

Ilan M. Kroo, Stanford University, Stanford, California

and

Ames Research Center, Moffett Field, California

NASA

LIST OF SYMBOLS

A cross-sectional area

AR aspect ratio, $\dfrac{b^2}{S}$

b span

C_D drag coefficient, $\dfrac{drag}{qS}$

$C_{D_{min}}$ minimum C_D

C_{D_o} C_D at zero lift

C_L lift coefficient, $\dfrac{lift}{qS}$

C_{L_o} C_L at which C_D is minimum

C_ℓ rolling-moment coefficient, $\dfrac{rolling\ moment}{qSb}$

C_m pitching-moment coefficient, $\dfrac{moment}{qS}$

C_n yawing-moment coefficient, $\dfrac{yawing\ moment}{qSb}$

C_y side-force coefficient, $\dfrac{side\ force}{qS}$

$\bar{c}$ mean geometric chord, $\dfrac{S}{b}$

c_r root chord

d diameter

E Young's modulus

f equivalent flat-plate drag area

k constant in 3-parameter drag polar

ℓ characteristic length

MAC mean aerodynamic chord, $\dfrac{2}{S}\displaystyle\int_0^{b/2} c^2 dy$

q   dynamic pressure, $\frac{1}{2} \rho V^2$

Re   Reynolds number, $\frac{\rho V \ell}{\mu}$

S   planform area

T   tension

V   tunnel airspeed

α angle of attack (measured with respect to keel)

β angle of sideslip

ϵ strain

Λ sweep angle

λ taper ratio, $\dfrac{c_{tip}}{c_r}$

ρ air density

σ stress

Subscripts:

B   body axis system (fig. 66)

S   stability axis system (fig. 65)

W   wind axis system (fig. 10)

c/4   quarter-chord line

f   full-scale value

l.e.   leading edge

m   model value

p   rate of change with roll rate

α rate of change with α

β rate of change with β

AERODYNAMICS, AEROELASTICITY, AND STABILITY OF HANG GLIDERS —

EXPERIMENTAL RESULTS*

Ilan M. Kroo**

Ames Research Center

SUMMARY

One-fifth-scale models of three basic ultralight glider designs were tested in a 2- by 3-m (7- by 10-ft) wind tunnel at Ames Research Center. The models were constructed to simulate the elastic properties of full-scale gliders and were tested at Reynolds numbers close to full-scale values (1.0×10^6 to 5.0×10^6). Twenty-four minor modifications were made to the basic configurations in order to evaluate the effects of twist, reflex, dihedral, and various stability enhancement devices. Longitudinal and lateral data were obtained at several speeds through an angle of attack range of -30° to +45° with sideslip angles of up to 20°.

Modern glider configurations exhibit much more stable and linear pitching-moment characteristics than the early "Rogallo designs" which are shown to have potentially dangerous characteristics at low angles of attack. The importance of vertical center of gravity displacement is discussed. Large destabilizing moments at negative angles of attack associated with low center of gravity contribute to the possibility of tumbling.

Lateral data indicate that effective dihedral is lost at low angles of attack for nearly all of the configurations tested. The appearance of lateral data depends greatly on the chosen reference axis system for these gliders which operate at unusually large angles of attack, hence demonstrating the need for a dynamic analysis.

Drag data suggest that lift-dependent viscous drag is a large part of the glider's total drag as is expected for thin, cambered sections at these relatively low Reynolds numbers.

**Research Assistant, Department of Aeronautics and Astronautics, Stanford University.

INTRODUCTION

In the last 10 years hang gliding has evolved from an obscure sport to a popular, world-wide activity with some 40 glider manufacturing corporations and with participants numbering in the tens of thousands. Performance gains have made possible 150-km (100-mile) flights at altitudes up to 6,000 m (19,000 ft) and multihour flights are now common. The requirements associated with performance, stability, and controllability have become more demanding as thermal soaring and limited aerobatic maneuvers have replaced the original short glides from sand dunes.

These requirements have been met largely by a design evolution based on trial and error rather than conventional analytical and wind-tunnel work. Although the results of NASA wind-tunnel studies of the Rogallo wing (refs. 1-8) in the 1960's could be used to obtain some idea of the characteristics of older hang glider designs, relatively little accurate data exist on the aerodynamic properties of modern gliders which bear little resemblance to the original Rogallo designs. Hence, most of the analytical work which has been done on glider dynamics is based on unrepresentative data. Only in the last 2 years have data from contemporary designs become available. The data base remains extremely limited despite the need for a quantitative understanding of the properties of these aircraft to increase their performance and safety.

In 1979, NASA-supported work (under grant NSG-2359) began on a program of research aimed at the development of quantitative tools to be used in predicting the aerodynamic characteristics of these ultralight gliders and assisting in their design (ref. 9). The investigation consists of two closely related phases:

1) Wind-tunnel studies of elastically-scaled models.

2) Development of analytical methods to predict the aerodynamic and structural properties of modern hang glider designs.

The empirical results will be used in verification and refinement of the analytical work to allow development of an analysis method with a broad range of applicability. The results also make it possible to identify design variables which are effective in improving the controllability and performance of these gliders. This report details the first portion of this work which was conducted in the Army Aeromechanics Laboratory 7- by 10-ft Wind Tunnel No. 2 at Ames Research Center. The assistance of personnel associated with this facility is gratefully acknowledged. Many useful suggestions have been provided by members of the project Advisory Committee, whose help is also greatly appreciated: Dr. Holt Ashley (faculty advisor), Mr. Donald Ciffone (technical monitor), Dr. Robert Ormiston, Mr. Gary Valle, Dr. Robert Jones, Dr. W. Hewitt Phillips, Dr. Paul MacCready, and Dr. Peter Lissaman.

TESTING PROCEDURE

Model Construction

Scaling- Unavailability of large-scale wind-tunnel facilities dictated the use of scale models rather than actual production gliders. To properly duplicate the aerodynamic characteristics of the full-scale aircraft, it is necessary that these models operate at the same Reynolds number and remain geometrically similar under corresponding loads. Reynolds number equivalence is especially important if the rather complex separated-flow effects, apparent at higher angles of attack and sideslip, are to be simulated. Recent experimental investigations (refs. 10-12) have demonstrated the importance of elastic scaling. The flight characteristics of this type of glider have been shown to vary considerably with changes in loading. This is caused by the flexibility of the frame and deformation of the fabric sail, which necessitates accurate modeling of the elastic properties in addition to geometric and aerodynamic similarity.

These combined requirements place severe constraints on model construction. Since available wind tunnels operate at essentially sea-level conditions, it follows that any resultant force F_m experienced by the glider model must equal the corresponding F_f at full scale. Force equality can be reasoned from the fact that

$$Re_m = Re_f$$

where the product of speed and typical length, $v\ell$, must be the same at both scales. With air densities

$$\rho_m = \rho_f$$

and forces proportional to $\rho V^2 \ell^2$ then

$$F_m = F_f$$

The combination of equal force and equal strain requirements leads to difficulties in the construction of elastically scaled models. If the leading edges of both model and full-scale gliders are constructed of tubes with circular cross sections of radius r proportional to l for aerodynamic similarity, the strain in these tubes is proportional to Fr^2/EI, with EI the familiar bending rigidity. The severe requirement on model construction is to ensure that

$$\left(\frac{r^2}{EI}\right)_m = \left(\frac{r^2}{EI}\right)_f$$

If the same construction and material were employed on the model one would have

$$\left(\frac{r^2}{EI}\right)_m = \left(\frac{\ell_f}{\ell_m}\right)^2 \left(\frac{r^2}{EI}\right)_f$$

This factor of 25 at one-fifth scale is quite unacceptable. Since weight is not believed to be a very significant factor, the situation can be alleviated with the use of solid rods of stiffer material on the model. Models constructed of steel in this manner approach the desired stiffness:

$$\left(\frac{r^2}{EI}\right)_m = 3.4 \left(\frac{r^2}{EI}\right)_f$$

The requirement of equal strains, therefore, can be met by allowing larger-than-scale rod diameters or by some relaxing of the Reynolds number requirement. If the rod diameters are geometrically scaled, a reduction in Reynolds number by approximately 0.54 is required.

Scaling of cables to simulate aerodynamic and structural properties of the full-scale glider is more difficult. Geometrically similar model cables would have a cross-sectional area 1/25 times that of the full-scale model, whereas (if the Reynolds number were reduced as above) the forces they experience would be lower by a factor of 3.4. To duplicate the stretching of the cables, then, the requirement is that

$$\epsilon = \frac{\sigma}{E} = \frac{T}{EA} \propto \frac{T}{d^2 E}$$

$$\frac{d_m}{d_f} = \frac{1}{\sqrt{3.4}} = 0.54$$

Since full-scale cables are nominally 3.2 mm (0.125 in.), adequate model structural strength as well as simulated cable stretching will be ensured if 1.6-mm (0.063-in.) cables are used. If the cables were geometrically scaled, they would be 0.6 m (0.025 in.) in diameter. Hence, an artificially high drag is produced. It is believed that the larger cables substantially affect only the drag measurements, which may be corrected accordingly.

Further difficulties associated with elastic scaling include properly modeling the cable attachments and sail stretching. Small differences in attachment geometry (absence of stainless-steel thimbles) lead to some modeling discrepancies. Exact modeling of sail stretching is also difficult. It requires special tightly-woven fabric, stiff thread, and scaled stitching. Simultaneous scaling of sail tensile properties and bending rigidity requires the selection of a material with proper values of Young's modulus and thickness. If sail material is used (fixed E), the thickness required to duplicate stretching varies with the inverse of the scale factor. This results in a very thick sail with larger-than-scale bending rigidity. Preliminary

4

analysis showed that for the models tested the contribution of sail stretching to the overall deformation would be small [at q = 480 N/m^2 (10 lb/ft^2) elongations of 0.4% for the standard and 1.4% for the low-billow models were predicted] — 3.8-oz. Dacron sail cloth was selected for use on the glider models as a compromise based on required strength, elasticity, and bending rigidity. No attempt was made to simulate the mass properties of the sail material.

Although some discrepancies existed in modeling the elastic properties of the full-scale glider, the predominant elastic deformations associated with leading-edge bending were modeled carefully. Further details of model construction are shown in figures 1-4.

Model configurations- A wide variety of hang glider designs are common today. It is no longer possible to test a "standard" configuration and use the results to predict universal characteristics for these aircraft. However, sufficient similarity does exist so that certain characteristics may be determined from tests on a small group with different but carefully selected geometries.

In particular, the effect of various modifications including fixed-twist ribs (fig. 5), luff lines (fig. 6), and keel pockets (fig. 7) as well as the effects of batten flexibility, dihedral, and sweep were investigated.

Three basic models were constructed with projected planforms shown in figures 2-4. The first model is a "standard Rogallo" configuration, representative of the early hang glider designs. This model was selected primarily because of the relatively large amount of full-scale data which exist for this configuration. Results from the present investigation could be compared with previous studies to verify the basic techniques used in the reduced-scale tests.

The second mo'el is most representative of present glider designs, and a majority of the data were obtained with this model. The third configuration was tested to obtain a better idea of the effects of sweep on hang glider designs. A summary of the basic model geometric properties is included in figures 2-4. A total of 27 different configurations were tested and are summarized in table 1.

Balance and Support System

The model support system permitted an angle-of-attack range of +45° to -30° (see figs. 8, 9). The model was supported in three places: the pilot attachment point at the apex of the triangular control frame and at each end of the horizontal segment of the frame (control bar). Angle-of-attack changes were made by rotating the model about an axis just below the control bar. This placed the sail generally above the tunnel centerline, which complicated wall corrections but substantially reduced strut interference effects. The strut rotated about its vertical axis to obtain sideslip angles of ±20°.

5

The 6-component balance system of the Army's 2- by 3-m (7- by 10-ft) wind-tunnel facility at Ames Research Center was used. Readings from strain-gauge balances were averaged for each data point and recorded on a PDP-11 computer which also provided on-line uncorrected data reduction. The following scale resolutions were available and were effectively reduced by averaging:

Lift	±0.9 N	(0.2 lb)
Drag	± .09 N	(.02 lb)
Side force	± .09 N	(.02 lb)
Pitching moment	± .16 Nm	(.12 ft/lb)
Rolling moment	± .14 Nm	(.10 ft/lb)
Yawing moment	± .14 Nm	(.10 ft/lb)

Angle-of-attack measurements were made with an Angle Indicating Digital Servo attached to the support structure, as shown in figure 9. The output from this servo was input directly to the digital data acquisition system.

In addition to the six-component force data, photographs of wool tuft patterns were taken to provide information on stall characteristics and basic flow properties. Photographs of the sail shape change with angle of attack were also recorded for comparison with future analytical work.

Data Analysis

Scale outputs were converted to standard forces and moments in nondimensional coefficient form using projected area, mean geometric chord, and span as references. Except where otherwise noted, the reference center about which moments were computed is the pilot tether point near the apex of the control frame [2.54 cm (1.00 in.) below the keel]. Reference center locations are shown for each model in figures 2-4. Angle of attack is measured with respect to the keel in all cases. [Note that the sail root chord in some cases is not parallel to the keel (fig. 7).] Moments are presented with respect to a wind-axes system (fig. 10) unless otherwise specified. The importance of the choice of reference axes and moment center is discussed in a later section.

Weight tares- Wind-off measurements of weight tares with and without model were made for various angles of attack and sideslip, fit to a two-dimensional least-squares approximation, and subtracted from the data.

Aerodynamic tares- Model-off runs were made to determine the aerodynamic forces exerted on the strut-mounting system at various angles of attack, side-slip, and dynamic pressure. A three-dimensional least-squares approximation of these tares was subtracted from the data. No other correction for strut interference was made.

Tunnel boundary corrections- Longitudinal and lateral data were corrected for blocking, streamline curvature, and induced angle effects according to procedures described in references 13-16 for these yawed, swept models, off the tunnel centerline. Maximum model span was about 70% of the tunnel span.

6

This resulted in an induced upwash of about 0.75° at the root quarter chord of the model. The effect of increased upwash at the tips is negligible at low-lift coefficients. At the higher C_L an effective decrease in washout is induced. This is partially compensated by the aeroelastic response (greater geometric washout). The spanwise variation of boundary-induced velocities was small, only slightly affecting the glider stalling behavior. At C_L of 1.0 an effective decrease in washout of less than 0.5° was induced.

Uncertainties are introduced into the data from several sources: 1) scale nonlinearities, 2) weight tare and aerodynamic tare fitted curve errors, 3) moment arm measurement uncertainties, 4) support system flexibility, 5) minimum measurement accuracy of scales, 6) noise in zero readings, 7) measurement accuracy of Angle Indicating Digital Servo, 8) hysteresis in scale balance system, and 9) model centering. The net uncertainties in the six components of forces and moments are approximately:

α	±0.05°	
C_L	± .02	
C_D	± .005	
C_Y	± .005	
C_m	± .01	
C_ℓ	± .005	(±0.01)
C_n	± .005	(±0.01)

Values in parentheses indicate uncertainties during yaw sweep in which large weight tares and hysteresis effects appeared during turntable rotation.

Some previous investigations (refs. 10-12 and 17, 18) have shown that results vary considerably with dynamic pressure. In this investigation, data were obtained at dynamic pressures ranging from 240 N/m² (5.0 psf) to 960 N/m² (20.0 psf). The Reynolds number corresponding to the tunnel conditions at 20 to 40 m/sec (65 to 130 ft/sec) is 1.35×10^6 to 2.70×10^6 per m. Since the models were constructed for elastic similarity at a Reynolds number of 0.54 times the full-scale value, these conditions correspond to full-scale velocities of 7 to 15 m/sec (24 to 48 ft/sec) based on equivalent elastic deformations.

Because of the large amount of tunnel time required to generate data on the number of configurations shown in table 1 with a three-dimensional test matrix (α, β, q), some of the test runs were made at only one dynamic pressure and are intended to demonstrate configuration-dependent trends rather than to establish a comprehensive data base on a very limited number of configurations.

Model structural considerations also limited testing at the high dynamic pressures. The 1.6-mm (1/16-in.) high-strength bolts were required to withstand stresses similar to the 8-mm (5/16-in.) aircraft bolts used on full-scale gliders and sail material was required to withstand full-luffing, low

7

angle-of-attack measurements at tunnel speeds up to 40 m/sec (130 ft/sec). These severe conditions resulted in a sail failure at the trailing edge of the first model and two bolt failures with subsequent models. The latter two structural failures occurred at highly stressed areas which were recognized during model construction as potential problems, and safety wires at these joints prevented major damage to the models.

PRESENTATION OF RESULTS

Figures 11-13 are installation photographs of the three models tested. Measured aerodynamic characteristics of these configurations are outlined below and are presented in figures 14-64. Table 1 describes the configurations.

Description	Configurations	Figures
Selected tuft photographs — stall behavior	1, 2A, 3I	14-18
Longitudinal characteristics of basic models — variation with q and α	1, 2B,C,H, 3H	
Lift		19-21
Drag		22-24
Moment		25-29
Variation of C_m with reference center location	1, 2E	30-31
Pitching-moment variation with sideslip	1, 2A, 3H,I	32-35
Effect of modifications on longitudinal characteristics		
Lift	2D-G,L-P, 3B-E,H,G	36-40
Drag	1,2B-G,L-P, 3B,E,H	41-48
Moment	2B-G,L,N,P, 3B-E,H,G	49-55
Lateral characteristics of basic models vs α	1, 2A,H,N,Q, 3H,I	56-64

8

DISCUSSION OF RESULTS

General Results

Lift curve- Figure 19 shows that a large range of nearly linear C_L vs α exists even for the high-billow "standard" design. A lift curve slope of about 2.2/rad, a relatively large C_L of 1.4 at 37°, a break in the linear curve at about 10° due to luffing, and a shift in the curve near $\alpha = 0°$ when the sail collapses in front of the cross bar are all apparent in the figure and agree well with previous results.

The second model exhibits a very linear lift curve from $C_L = 0$ (where luff-line tension diminishes rapidly) up to bout $C_L = 0.8$. The curve reaches a maximum of 0.92 for the basic configuration (fig. 20).

In contrast to the above, the variation of C_L with α for the third model is more nonlinear (fig. 21). This is probably a result of higher sail tension and a correspondingly greater deformation with loading. This trend is also visible in the variation with dynamic pressure. The highly reflexed airfoil combined with an early root stall results in a relatively low $C_{L_{max}}$ of 0.83 at 24°.

Drag data- Drag data for the basic configurations are given in figures 22-24. Data on other configurations are presented in figures 41-48. As mentioned previously, drag results must be corrected for two effects: 1) the use of larger-than-scale cables, and 2) the absence of pilot drag. Results from this investigation, together with results in references 10-12 and 19-21 were used to approximate the relative contributions of various glider components to the total drag of the glider.

Cables: It is difficult to estimate the actual drag of cables in the vicinity of the glider. When the data for isolated cables from reference 19 are used, a drag coefficient of 1.0 per unit length based on diameter appears reasonable. For conventional ultralight designs this may be expressed approximately as:

$$f = 0.044 + 0.0037 \ b \ (m^2) \quad [0.47 + 0.012 \ b \ (ft^2)]$$

of equivalent flat-plate drag area, or about 0.08 m^2 (0.86 ft^2) for a typical 10-m (33-ft) span glider. The data presented here must, therefore, be corrected to account for the large-diameter cables as follows:

$$\Delta C_{D_o} = \begin{cases} \text{Standard:} & -0.0050 \\ \text{Model 2:} & -0.0056 \\ \text{Model 3:} & -0.0055 \end{cases}$$

Pilot and harness: Estimates of pilot and harness drag from references 10 and 12 vary from 0.12 m^2 (1.3 ft^2) to 0.23 m^2 (2.5 ft^2). A full-scale pilot drag area of 0.21 m^2 (2.3 ft^2) leads to the following corrections which must be added to the model data:

9

$$\Delta C_{D_o} = \begin{cases} \text{Standard:} & 0.0115 \\ \text{Model 2:} & 0.0118 \\ \text{Model 3:} & 0.0118 \end{cases}$$

Cross bar: The drag of the cross bar varies with its distance from the sail and with the lift coefficient of the glider. A rough approximation to its drag from reference 19 is

$$f = 0.03 \ b \ (m^2) \quad [0.09 \ b \ (ft^2)]$$

Control frame: Approximately $0.186 \ m^2$ $(2.0 \ ft^2)$ of parasitic drag area is due to the control bar and kingpost (ref. 19).

Sail drag: The remaining drag on the glider is the viscous and induced drag of the lifting surface. Examination of section characteristics in the Reynolds number range of 5×10^5 to 1×10^6 (refs. 19-21) shows that profile drag varies rapidly with lift coefficient (especially for thin sections). The drag data obtained here for the second model is plotted vs C_L^2 in figure 44. The curve is clearly not linear and much greater success was achieved in fitting data to a three-parameter drag polar. This is partly due to the large amount of twist in these wings and partly to the highly cambered sections which achieve minimum drag at a relatively high C_L. This large lift-dependent viscous drag makes the usual relation for drag: $C_D = C_{D_o} + C_L^2/\pi AR$ unsuitable over the large C_L range in which hang gliders operate, and data were fit to the form $C_D = C_{D_{min}} + K \ (C_L - C_{L_o})^2$ (figs. 45-48).

Apparent in these figures is the influence of twist on drag (see especially fig. 44). In addition to an increment in $C_{D_{min}}$, twist produces a more rapid increase in drag with lift for the configurations tested here.

For convenience in data interpretation the drag polars for many configurations were fit to a three-parameter drag polar in the range $0.2 < C_L < 0.8$ and are summarized below. (Note that $C_{D_{min}}$ has not been corrected for pilot or oversized cables.)

$$C_D = C_{D_{min}} + K(C_L - C_{L_o})^2$$

Configuration	$C_{D_{min}}$	K	C_{L_o}	Comments
1	0.122	0.321	0.44	$0.45 < C_L < 1.1$
2B,C,D,E,F,G	.073	.138	.27	6 config. avg.
20	.082	.183	.28	
2P	.078	.141	.35	
2E	.073	.148	.30	
2L	.083	.164	.28	
3H	.067	.231	.21	
3F	.073	.179	.25	
3E	.072	.296	.33	$0.2 < C_L < 0.85$
3B	.079	.285	.27	

10

Pitching moment-

Standard: The variation of C_m with α is shown in figure 25. The highly nonlinear character of the curve is attributed primarily to deformation of the flexible sail. Figure 25 indicates that a negative pitching moment is present throughout the entire range of α tested. This is in agreement with results from references 1-7 and implies that some "bar pressure" corresponding to a rearward center-of-gravity shift is required to trim this glider at the desired C_L. The slope of C_m vs α changes several times throughout the angle-of-attack range. During these tests significant changes in sail shape were observed to coincide with discontinuities in the pitching-moment curve.

Trailing-edge luffing began at about 22°, appearing as high-frequency motion of the trailing edge from midspan to tips. The luffing spread forward and at about 16° low-frequency "rippling" extended to the cross bar. At 13° large-scale motion of the sail from the cross bar, aft, was observed while the forward sail portion remained inflated. From 13° to 10° the sail maintained this general shape while the amplitude of the luffing increased. At about 10° the forward portion of the sail became slack and also experienced large-scale luffing. From 10° to 2° the sail was fully luffing with large amplitudes. The sail appeared to lie almost uniformly in the plane of the frame. At about 2° the forward portion of the sail began to inflate on the opposite side of the frame intermittently. By -2° it had stabilized in this position, forming a highly cambered surface between the leading edges and cross bar while the sail aft of the cross bar remained luffing. The rear portion of the sail continued to luff extensively to -25° where only high-frequency luffing of the trailing edge persisted.

The pitching-moment curve clearly reflects these observed changes in sail shape. The slope of C_m vs α increases as the trailing edge begins luffing, corresponding to a decrease in the local lift-curve slope near the trailing edge. As the entire rear portion of the sail begins luffing C_{m_α} becomes more positive.

The rear portion of the sail may be regarded as analogous to a horizontal stabilizer; although "fixed" under tension at high C_L, it becomes unloaded at low-lift coefficients and is free to move downward. This corresponds to a "stick-free" horizontal control surface in the analogy, with subsequent reduction in longitudinal static stability. When the forward sail part begins to enter global luffing, the rear sail is no longer more "free" than the forward section since the sail in front of the cross bar also changes its incidence with α. Thus, C_{m_α} becomes more negative when the forward sail area begins luffing (at -10°). At 2°, when the sail begins to inflate negatively near the nose, the stick-free analogy again holds and C_{m_α} becomes positive. As sail tension at the trailing edge increases and luffing subsides, the glider becomes "stable" again near -25°.

The physical interpretation of the nonlinearities in pitching moment applies not only to the standard configuration but to many flexible gliders in which sufficient sail slackness exists for large-scale luffing. The initial destabilizing break in C_{m_α} due to luffing occurs on many gliders

11

although the subsequent increase in stability is often prevented with the use of battens and root camber which prevent forward sail luffing. This increase in stability at about 10° on the "standard" in the full-luffing condition may result in a stable trim point at low C_L for sufficiently aft center-of-gravity positions. Such stable "full-luff dives" were reported with these early designs (refs. 22-26) and, although the mechanism was not fully understood, corrective measures have virtually eliminated this problem in current designs, as seen in pitching-moment data for other models tested here.

Also apparent in the pitching-moment data for the "standard" is a large nose-down moment at stall. Tuft studies indicate that this is due to leading-edge separation at the higher C_L with sections just inboard of midspan stalling first (fig. 14).

Models 2 and 3: Features of the pitching-moment curves for models 2 and 3 will be discussed in detail in the following sections in terms of the effects of configuration changes. In general, the variation of C_m with α differs greatly from the original standard configuration. Lower sail fullness, the use of battens, reflex, and fixed minimum twist produce a much more linear pitching-moment curve. Most of these configurations were found to be stable and trimmed "hands-off" in the desired C_L range, although considerable variations were produced with changes in twist and luff-line arrangement.

Choice of reference centers/axes systems- The basic reference centers about which moments are measured in this report are shown in figures 2-4. These centers correspond to pilot tether positions, the point at which the pilot's harness is attached to the glider. This point has been chosen here and in many previous studies (refs. 10-12, 27, 28) since it corresponds approximately to the glider's center of rotation when no pilot control force is present. That is, although the center of gravity of the pilot-plus-glider system is located below the keel, rotations occur about a point near the keel if the pilot is free to swing about the tether point.

A measure of "hands-on" stability, corresponding to the case in which the pilot's position is fixed with respect to the control bar, is obtained from a plot of C_m about the combined pilot and glider center of gravity. In this case the reference center is located below the keel. As can be seen from figures 22 and 23 the two curves are substantially different. (In these figures the reference point was fixed relative to the glider at the combined pilot/glider center of gravity, which was assumed to lie 24.4 cm (9.6 in.) vertically below the models' keel at an angle of attack of 25°.) The effects of the low-center-of-gravity position are (1) increased stability at high C_L, 2) somewhat larger C_{m_o} (due to drag), 3) decreased stability at negative angles of attack.

Simple geometric considerations show that the vertically displaced center of gravity introduces a pitching moment which varies with α^2, increasing the stability at positive angles and contributing large destabilizing moments at negative angles. It is possible that this effect is a major contributor to the "tumbling" phenomenon discussed in references 12, 22, and 28 and commonly reported with early high-performance hang gliders. The rapid nose-down

12

pitching velocity which may continue for several rotations begins with an encounter with a negative vertical gust or gradient. In reference 12 the cause of this phenomena is described as associated with aeroelastic deformations of the sail which result in large, negative pitching moments when the forward sail portion collapses. Results of the present investigation show that the negative value of the pitching moment down to $-30°$ is comparable to that in the normal flying regime. The fact that many of the hang gliders which have reported tumbling problems used relatively tight sails, which would not produce sudden nose-down moments at negative angles of attack, also indicates that another effect may be important. In the observed cases of tumbling with hang gliders "pilots have maintained their grip on the control bar" (ref. 28) and the vehicle in reference 22 which exhibited tumbling had a center of gravity fixed at a point 25% of the keel length below the keel.

The importance of vertical center-of-gravity location to the pitching-moment characteristics of the glider and the effect of reference center location on the appearance of moment data indicates that care should be taken in drawing conclusions about stability without carrying out a dynamic analysis. The United States Hang Gliding Association has developed pitching-moment requirements for glider certification in an apparently successful self-regulation program. Among these empirically determined requirements is a minimum pitching-moment coefficient at zero lift of 0.05 based on MAC and measured about the pilot tether point. The above considerations indicate why such a large pitching moment at zero lift is a reasonable requirement and why demonstrated ability to recover from near-zero angle-of-attack conditions (as was once the requirement) is not sufficient to ensure longitudinal stability.

Similar considerations apply to the choice of reference axes systems. A wind-axes system, shown in figure 10, was used to define the moments and forces in the report. Two other reference systems, often used in the presentation of wind-tunnel data and/or dynamic analyses, are the stability- and body-axes systems, shown in figures 65 and 66. In the symmetric flight condition ($\beta = 0$) no difference between these systems exists for longitudinal data. In general, however, major differences appear for lateral coefficients, especially at high angles of attack or sideslip. The transformations between the three systems for use in comparing these data with results of other studies and in future dynamics work are included in the appendix. Of special interest is the fact that wind axes and stability axes produce the same value of yawing-moment coefficient while body axes and stability axes provide identical measurements of pitching moment and side force. When yawing-moment data are expressed in body axes, as in references 2 and 5, most gliders exhibit negative values of C_{n_β} (usually indicative of directional instability) at higher angles of attack. In stability and wind axes, however, C_{n_β} appears to increase with α. Variation in the appearance of lateral derivatives vs angle of attack, depending on the axes system chosen, is demonstrated in figures 56 and 57, in which lateral derivatives are expressed in wind axes and body axes, respectively. Conclusions concerning the directional stability of these gliders without a study of the dynamics cannot be made with certainty.

Influence of changes in dynamic pressure- Changes in sail shape due to structural elasticity together with Reynolds-number-dependent flow characteristics are expected to produce changes in aerodynamic coefficients with dynamic pressure. Figures 19-29 illustrate the effects of airspeed on the characteristics of models tested here. In agreement with previous full-scale tests, pitching-moment coefficient appears to be most strongly affected by changes in dynamic pressure. Lift and drag coefficients do not appear to be affected greatly in the range of speeds employed here.

Similar effects are observed with the second model. Larger variations in aerodynamic characteristics with q appear in the data at low angles of attack. This is expected because of the relatively fle 'ble battens wl ase shapes vary greatly with loading at the angles where lufr lines are ef ective. Monotonicity of pitching-moment coefficient changes vs q was investigated and presented in figure 29. In these runs, a variety of dynamic pressures was used while the model attitude was fixed. At those angles tested, pitching-moment coefficient does not vary greatly with q, but a steady decrease in the magnitude of C_m is observed for all α — especially at the lower angles where luff-lines are in tension.

The third model exhibited larger variations in aerodynamic properties with dynamic pressure throughout the range of angle of attack tested. Lower lift coefficients at given α and smaller pitching-moment coefficients at low C_L were obtained at higher tunnel speeds, as shown in figures 21 and 28. This general trend also appears in full-scale results.

Since "speed stability" and "angle-of-attack stability" are both desirable, it is not possible to infer longitudinal stability characteristics by inspection of a single plot of C_m vs α at fixed q or C_m vs C_L at fixed load. Although much can be said from such data, the importance of a dynamic analysis is again demonstrated.

Separ tion phenomena- The appearance of separated flow on the models was observed with the use of wool tufts attached to the sail upper surface (and lower surface in some cases). Runs with and without tufts indicated that their presence had a negligible effect on coefficient data.

Stall behavior of the first model is summarized in figures 14(a)-14(g), which are traced from photographs of the tufted model. Separation occurs first at a sectior near the midspan, spreading outward quickly. The root section rem ' is attached to very high angles.

Sent ation from the second basic configuration with a minimum of 24° of negati.e tip incidence (with respect to the keel) begins at the root chord and slc. ly spreads toward the tips. The flow at the wingtips remains attached up t a keel incidence of 39°. This is primarily due to the fact that the tips are allowed to twist under the applied loads and assumed a shape with a large amour.t of washout (>30°) at the extreme angles of attack. However, even when the washout was fixed at 12°, separation occurred first at the root, spreading more rapidly toward the tips as α was increased. The process is shown in figure 15. Also apparent from these studies is the effect of sideslip on

14

stall characteristics. Figure 16 illustrates the stall behavior at a sideslip angle of 20°. As expected, the trailing-wing stall occurs at a much lower angle than that of the leading wing, although the effect on the lateral derivatives does not appear significant.

The third model demonstrated similar stalling characteristics with a root stall occurring at 29°. Increasing tip washout with angle of attack prevented tip stall up to 40°. Despite the lower sweep angle, observed behavior in the sideslipping condition was similar to that of model 2. On the third model, the lower surface of the sail was also tufted during one of the tests. The stiff, highly cambered batten/ribs which extended to the leading edge of this model produced an airfoil shape with pronounced lower-surface separation at angles of attack up to 20°. The flow pattern inferred from tuft observations is shown in figure 18. Most of the lower-surface flow remains separated up to 5° where flow begins to reattach some distance aft of the leading edge. Reattachment location moves toward the leading edge as incidence is increased with lower surfaces near the wingtips remaining separated up to 20° (due to lower local incidence with washout).

The appearance of lower-surface separation suggests that substantial performance losses may be associated with the use of profiles similar to those tested. Eppler (ref. 21) discusses this problem in the design of airfoils for use on ultralight gliders. In order to obtain low-section drag at high C_L and large maximum-lift coefficients, a large amount of camber is required on these thin sections. Since camber generally creates a large, negative C_{m_o}, airfoils with large nose camber and reflex appear desirable, yet this large nose camber results in poor low-lift drag characteristics. The solution seems to require the use of sections with greater thickness. Many recent glider designs employ double-surface airfoils and may overcome the observed difficulties in obtaining the required maximum lift, low-pitching moment, and low-section drags.

Lateral data- The variation of C_{ℓ_β} (effective dihedral) with angle of attack is shown in figures 56-64. These curves were obtained from tests at a fixed yaw angle of 20° after yaw runs showed that the coefficients were linear in β up to this angle. All gliders tested showed a decrease in C_{ℓ_β} with C_L as expected from simple sweep theory with C_{ℓ_β} becoming positive at low angles of attack. The loss of effective dihedral at low-lift coefficients may be attributed to the lack of geometric dihedral combined with the high twist of these wings. (At low angle of attack the section C_L near the tips is negative, producing, according to sweep theory, an adverse roll due to sideslip.) This behavior has been reported in reference 12 and appears to be characteristic of a majority of hang-glider designs. The magnitude of C_{ℓ_β} at a given C_L is greatest for model 1 and least for model 3, reflecting the expected dependence on sweep angle.

Figures 56-64 also show the behavior of C_{n_β}, the yawing-moment coefficient due to sideslip derivative, as a function of incidence angle. In the

15

chosen reference axes system, C_{n_β} for the first model increases with C_L up to a C_L of 0.8 and maintains this value of C_{n_β} up to 45°. The third model demonstrates similar behavior with a roughly parabolic variation of C_{n_β} with C_L through stall but with a generally lower value of C_{n_β} than model 1. The second model's yaw stiffness does not change monotonically with C_L but maintains a small positive value of C_{n_β} out to stall as indicated in figure 59. Values of C_{n_β} for model 1 in the body-axes system are given in figure 56.

The variation of C_m with α at 20° of sideslip is compared with the symmetric data in figures 32-35. The effect is model dependent and no general conclusions are apparent from the data expressed in this form. It should be noted that the positive increments in C_m due to sideslip for the first model appear as negative increments at the higher angles of attack when expressed in body axes, again indicating the necessity of more thorough analysis to assess the importance of these results. Coupling of longitudinal and lateral motion, as suggested by the change in C_m with β, is a result of aeroelastic distortion of the sail which changes the lift distribution of the wing in such a way as to produce a (sometimes large) pitching moment. Reference 12 indicates that in some cases a large nose-down pitching moment is produced, increasing the possibility of pitch divergence at low C_L. Results from similar tests with the second model indicate a less important effect, while the pitching moment of the third model appears significantly altered at 20° of sideslip. In fact, a stable (in α) $C_m = 0$ point appears at this condition. The point is not actually a trim point since C_n is nonzero at this attitude and a corrective yawing moment will tend to reduce β and hence increase C_m.

Effects of Configuration Changes

A major goal of this experimental investigation was the analysis of effects on the aerodynamic properties of ultralight gliders of various design modifications. Full-scale tests have shown that rather large differences exist in data obtained from gliders with very similar geometries due to differences in sail and cable tension, small variations in sail shape, leading-edge stiffness, etc. Difficulties associated with elastic scaling of small models may also lead to some differences between these results and the properties of a particular full-scale vehicle. Conclusions drawn from comparative studies of modifications to a basic configuration are less affected by such difficulties, and it is believed that general results obtained from these model tests will be especially useful in full-scale applications.

Washout- Figures 36-55 illustrate the effects of various modifications on the longitudinal characteristics of models 2 and 3. In these figures, data on configurations 2A-P may be compared to obtain an idea of the effects of twist on lift, drag, and moment characteristics of a typical contemporary glider. A primary effect of washout on this swept wing is, of course, on pitching moment. When the minimum washout of the tip is constrained by a rib fixed

16

to the leading edge (fig. 5), the pitching moment at low angles of attack is increased greatly. Fixing the incidence of the tip at angles below 20°, as is accomplished by the "floating tip" arrangement of configurations 2A-D, H-Q, also increases the glider's longitudinal stability in this range. At higher angles of attack the local tip incidence increases to approximately 30° with respect to the keel on this model. This condition prevents the tip from stalling, increases the drag, and decreases $C_{L_{max}}$. The effects of wing twist on lateral derivatives were not evaluated systematically in the present study but are believed to be responsible for the loss of effective dihedral discussed previously.

Luff lines- Luff lines or reflex bridles are lines connected to a point on the upper-wing structure (usually the upper wires near the kingpost) and to the ends of one or more pairs of battens near the trailing edge (see fig. 6). At normal flying attitudes the trailing edge of the sail lies above the plane of the frame and luff lines remain slack. As the angle of attack is decreased to very low and negative angles, the sail trailing edge moves toward the frame plane and luff lines tighten, preventing further displacement of the trailing edge. If the battens are flexible, a large amount of reflex or negative camber is produced along with a strongly stabilizing (nose-up) pitching moment. Thus, a very large C_{m_o} at low and negative angles of attack is achieved with a very small performance loss in the normal flight regime. Luff lines are now incorporated on nearly all flexible-wing hang gliders and play a large role in the elimination of the (once common) tumbling and high-speed stability problems. Their effects are illustrated in figures 36-55. Luff-line length determines the angle at which their effects become important and, to some extent, the magnitude of C_m produced. Other factors which appear to affect the influence of luff lines are illustrated in the figures and include: 1) luff-line batten stiffness — gliders with luff lines attached to inflexible battens require large dynamic pressures to produce reflex and seem less effective in generating C_{m_o}; 2) chord of batten to which luff lines are attached — larger chord leads to larger camber change for given batten stiffness as well as greater contribution to glider C_m; 3) spanwise location of luff lines and model sweep — luff lines which are located some distance from the root chord on swept wings may increase the wing washout in addition to increasing the local section's C_m. These factors must be considered simultaneously in the evaluation of luff-line effectiveness. For example, luff lines located near the root of a highly swept wing with relatively stiff battens may reduce the washout by holding the root chord at a more negative incidence with respect to the fixed tip angle, while producing little reflex change. In general, however, configurations similar to those commonly flown employ luff lines which are capable of generating C_m of approximately +0.1 to +0.2.

Batten flexibility- The effect of batten flexibility on longitudinal characteristics of the second model are shown in figures 37(b) and 51. The primary impact of batten flexibility is that associated with luff lines discussed above. Batten stiffness also influences section camber in the absence of luff lines. Stiffer (straight) battens reduce sail camber and subsequent variations in C_m and C_L vs α are apparent in figures 37(b) and 51. Runs at high speeds with the most flexible battens produced large-amplitude flutter

(distinct from the aerodynamic luffing observed on the first model) and prohibited tests of this configuration at all but the larger angles of attack.

Reflex and rib camber– Steel music wire (1/8-in.) ribs with various amounts of reflex and camber were substituted for flexible battens in several runs with model 3. Results are presented in figures 40, 43, and 53. Data for models with highly cambered sections show an increase in drag at low C_L associated with lower surface separation discussed previously. A higher $C_{L_{max}}$ and lower drag at high-lift coefficients is obtained with this configuration, however. Tests with ribs having greater nose camber and increased trailing-edge reflex show the expected increase in C_{m_o} with an additional low-angle-of-attack drag penalty.

Sweep– A comparison of the results from models 2 and 3 demonstrates the general effect of sweep on the static longitudinal and lateral characteristics of these designs. Basic differences lie in the method by which the large C_m required at zero lift is obtained. Highly swept gliders may rely on the pitching moment produced by twist, while gliders with very low sweep must employ sections which are highly reflexed at low angles of attack. Part of the motivation for designs with relatively low sweep includes: 1) more desirable stalling characteristics; 2) lower twist drag, if required C_{m_o} can be achieved without large washout; 3) elastic deformation of the tips, decreasing washout at high speeds, and increasing wa: out at high angles of attack will not result in such destabilizing changes in pitching moment; 4) lower effective dihedral at high C_L may improve lateral control. Higher sweep designs exhibit greater directional stability and some washout may be used to simultaneously reduce tip-stall tendencies, produce C_{m_o}, and improve spanwise lift distribution.

Results of present tests indicate generally larger values of $\left| C_{\ell_\beta} \right|$ and C_{n_β} for the higher sweep model. Performance comparisons show that the second model exceeded the maximum L/D of the lower sweep design. This is attributed to two factors. The airfoil shape of the basic low-sweep configuration was highly reflexed and cambered. Resulting lower surface separation increased the profile drag of this design relative to that of the flatter sail of model 2. Low leading-edge sweep also reduces the effective torsional rigidity of the wing and without some leading-edge restraint, very large sail tension is required to attain a "flat" sail. As no restraint fixed to the leading edge was employed here, a resulting nonoptimal twist distribution produced high induced drag and premature root stall with correspondingly low $C_{L_{max}}$. Therefore, these data should not be used directly to assess the relation between sweep and potential performance. It is shown, however, that it is not difficult to obtain the required C_{m_o} through the use of reflex rather than twist.

Sail fullness (billow)– No tests were run in which billow was systematically varied. Comparison of results from the standard configuration and the second model indicate that much of the nonlinearity in the aerodynamic

18

characteristics of these aircraft is a result of large sail fullness. Higher
sail tension allows the glider to approach more closely an optimal spanwise
load distribution and reduces the drag substantially at low angles of attack,
as can be seen from figures 45 and 46.

Keel pockets- The second model was tested with and without a "keel
pocket," shown in figure 7. The keel pocket provides a means of attaching
the sail at the keel in such a way that it is free to slide laterally as load-
ing changes. This technique is used to decrease the roll damping, C_{l_p}, and to
increase the effectiveness of the "weight-shift" control method. Although it
is intended to change damping derivatives, its effect on static derivatives
was evaluated here (see fig. 52). Major changes in the glider geometry with
the addition of a keel pocket affect static results as follows: By reducing
the incidence of the root section with respect to the keel (to which angle
of attack is referred) the zero-lift incidence is increased. Because of
the reduced root incidence, the twist (washout) is reduced as tip washout
constraint ribs were not altered. The root chord is raised out of the plane
of the frame which introduces approximately 2° of anhedral. The keel pocket
also adds some lateral area aft of the reference center and thus affects
directional stability.

Figure 42 illustrates the influence of the keel pocket on pitching moment
vs C_L. The increment in pitching-moment coefficient at low C_L is due to
the flexible rib section and trailing-edge support wire (fig. 7) which act in
a manner similar to luff lines. A large amount of reflex is produced at the
root chord as the trailing edge is held fixed and the (negative) camber of the
flexible rib increases under negative load. The shift in C_m curve at the
larger values of C_L and the higher $C_{L_{max}}$ due to reduced twist are apparent
in figure 50. Lateral derivatives vary in the manner shown in figure 65.
Included in this data is a small increase in C_{l_β} due to anhedral. The value
of C_{n_β} is not measurably changed.

Dihedral- The loss of effective dihedral at low angles of attack
($C_{l_\beta} > 0$) suggests that the incorporation of geometric dihedral might improve
the lateral characteristics of gliders at high speeds. Theoretical considera-
tions also suggest that the low values of C_{n_β} might be increased with
dihedral. These assertions were tested by introducing 3.5° of dihedral (per
side) to the second and third models. Figures 34, 35, and 61-64 summarize the
results. The general conclusion from these data is that this amount of geo-
metric dihedral is insufficient to significantly alter either C_{l_β} or C_{n_β} in
the desired range of lift coefficients. Figure 53 indicates that the inclu-
sion of this amount of dihedral does decrease the angle at which C_{l_β} becomes
positive (by approximately 5°) but the character of the curve remains
unaltered. A small effect on the pitching moment coefficient at 20° of
sideslip is indicated in figures 34 and 35 but, again, the effect is small.

19

Comparison with Previous Work

Results of full-scale wind-tunnel tests of various configurations reported in references 1-12 and 17 agree well with those presented here. Values of $C_{L_{max}}$ and C_{L_α} for model 1 lie well within the range of values obtained in these investigations. The general characteristics of pitching moment vs angle of attack are observed in each of the studies in the range in which data are available, although some differences are expected in light of dissimilarities, in particular model construction methods.

Although most of the data available for comparison are found in NASA reports on designs similar to the standard configuration, some results for more contemporary designs are available (refs. 10-12). The effects of luff lines and fixed twist ribs have been investigated previously in tests of production gliders using "test vehicles." Gliders are mounted on automobiles or on carriages in front of the car and simple balances used to determine the pitching moment at a given angle of incidence. A sample of such data is shown in figure 35, kindly provided by Mr. Tom Price, former president of the Hang Glider Manufacturers Association. The basic behavior of C_m vs α as affected by luff lines and fixed tips also appears in the wind-tunnel tests of figure 49(a), although the data at negative angles of attack differ. This difference is probably due to the influence of the large keel pocket with flexible root batten of configuration 2E which increases the root reflex at low C_L; this was not incorporated in the configuration of figure 55. Differences in moment reference center also contribute to this discrepancy.

Some disagreement in $C_{L_{max}}$ is observed between the present tests and the data in references 10 and 11. Although the value of $C_{L_{max}}$ for the first model is in good agreement with previous data, values of $C_{L_{max}}$ for the second and third models appear lower than expected. The discrepancy is partially due to the difficulty of producing "clean," rippless sails at these small scales. Such imperfections may lead to early separation. The somewhat lower Reynolds number involved in these tests might be expected to reduce $C_{L_{max}}$ while values in reference 10 may be overestimated due to large blocking effects.

A comparison of lateral derivatives measured here and in references 2, 3, 8, and 12 for the standard configuration indicate the same general behavior with angle of attack. Differences are due partly to small differences in reference center location with insufficient information available to relate all data to the same reference as well as differences in the individual model geometries (see fig. 56).

20

CONCLUSIONS

Static longitudinal and lateral aerodynamic characteristics of 27 variations of 3 basic ultralight glider configurations were determined from wind-tunnel tests of 1/5-size, elastically scaled models. The importance of sweep, twist, luff lines, batten flexibility, reflex, keel pockets, and dihedral are discussed as they relate to the data obtained here. Modern glider configurations exhibit much more stable and linear pitching-moment characteristics than older Rogallo designs which are shown to have potentially dangerous characteristics at low angles of attack. Fixing the center of gravity vertically below the keel may produce large destabilizing moments at negative angles of attack and may contribute to the possibility of tumbling.

Differences in the appearance of lateral derivatives depending on choice of reference axes system are important for these gliders which fly at unusually large angles of attack, thus demonstrating the need for a full dynamic analysis in the assessment of glider stability. Variations of pitching moment with sideslip and dynamic pressure complicate the analysis of longitudinal stability but are important for some of these configurations. All gliders tested demonstrated a loss of effective dihedral (associated with positive values of C_{l_β}) at low angles of attack. This is attributed to the influence of sweep and twist on C_{l_β} and the lack of geometric dihedral.

The data presented here are intended to provide some basic information on the aerodynamic characteristics of modern hang gliders and the effects of various design modifications. Results form a base of empirical data from which analytical work on stability and control, necessary for a correct interpretation of these data, may proceed. Such work, planned for future publication, involves the development of more refined performance and stability prediction methods in a form which may be used in the design of safer and more efficient ultralight gliders.

APPENDIX

TRANSFORMATIONS BETWEEN AXES SYSTEMS

The following relations may be used to transform the data (expressed in this report in wind axes) to stability or body axes. (Note that $M_B = M_S$ while $N_S = N_W$.)

$$L_B = L_W$$

$$D_B = D_W$$

$$Y_B = Y_W \cos \beta - D_W \sin \beta$$

$$M_B = M_W \cos \beta + \ell_W \sin \beta$$

$$\ell_B = -M_W \sin \beta \cos \alpha + \ell_W \cos \beta \cos \alpha - N_W \sin$$

$$N_B = -M_W \sin \beta \sin \alpha + \ell_W \cos \beta \sin \alpha + N_W \cos \alpha$$

$$L_S = L_W$$

$$D_S = D_W$$

$$Y_S = Y_W \cos \beta - D_W \sin \beta$$

$$M_S = M_W \cos \beta + \ell_W \sin \beta$$

$$\ell_S = -M_W \sin \beta + \ell_W \cos \beta$$

$$N_S = N_W$$

22

REFERENCES

1. Polhamus, E. C.; and Naeseth, R. L.: Experimental and Theoretical Studies of the Effects of Camber and Twist on the Aerodynamic Characteristics of Parawings Having Nominal Aspect Ratios of 3 and 6. NASA TN D-972, 1963.

2. Bugg, F. M.: Effects of Aspect Ratio and Canopy Shape on Low-Speed Aerodynamic Characteristics of 50 Swept Parawings. NASA TN D-2922, 1965.

3. Naeseth, R. L.; and Gainer, T. G.. Low-Speed Investigation of the Effects of Wing Sweep on the Aerodynamic Characteristics of Parawings Having Equal Length Leading Edges and Keel. NASA TN D-1957, 1963.

4. Johnson, J. L., Jr., and Hassel, J.: Full-Scale Wind Tunnel Investigation of a Flexible-Wing Manned Test Vehicle. NASA TN D-1046, 1963.

5. Johnson, J. L., Jr.: Low-Speed Wind Tunnel Investigation to Determine the Flight Characteristics of a Model of a Parawing Utility Vehicle. NASA TN D-1255, 1962.

6. Johnson, J. L., Jr.: Low-Speed Force and Flight Investigations of a Model of a Modified Parawing Utility Vehicle. NASA TN D-2492, 1965.

7. Turnell, J. A.; and Nielsen, J. N.: Aerodynamics of Flexible Wings at Low Speeds, Part IV — Experimental Program and Comparison with Theory. VIDYA Report No. 172, Feb. 1965.

8. Chambers, J.; and Boisseau, P.: A Theoretical Analysis of the Dynamic Lateral Stability and Control of a Parawing Vehicle. NASA TN D-3461, 1966.

9. Kroo, I.; and Chang, L.: Analytical and Scale-Model Research Aimed at Improved Hang Glider Design. Proc. of the Third International Symposium on the Technology and Science of Low-Speed and Motorless Flight. NASA CP-2085, 1979.

10. Ormiston, R.: Wind Tunnel Tests of Four Flexible Wing Ultralight Gliders. NASA CP-2085, 1979.

11. LaBurthe, C.: Experimental Study of the Flight Envelope and Research of Safety Requirements for Hang Gliders. NASA CP-2085, 1979.

12. LaBurthe, C.; and Walden, S.: Etude de securite sur des planeurs ultra-legers de formule ROGALLO — Aerodynamique et mecanique du vol. ONERA RT 8/5134 SY, 1978.

13. Gillis, C.; Polhamus, E.; and Gray, J.: Charts for Determining Jet-Boundary Corrections for Complete Models in 7-by-10 Foot Closed Rectangular Wind Tunnels. NACA ARR L5G31, 1945.

23

14. Katzoff, S.; and Hannah, M.: Calculation of Tunnel-Induced Upwash Velocities for Swept and Yawed Wings. NACA TN-1748, 1948.

15. Weinberg, J.: Wind Tunnel Wall Corrections in the Ames 7-by-10 Foot Wind Tunnels. Memo for Files, NACA Ames Aeronautical Laboratory, 1950.

16. Pope, A.; and Harper, J.: Low-Speed Wind Tunnel Testing. Wiley and Sons, Inc., 1966.

17. Rigamonti, N.; and Pflugshaupt, H.: Investigation of the Steady-State Behavior of Two Delta-Wing Hang Gliders. NASA TT F-17394, 1977.

18. Ormiston, R.: Theoretical and Experimental Aerodynamics of an Elastic Sailwing. Ph.D. Thesis, Dept. of Aerospace and Mechanical Sciences, Princeton Univ., 1969.

19. Hoerner, S.: Fluid Dynamic Drag, Pub. by Author, 1965.

20. Schmitz, F.: Aerodynamics of the Model Airplane. Part I, Airfoil Measurements. Berlin, 1942.

21. Eppler, R.: Some New Airfoils. In: Tech. and Science of Low Speed and Motorless Flight. NASA CP-2085, 1979.

22. Libby, C.; and Johnson, J.: Stalling and Tumbling of a Radio-Controlled Parawing Airplane Model. NASA TN D-2291.

23. Phillips, W. H.: Recovery from a Vertical Dive. Ground Skimmer (now Hang Gliding), Aug. 1975.

24. Phillips, W. H.: More on Dive Recovery or Lack Thereof. Ground Skimmer, Nov. 1975.

25. Phillips, W. H.: Stability and Control of Hang Gliders. Paper presented at Society of Automotive Engineers Meeting, Sept. 1976.

26. Jones, R. T.: Dynamics of Ultralight Aircraft — Dive Recovery of Hang Gliders. NASA TMX-73229, 1977.

27. Valle, G.: Flight Testing for HGMA Certification and HGMA Specification and Compliance Program. Hang Gliding, Jan. 1977.

28. Valle, G.: A Preliminary Analysis of the Longitudinal Dynamics of Ultralight Gliders. Hang Gliding, March 1979.

TABLE 1.– DESCRIPTION OF CONFIGURATIONS

Config-uration	Basic planform	Tip geometry	Battens	Luff lines	Keel pocket	Dihedral
1	Standard, (fig. 2)		None	None	No	No
2A	30° sweep (fig. 3)	21° min tip washout	Spruce	To first batten set	Yes	No
2B		24° min tip washout		To first batten set		
2C		↓		None		
2D		21° min tip washout				
2E		No fixed twist tips		↓		
2F				To first batten set		
2G		↓	↓	Shortened luff lines		
2H		24° min tip washout	Cambered ribs replace batten set 2	To first batten set		
2I			Flexible plastic battens in sets 1, 2, 3			
2J			Plastic battens in set 1; spruce in sets 2 and 3			
2K			Rigid cambered ribs sets 1, 2, 3		↓	
2L			Spruce		No	
2M			Plastic battens set 1	↓		
2N	↓	↓	Spruce	To 2nd batten set	↓	↓

TABLE 1.- Concluded.

Configuration	Basic planform	Tip geometry	Battens	Luff lines	Keel pocket	Dihedral
20	30° sweep (fig. 3)	24° fixed twist	Spruce	To 1st batten set	No	No
2P		12° fixed twist				
2Q		24° min tip washout		None		3.5° per side
3A	Low sweep design (fig. 4)	No fixed tips		To batten set 1		No
3B				None		
3C				To batten set 2		
3D				To batten sets 1 & 2		
3E			Cambered ribs	None		
3F			Cambered ribs	To batten set 3		
3G			Cambered ribs with increased camber and reflex			
3H				None		
3I				None		3.5° per side

NOTES:

1. Batten sets are numbered from the root with the pair of battens closest to the root labeled set 1.

2. Tip twist is measured w.r.t the keel reference; the large keel pocket produces a 9° angle between root chord and keel.

3. Since dihedral was added by simply lengthening the lower wires and tightening the upper wires, some additional billow was introduced. This is reflected in the drag data.

26

Kingpost (.48 cm stainless steel)

Cable (7x7 .16 cm aircraft cable)

Sleeve {Model 1: 6.0 cm x 1.1 cm OD
{Models 2,3: 12.7 cm x 1.1 cm OD
[304 stainless steel]

Leading edge
(cold rolled steel)
.79 cm diam: Model 1
.95 cm diam: Models 2,3

Cross bar (same
material as
leading edge)

Keel (material same as leading edge)

Control bar (.48 cm stainless steel)

27
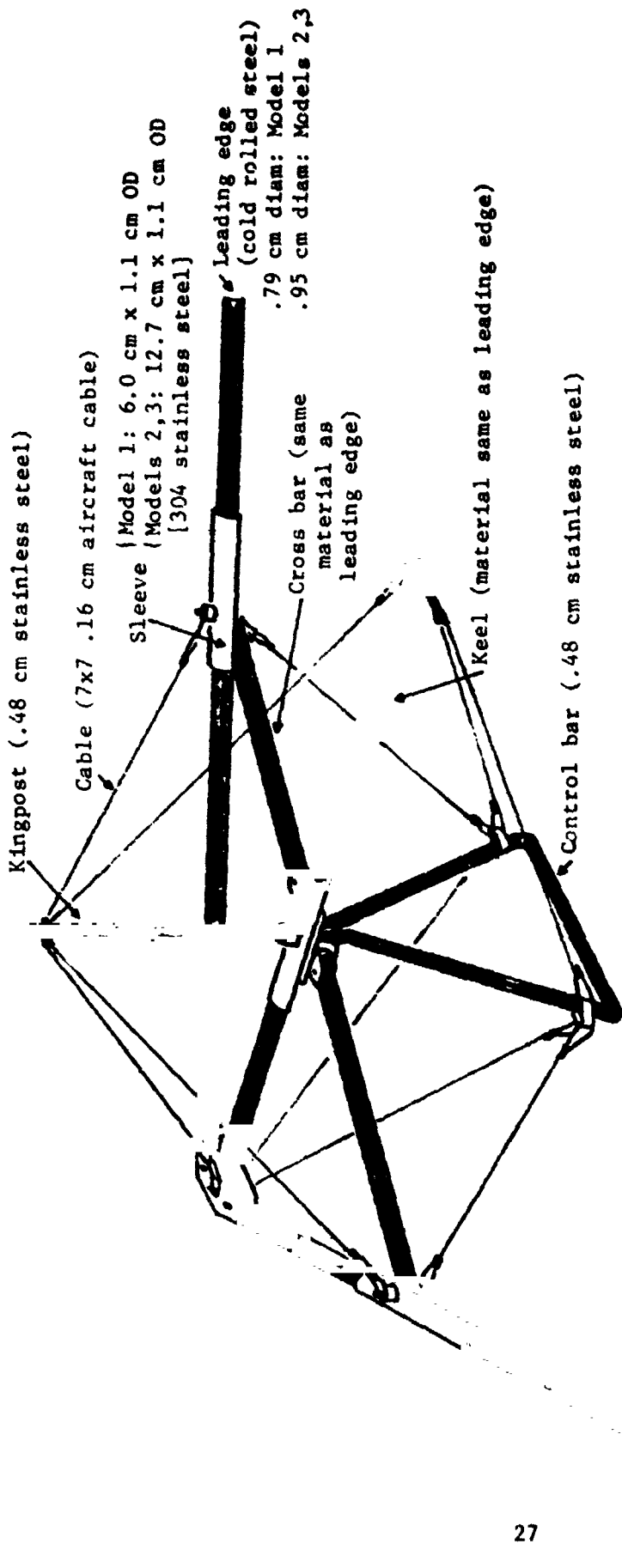
Figure 1.- Frame construction details.

MODEL # 1

PROJECTED PLANFORM:

$S = .74 \, m^2 \quad (8.00 \, ft^2)$

$b = 1.43 \, m \quad (4.69 \, ft)$

$AR = 2.75$

$\bar{c} = .52 \, m \, (1.71 \, ft)$

$\Lambda_{LE} = 50°$

APPROXIMATE TRAPEZOIDAL WING:

$\lambda = 0.0$

$\Lambda_{c/4} = 40°$

$MAC = .69 \, m \quad (2.27 \, ft)$

Ref.
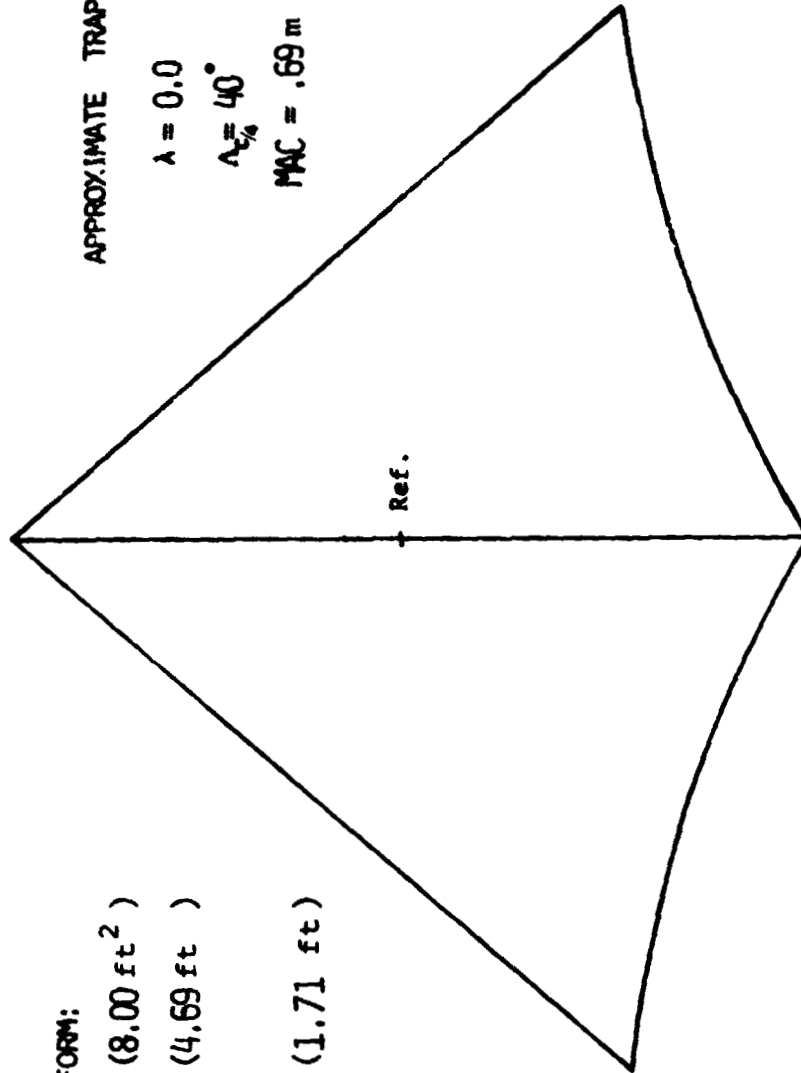
Figure 2.- Model 1 "standard configuration" planform and geometric characteristics.

MODEL # 2
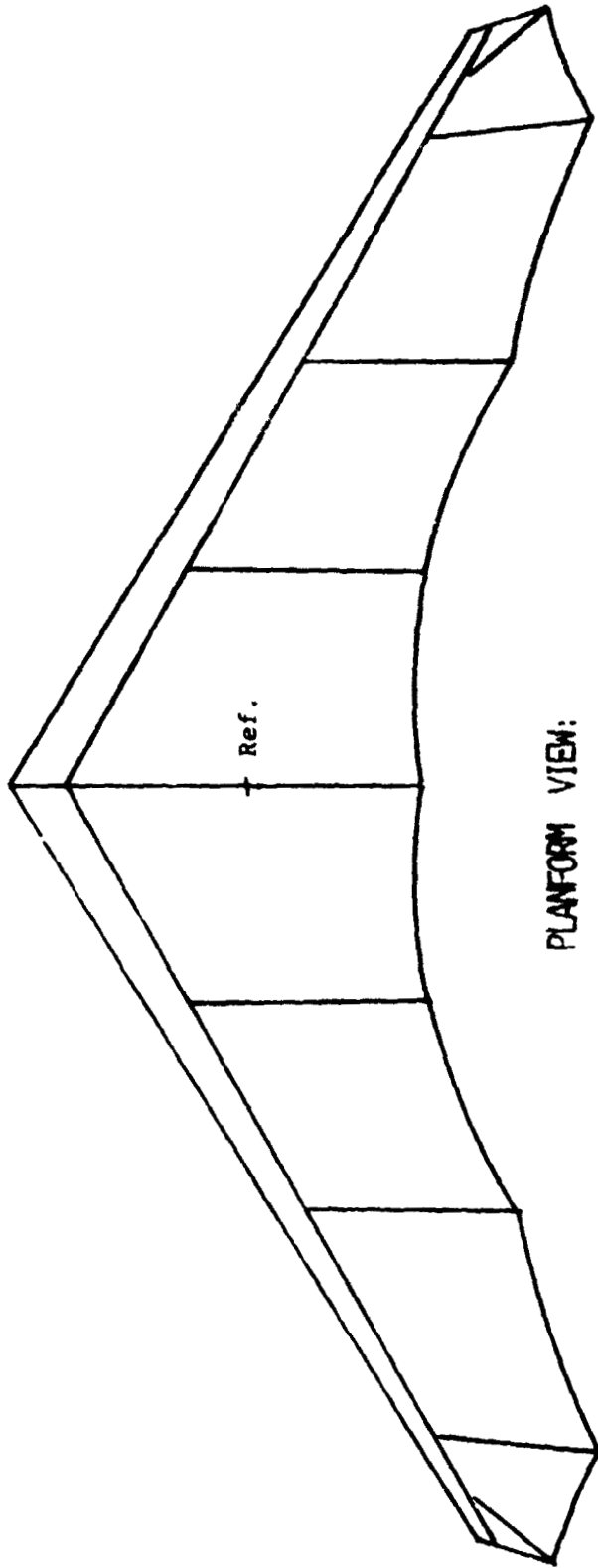
PLANFORM VIEW:

$S = .72 \ m^2 \quad (7.77 \ ft^2)$

$b = 2.10 \ m \quad (6.88 \ ft \ )$

$\Lambda_{LE} = 32.5$

$\bar{c} = .34 \ m \quad (1.13 \ ft \ )$

$AR = 6.1$

$\lambda \approx .34$

$MAC \approx .38 \ m \quad (1.25 \ ft \ )$

$\Lambda_{C/4} \approx 28.5$

Figure 3.- Model 2 planform and geometric characteristics.

MODEL # 3

Ref.
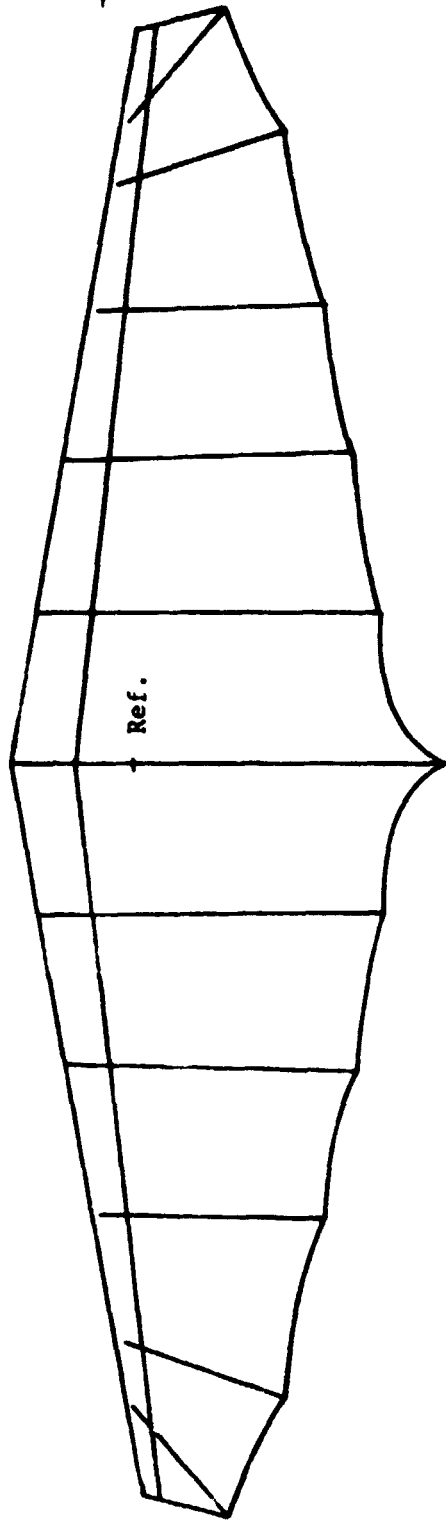
PROJECTED PLANFORM:

$S = .72 \text{ m}^2 \quad (7.80 \text{ ft}^2)$

$b = 2.03 \text{ m} \quad (6.67 \text{ ft})$

$\Lambda_{LE} = 10°$

$\bar{c} = .36 \text{ m} \quad (1.17 \text{ ft})$

$AR = 5.7$

APPROXIMATE TRAPEZOIDAL WING:

$\lambda = .28$

$MAC = .39 \text{ m} \quad (1.29 \text{ ft})$

$\Lambda_{C/4} = 4.6°$

Figure 4.— Model 3 planform and geometric characteristics.

fixed-twist rib
holds minimum
washout in sail

fixed-twist rib

leading edge

keel

sail
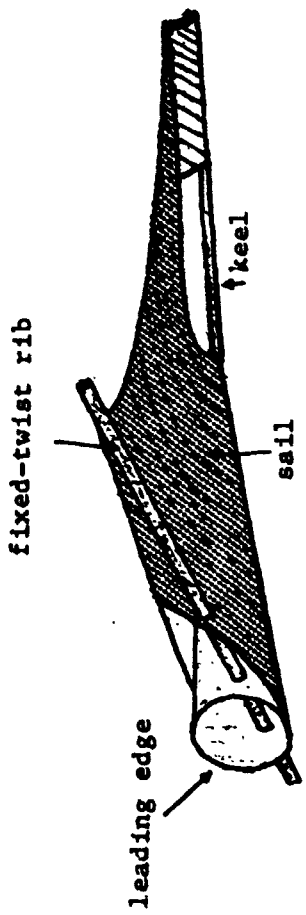
Figure 5.- Fixed-twist ribs.

31

luff lines

sail shape at positive
angles of attack

luff lines

sail shape under
negative loads
with luff lines
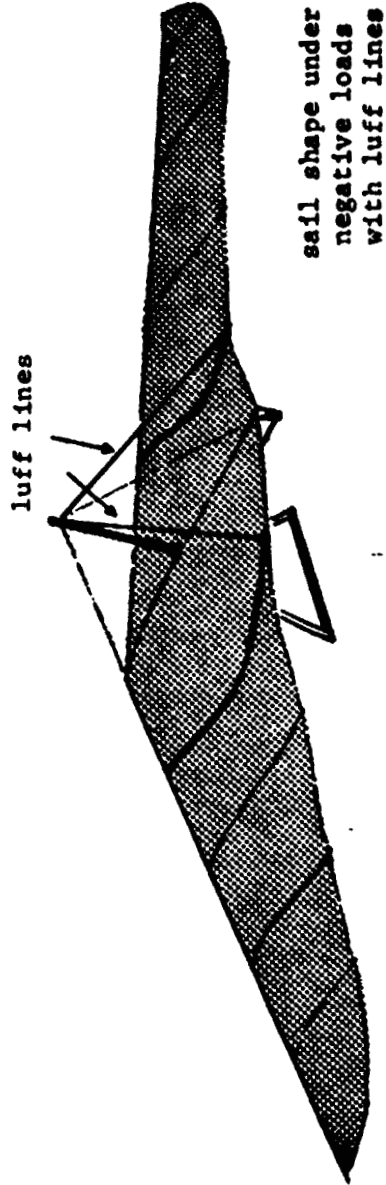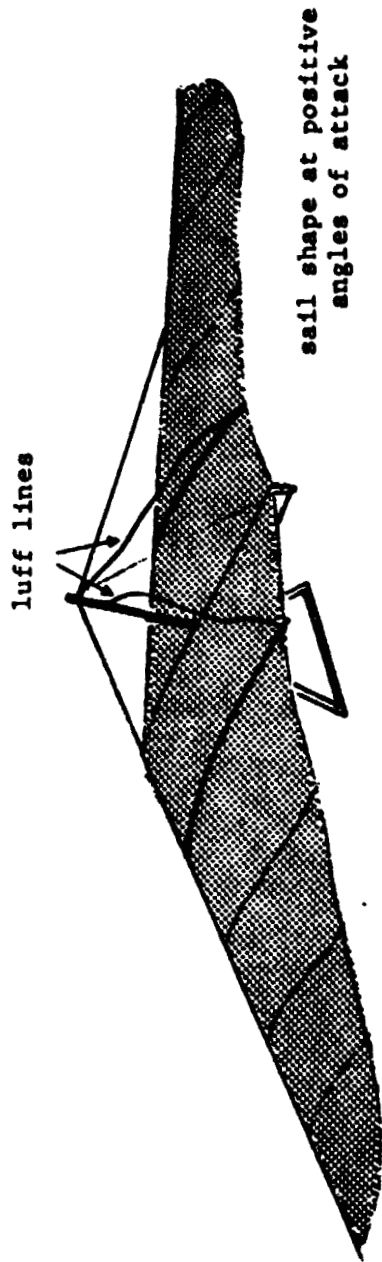
Figure 6.- Luff line geometry.

32

keel pocket

sail deformation
with keel pocket
under asymmetric loading
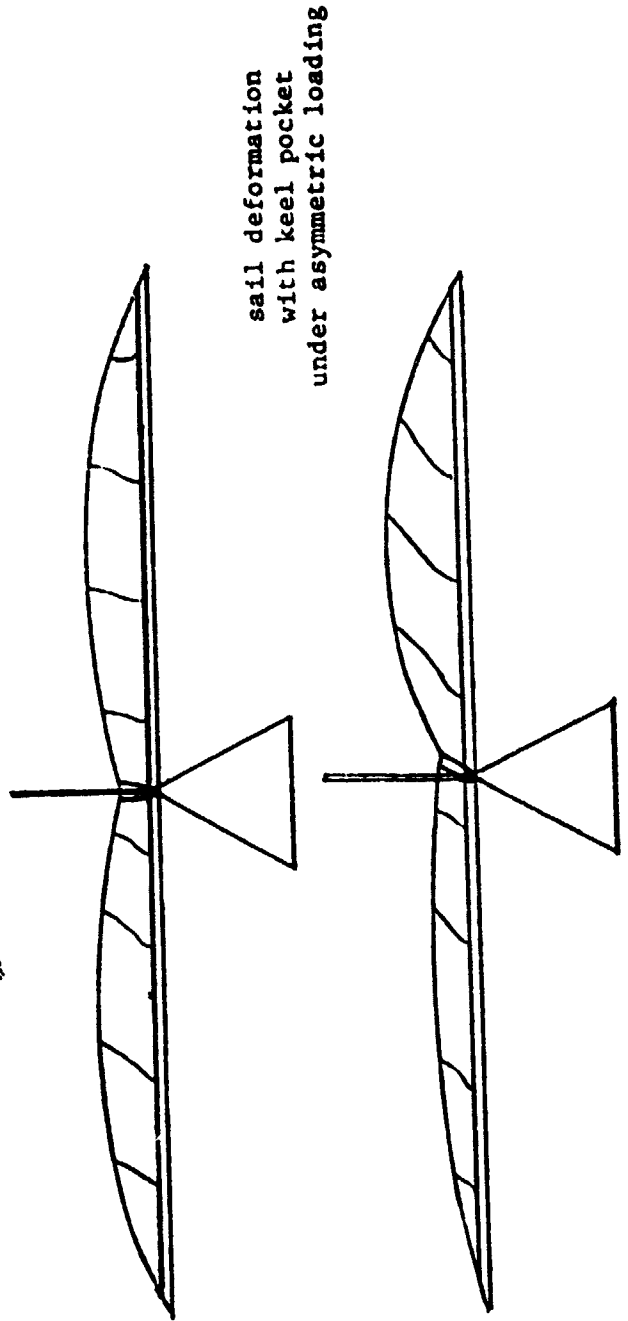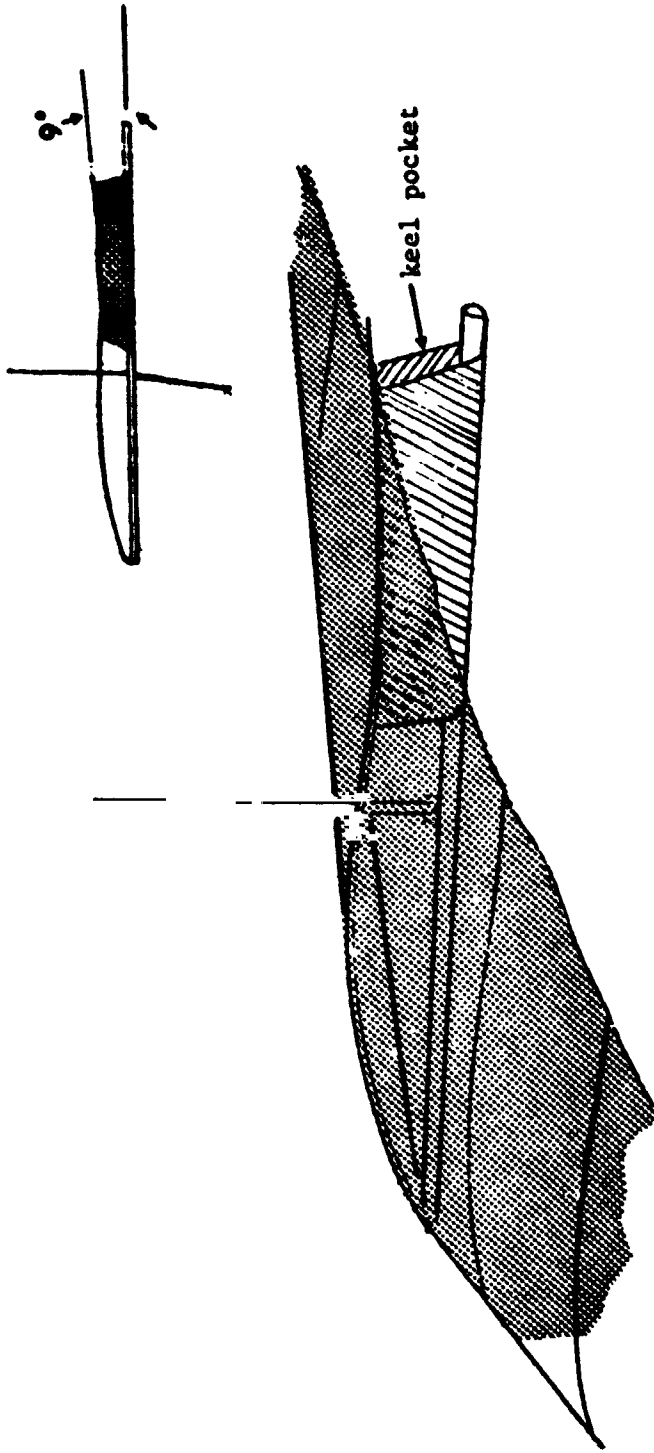
Figure 7.- Keel pocket.

33
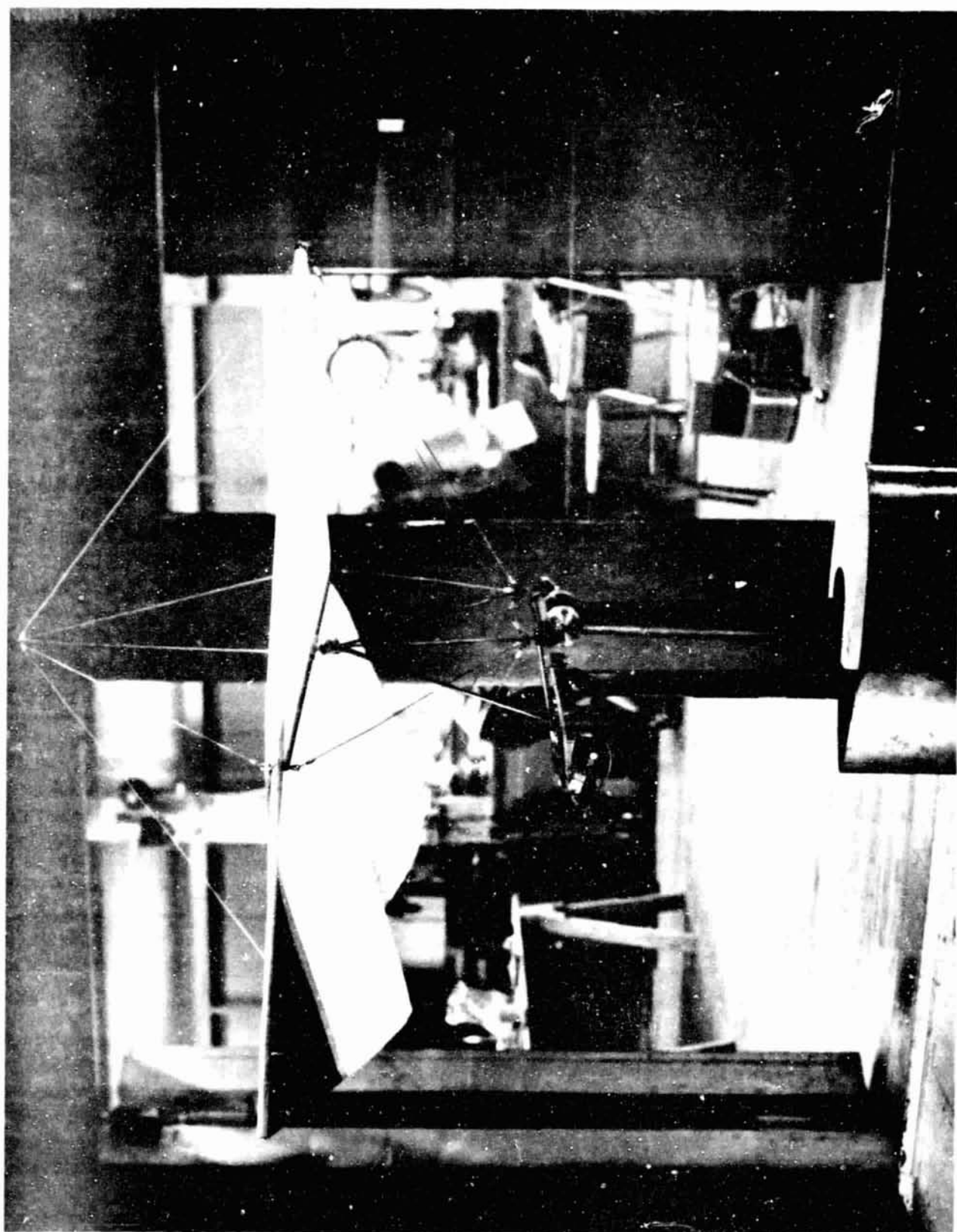
Figure 8.- Strut mount.

34
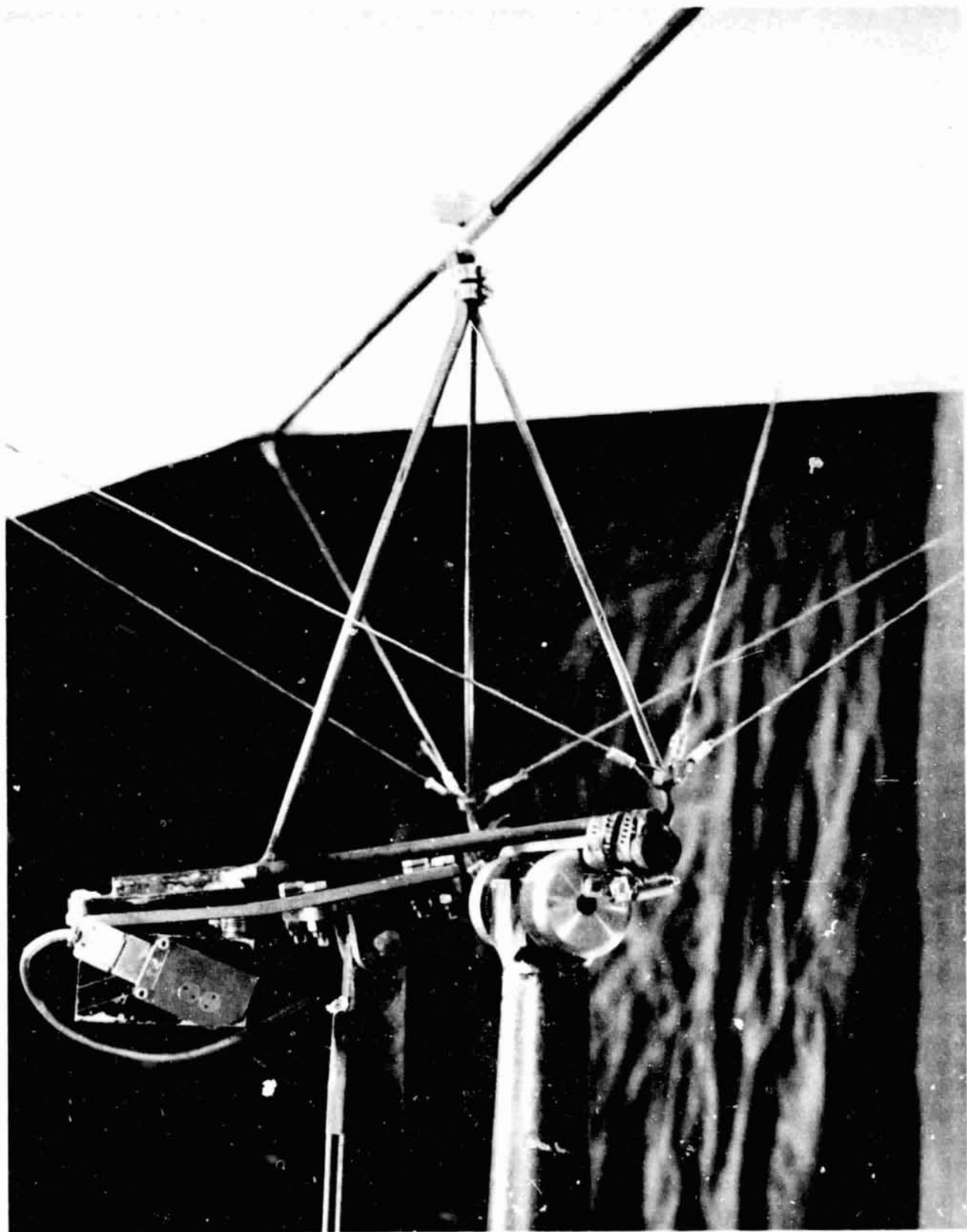
Figure 9.- Detail of mount.

35
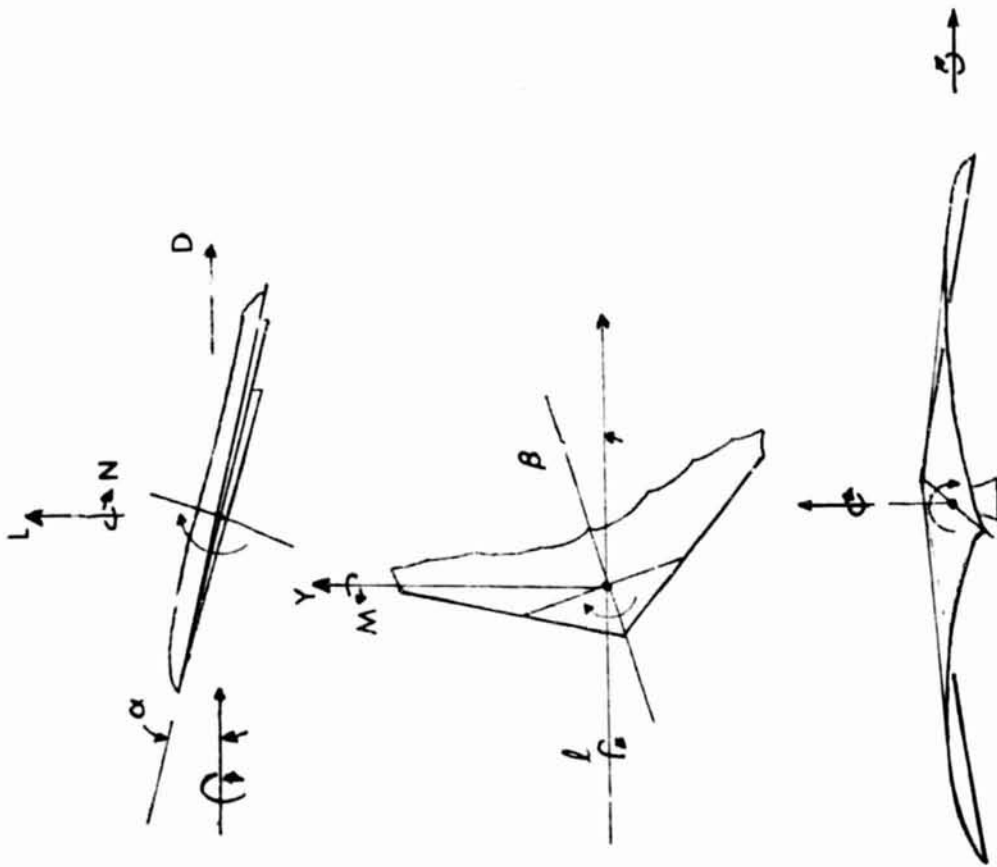
Figure 10.- Wind axes system.

36
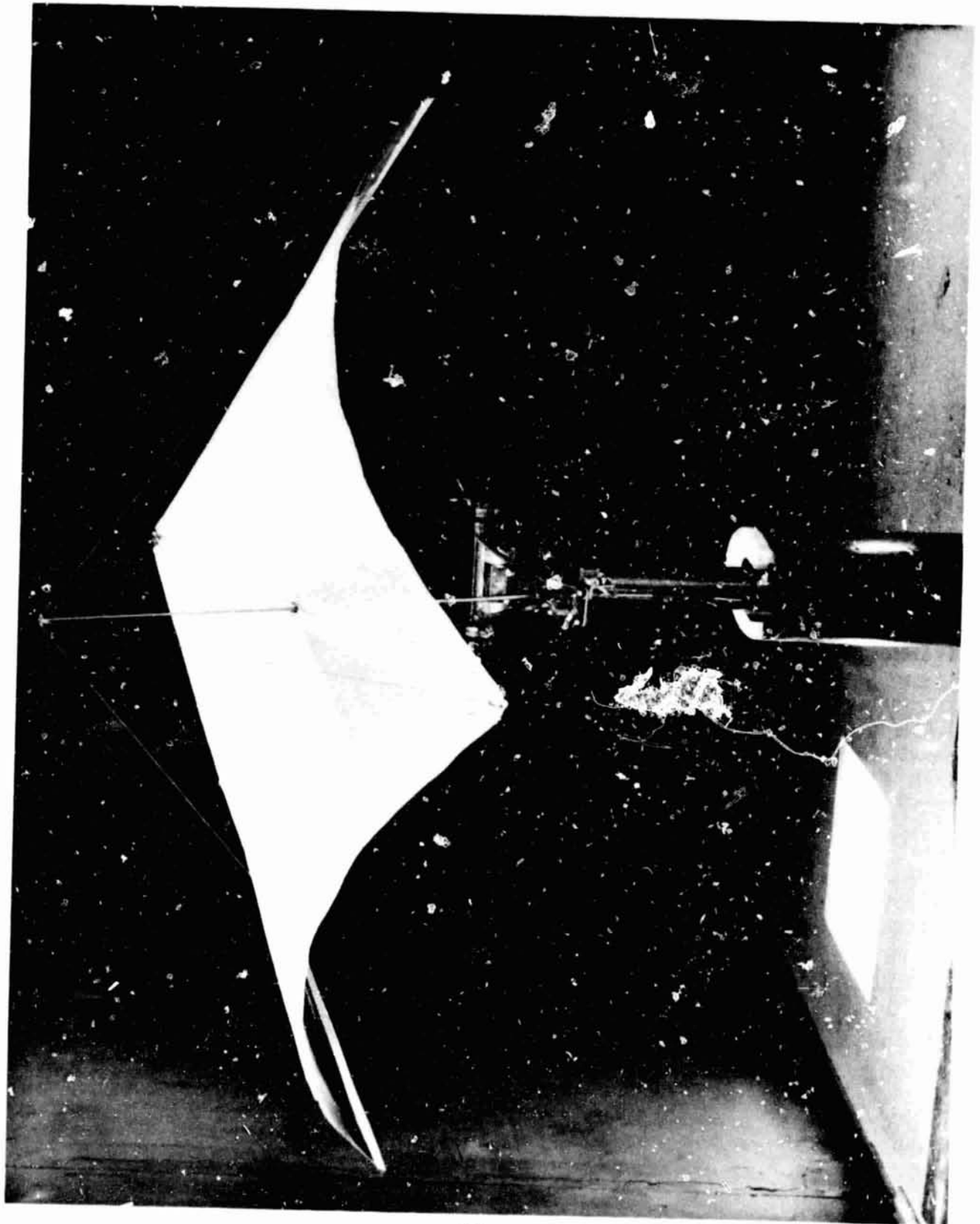
Figure 11.- Model 1 installation.
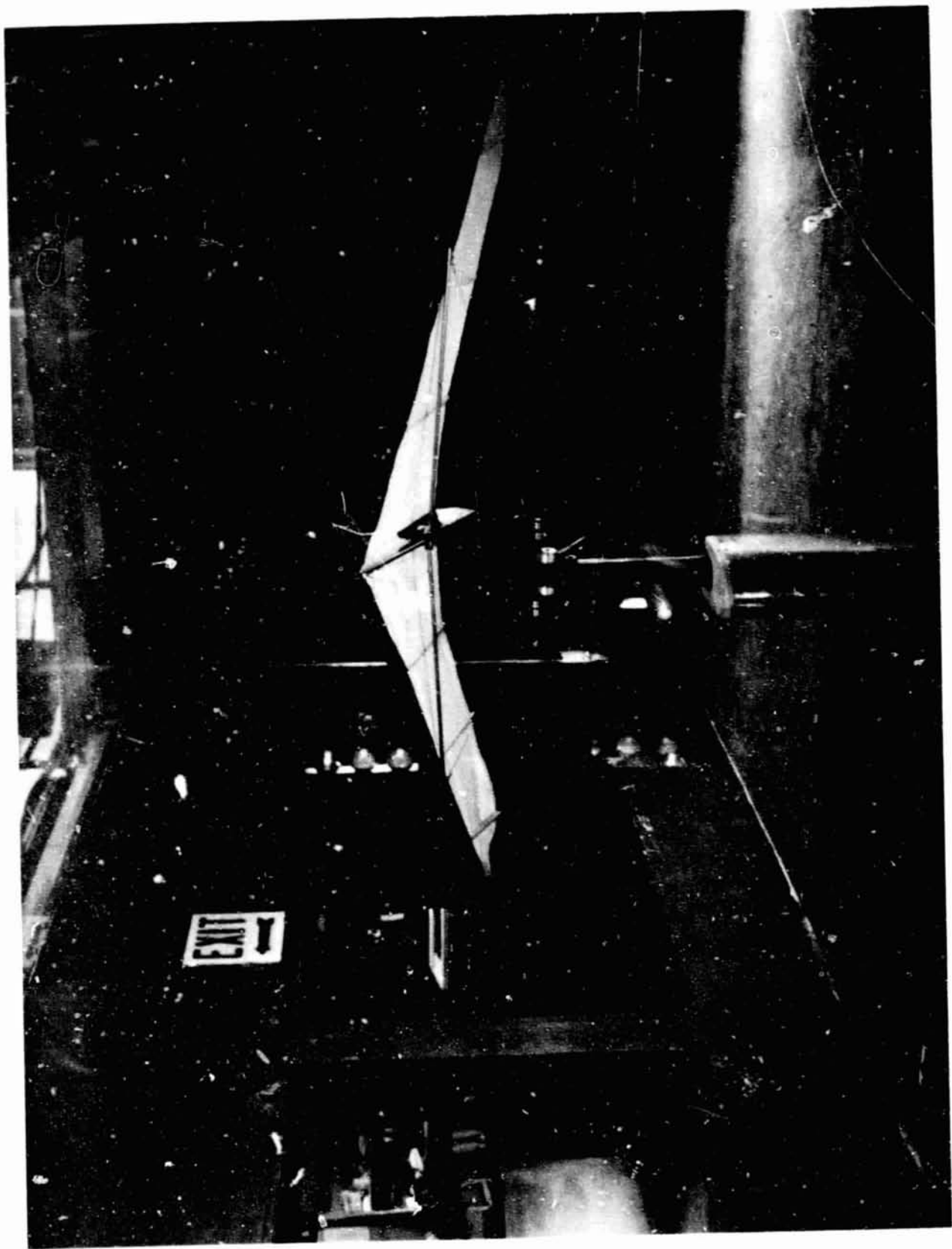
Figure 12.- Model 2 installation.
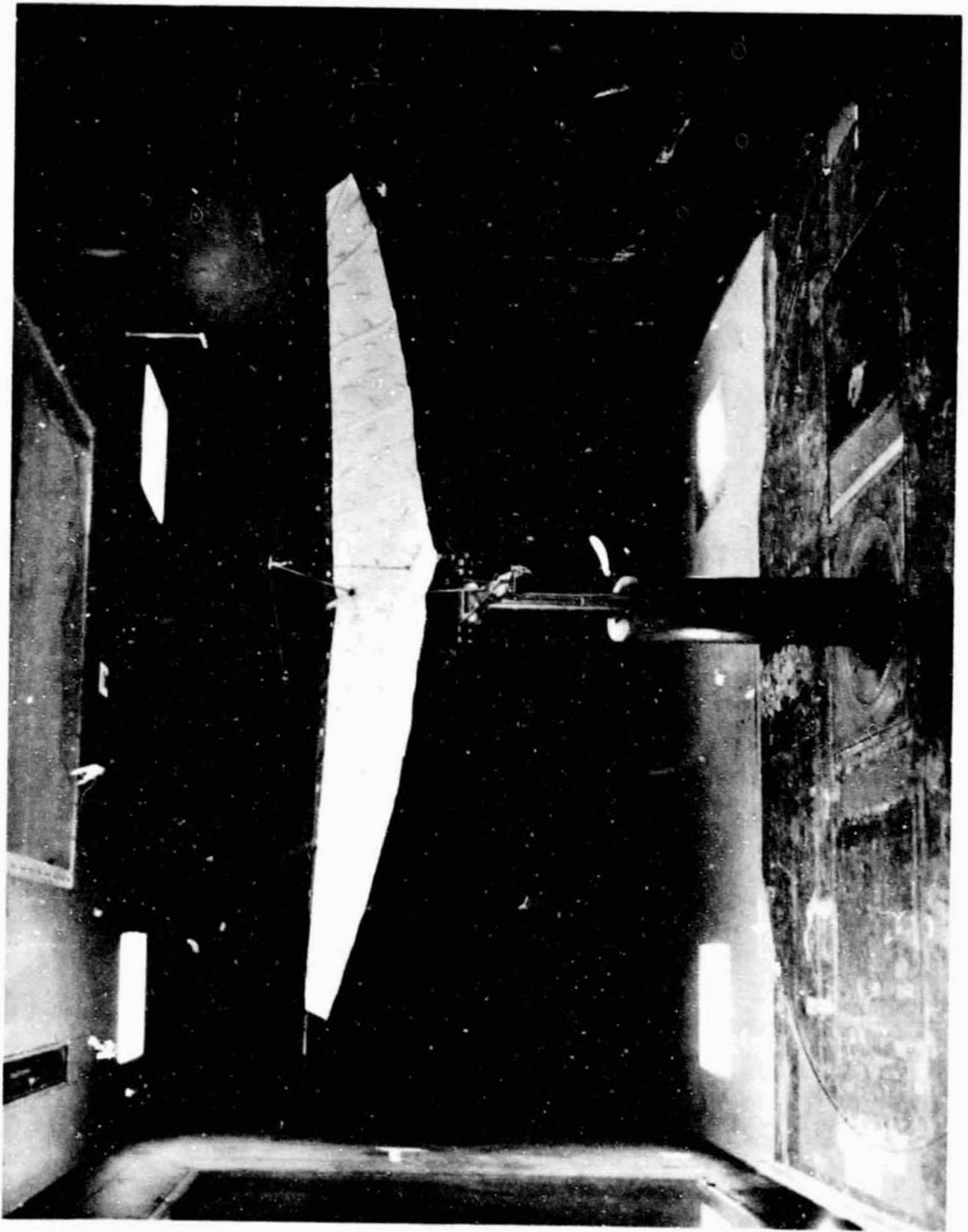
Figure 13.- Model 3 installation.
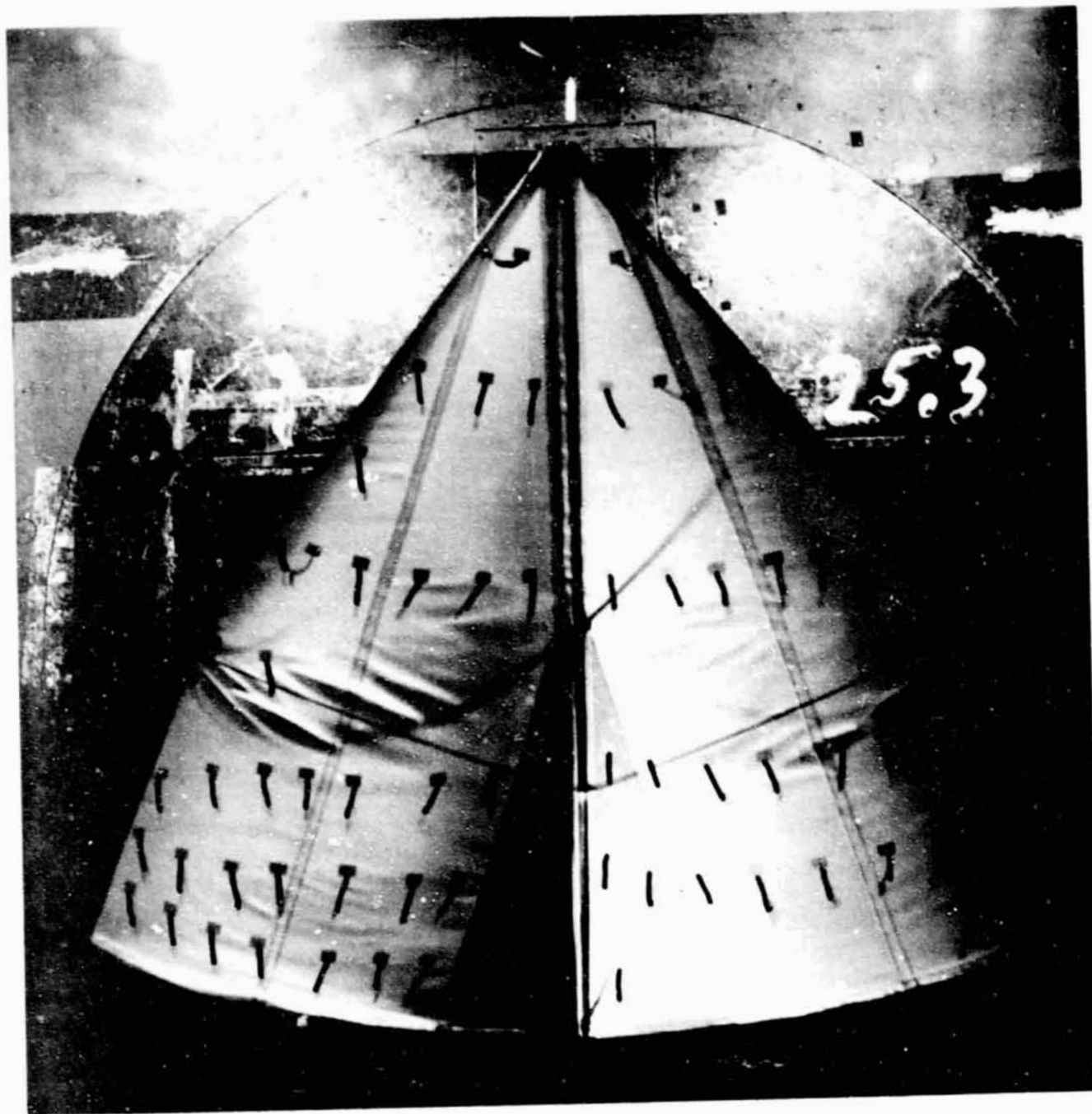
(a) $\iota = 25.3°$

Figure 14.- Tuft pattern, standard configuration.
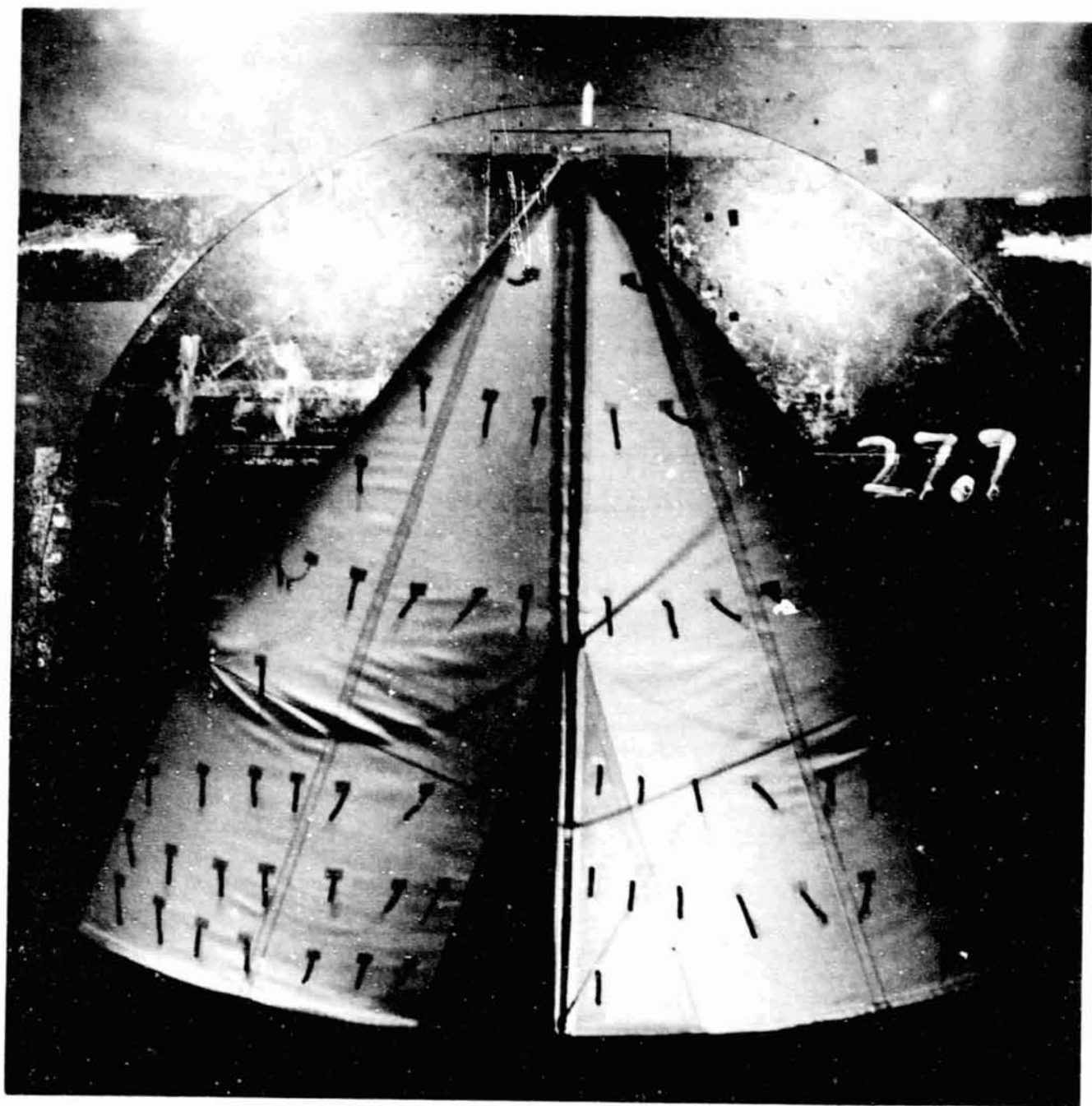
(b) $\alpha = 27.7°$

Figure 14.- Continued.
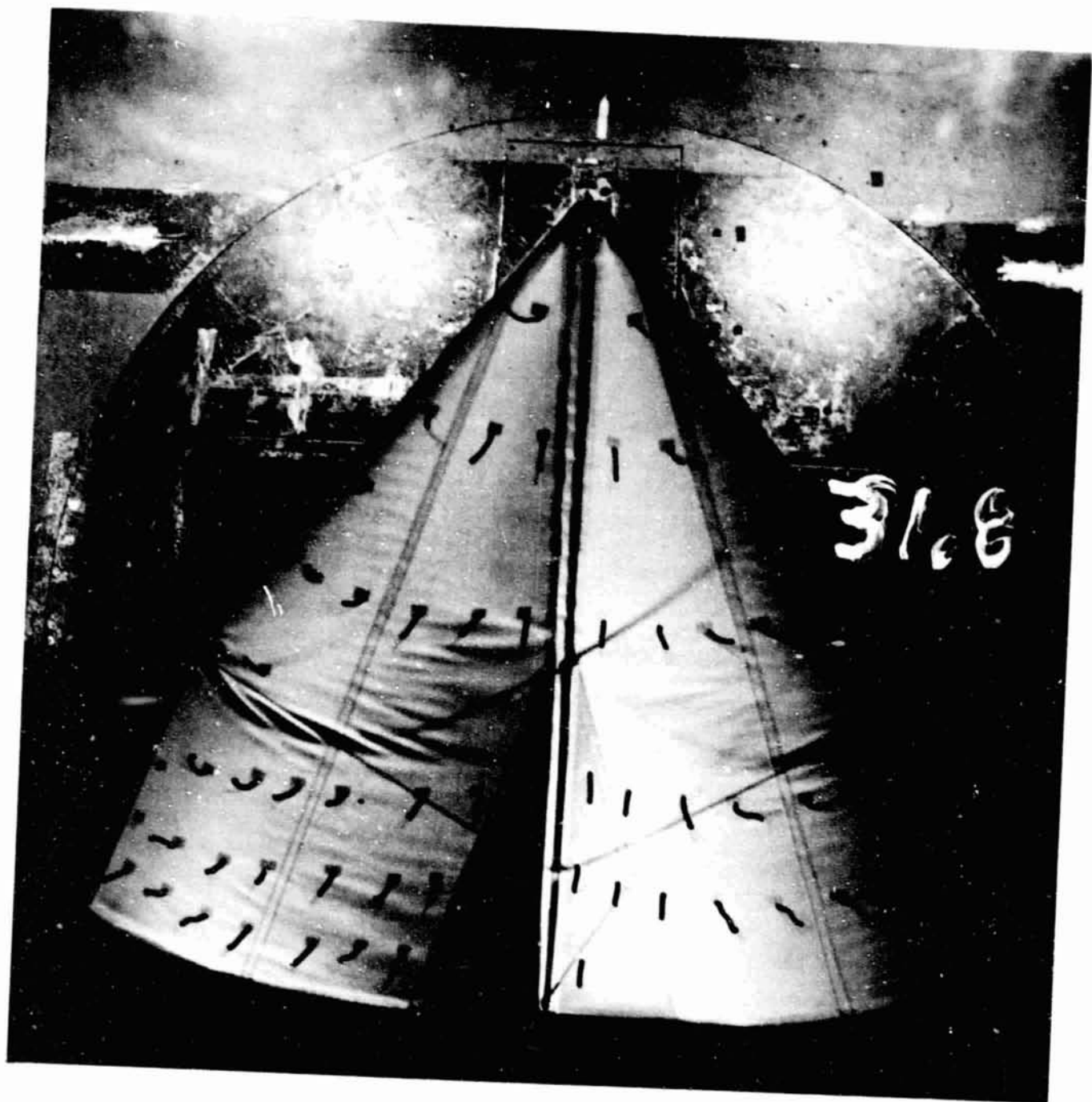
(c) $\alpha = 31.8°$

Figure 14.- Continued.
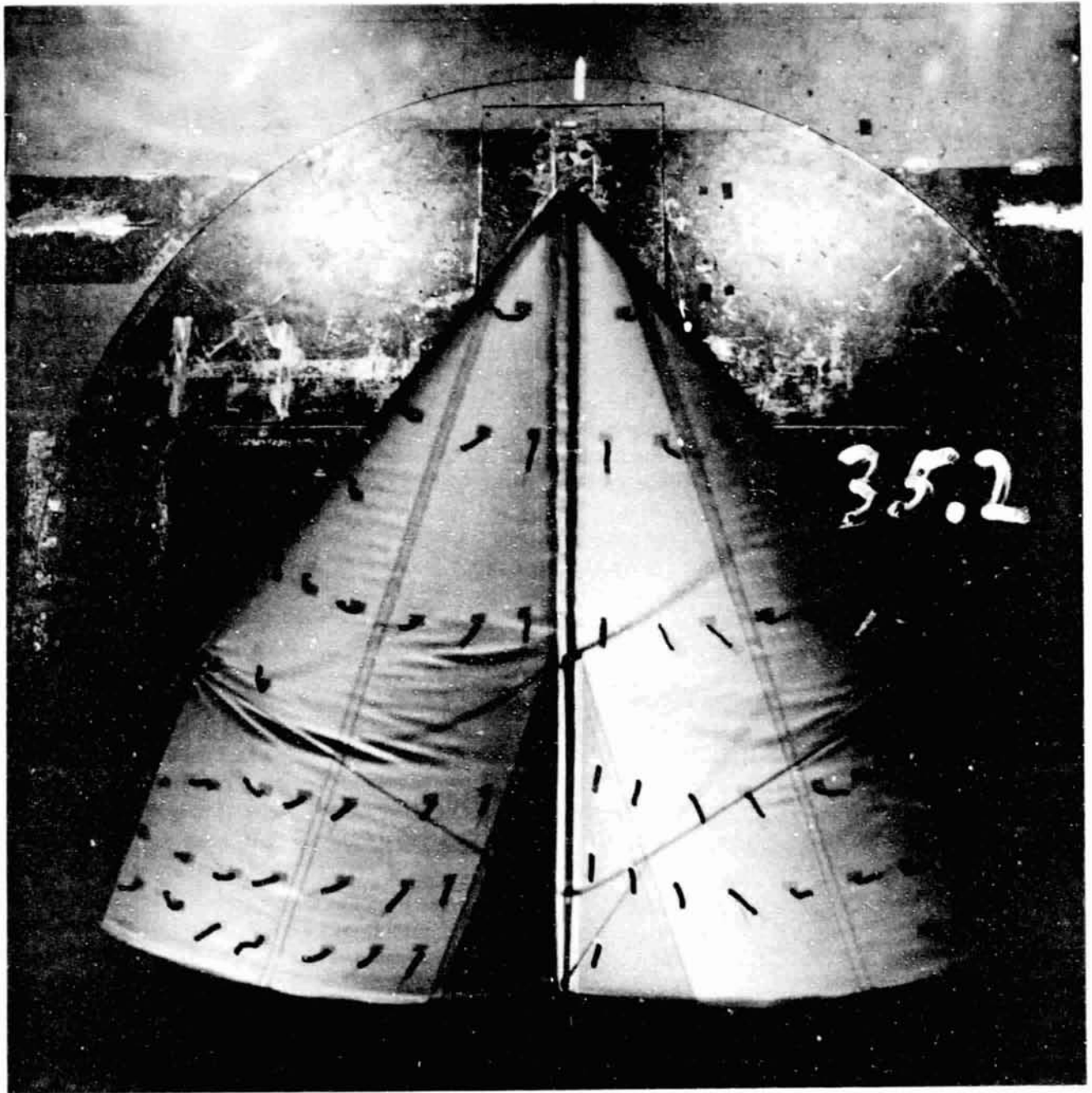
(d) $\alpha = 35.2°$

Figure 14.- Continued.
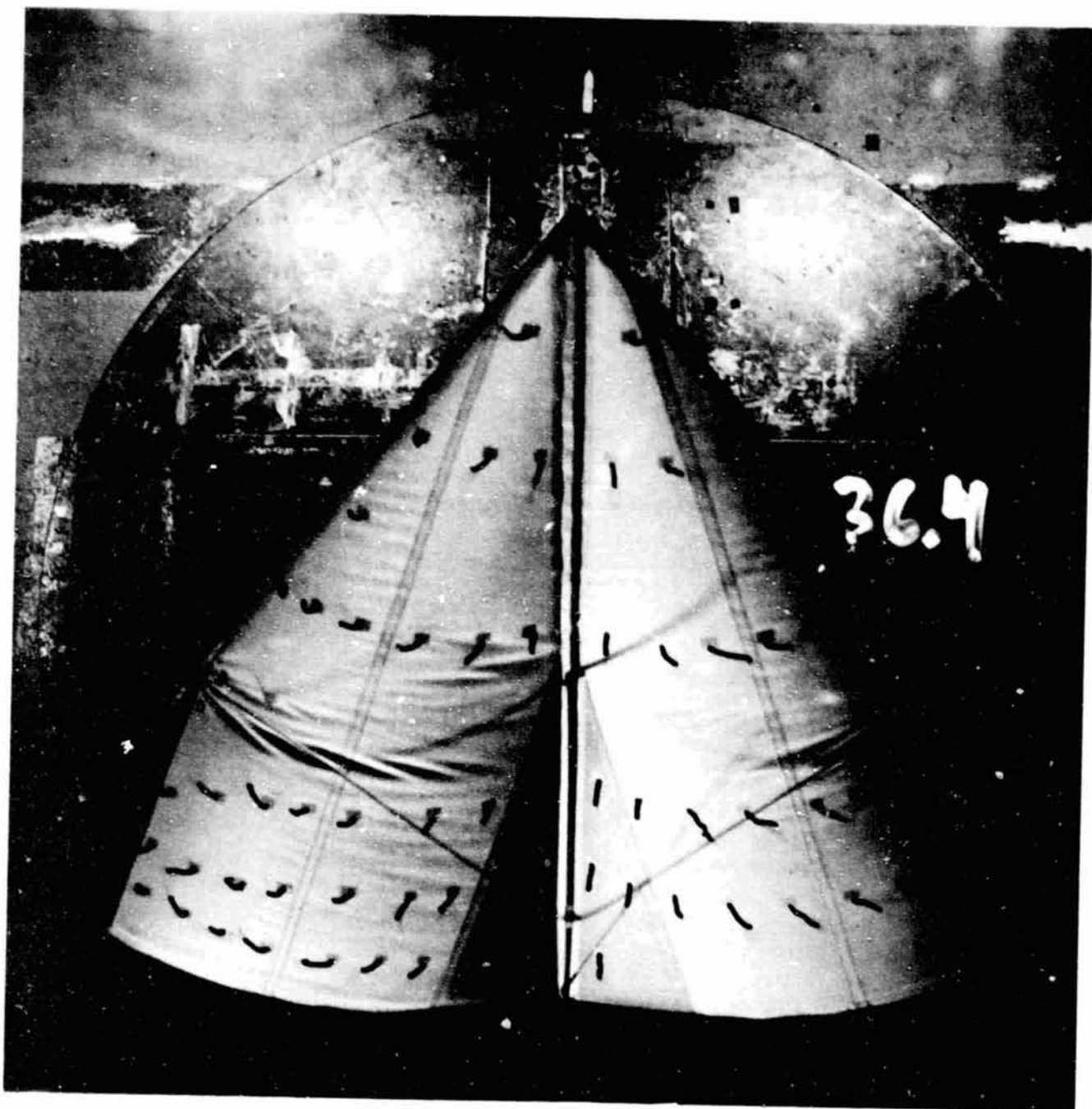
(e) $\alpha = 36.4°$

Figure 14.- Continued.
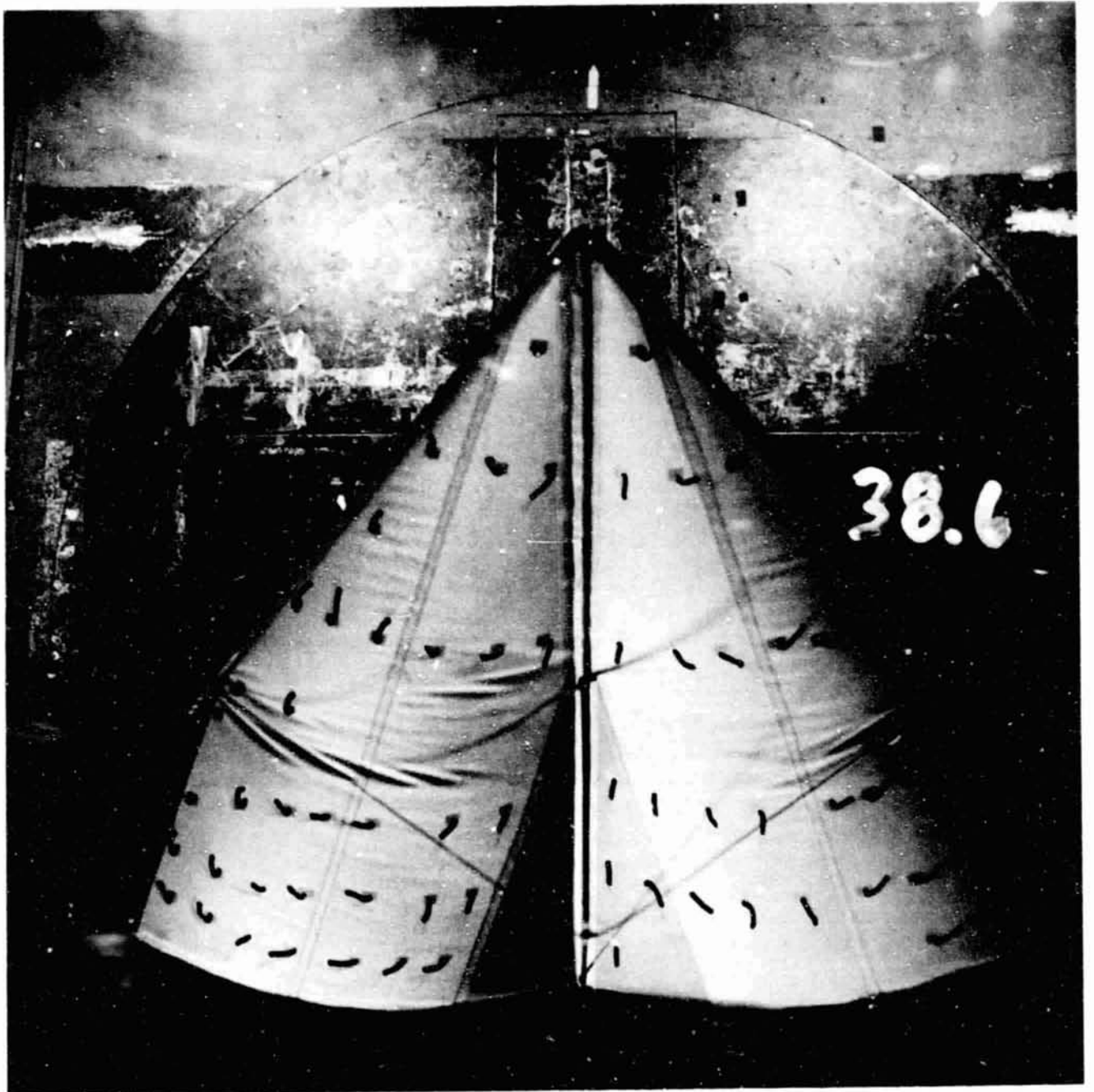
(f) $\alpha = 38.6°$

Figure 14.- Continued.
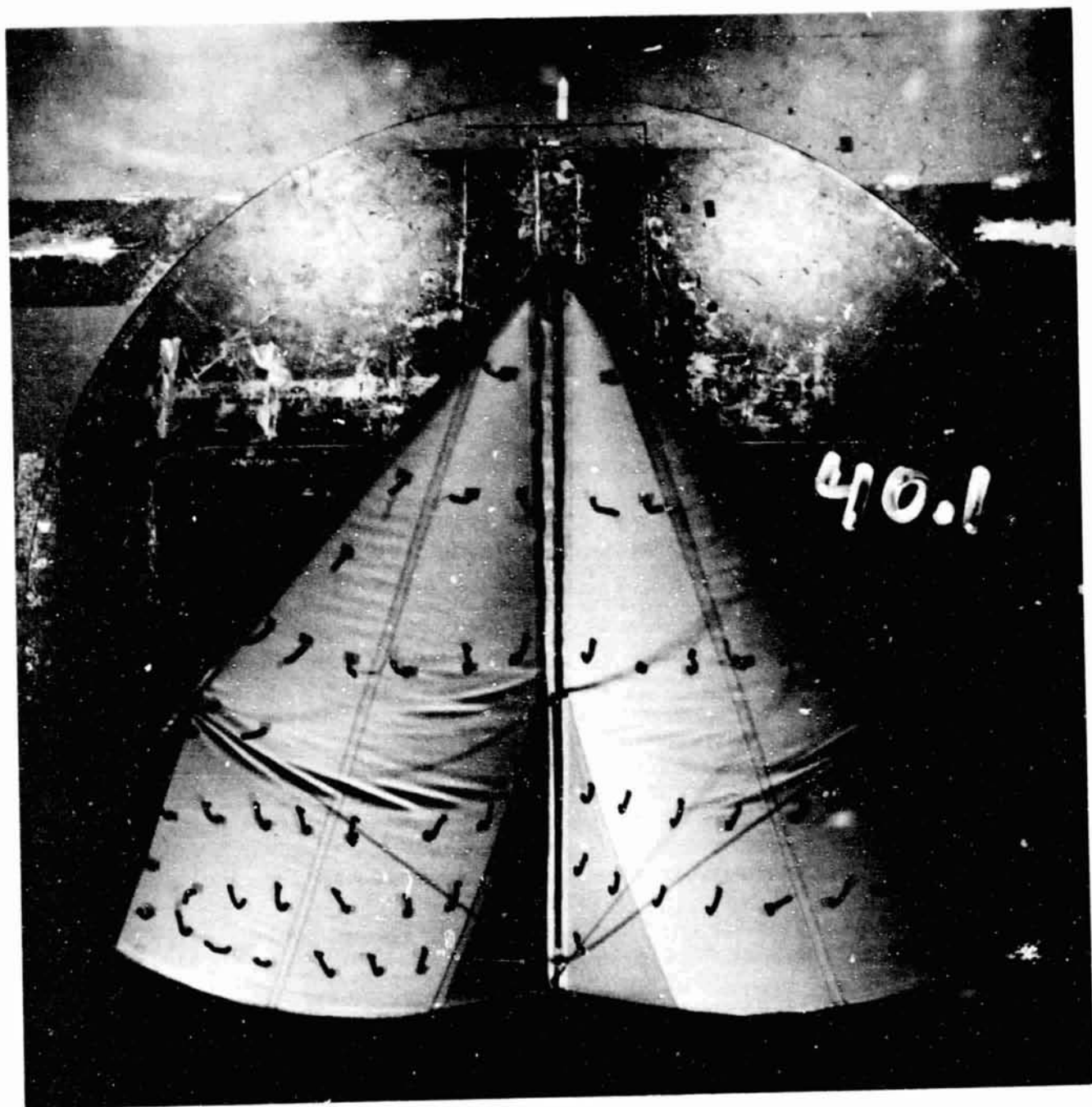
(g) $a = 40.1°$

Figure 14.- Concluded.
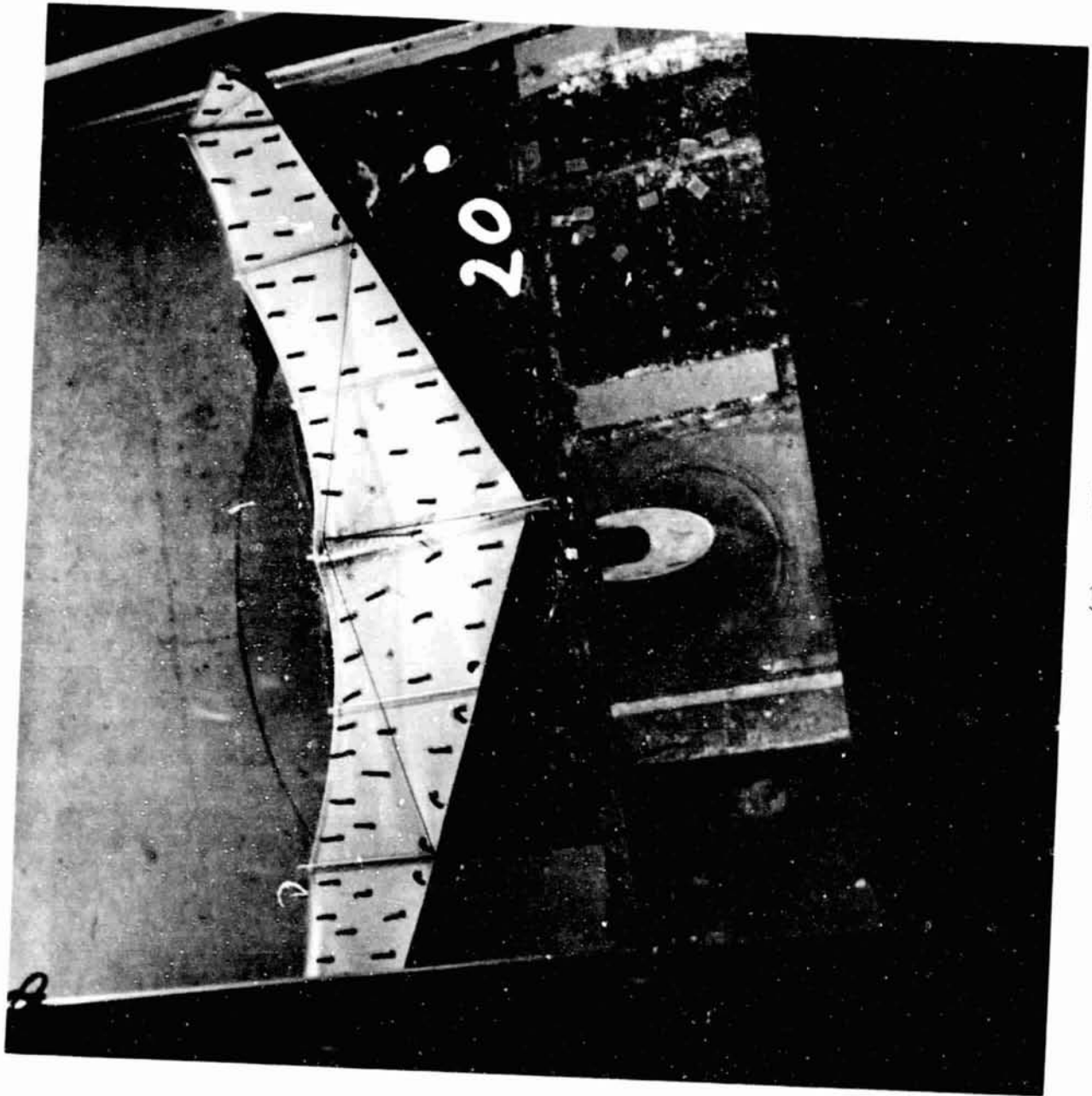
(a) $\alpha = 20°$

Figure 15.- Tuft pattern, configuration 2A.
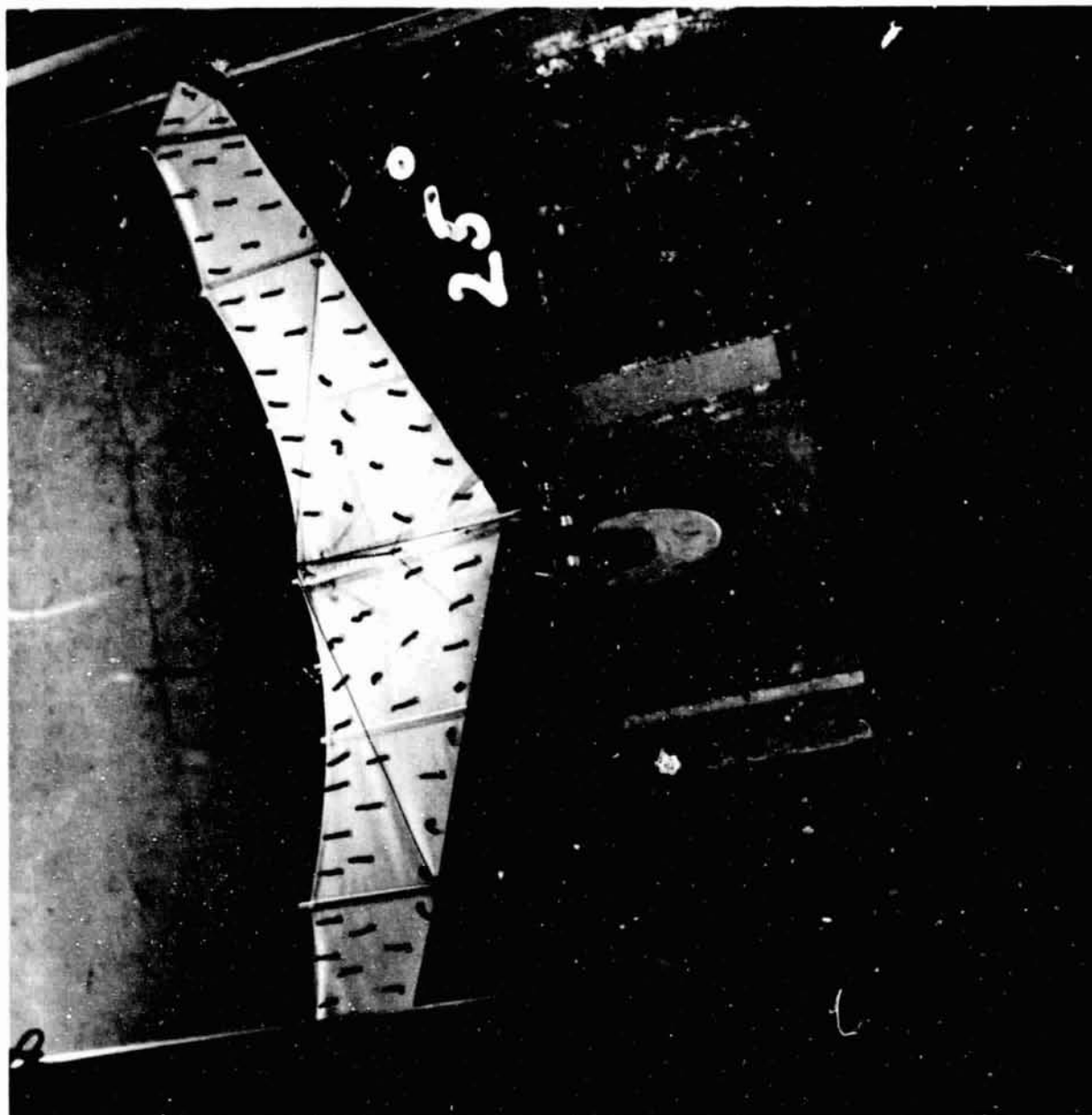
(b) $\alpha = 25°$

Figure 15.— Continued.
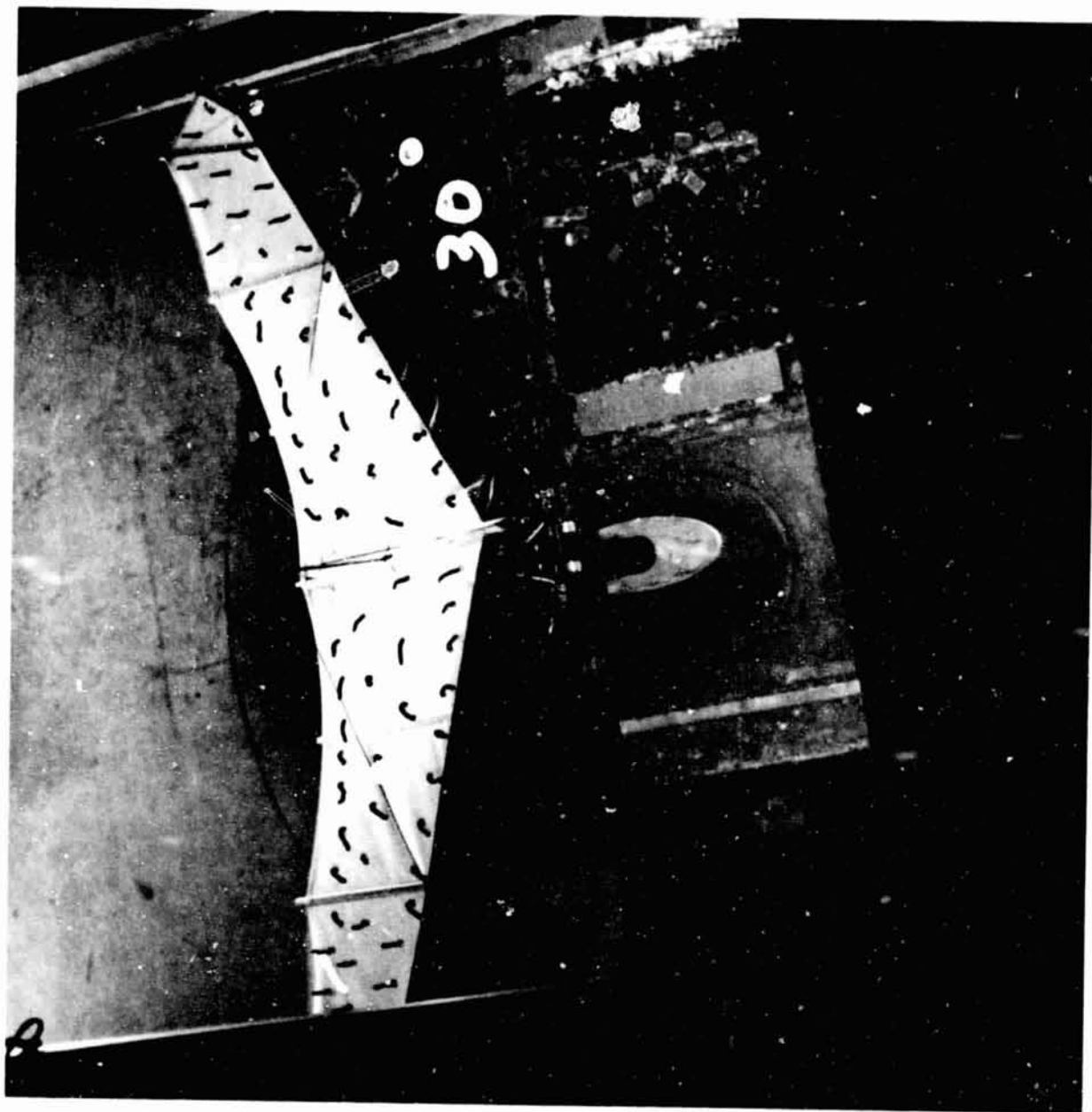
(c) $\alpha = 30°$

Figure 15.– Continued.

49
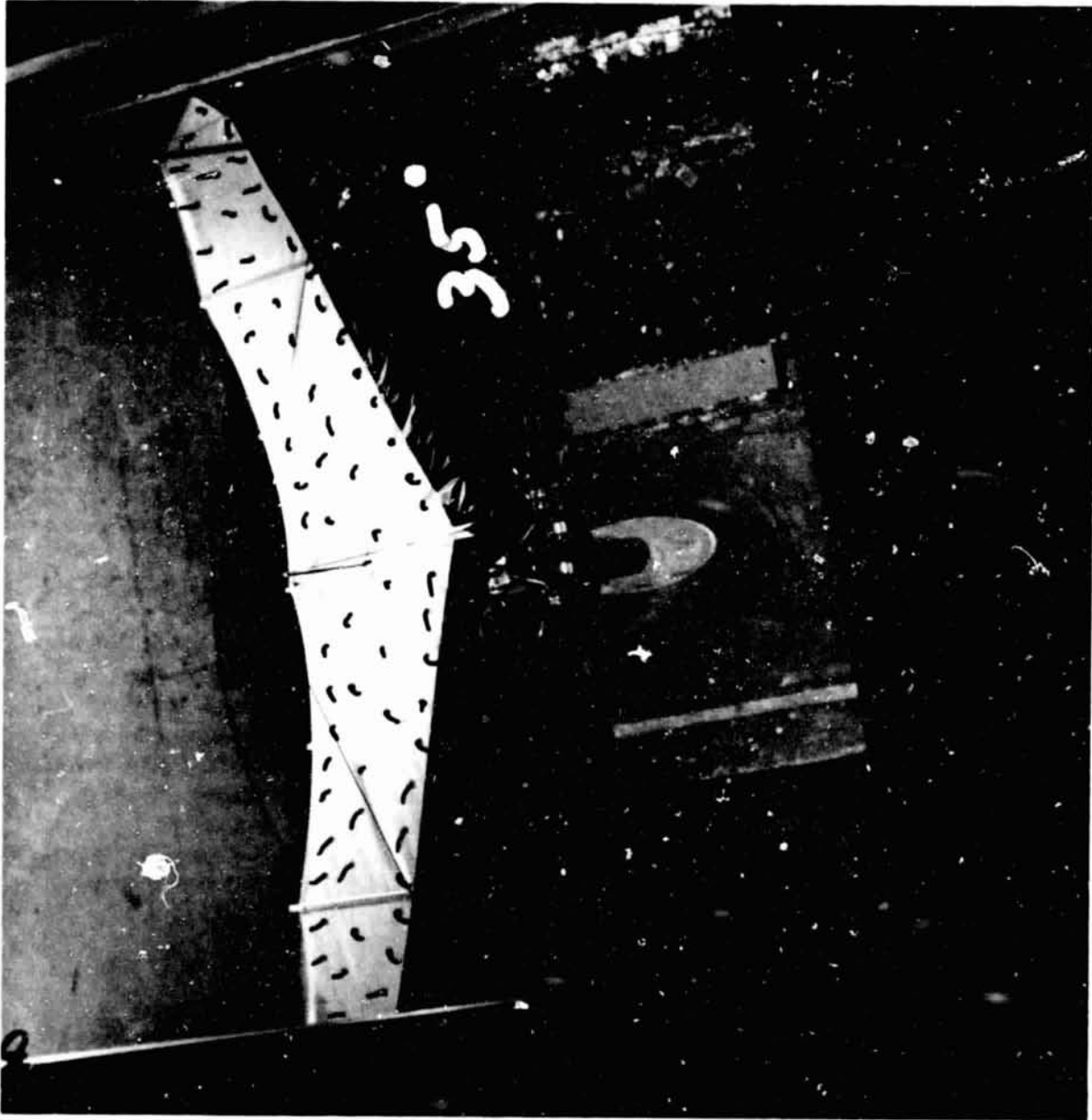
(d) $\alpha = 35°$

Figure 15.- Concluded.
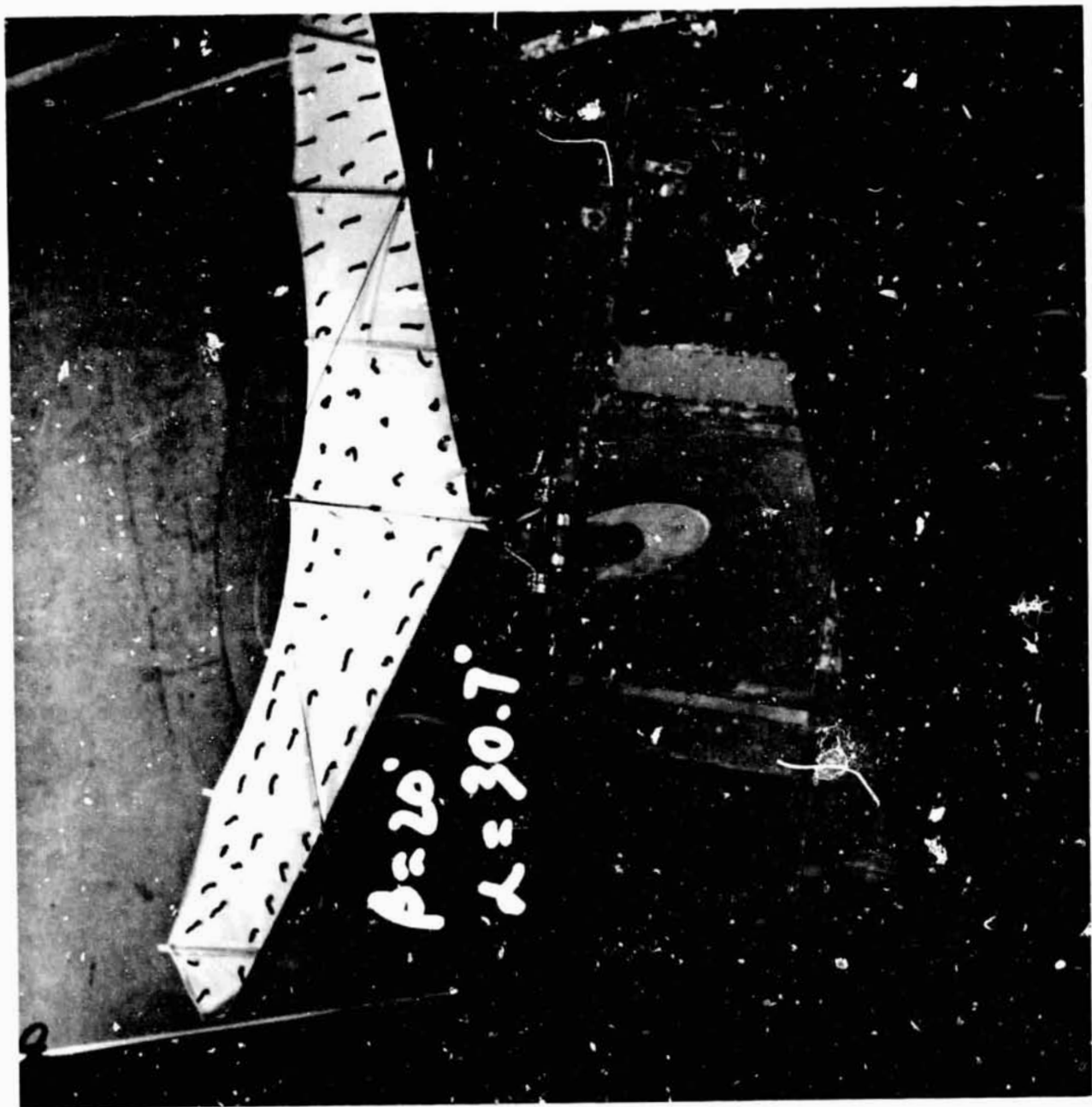
Figure 16.- Tuft pattern, configuration 2A; $\alpha = 30.7°$, $\beta = 20°$.
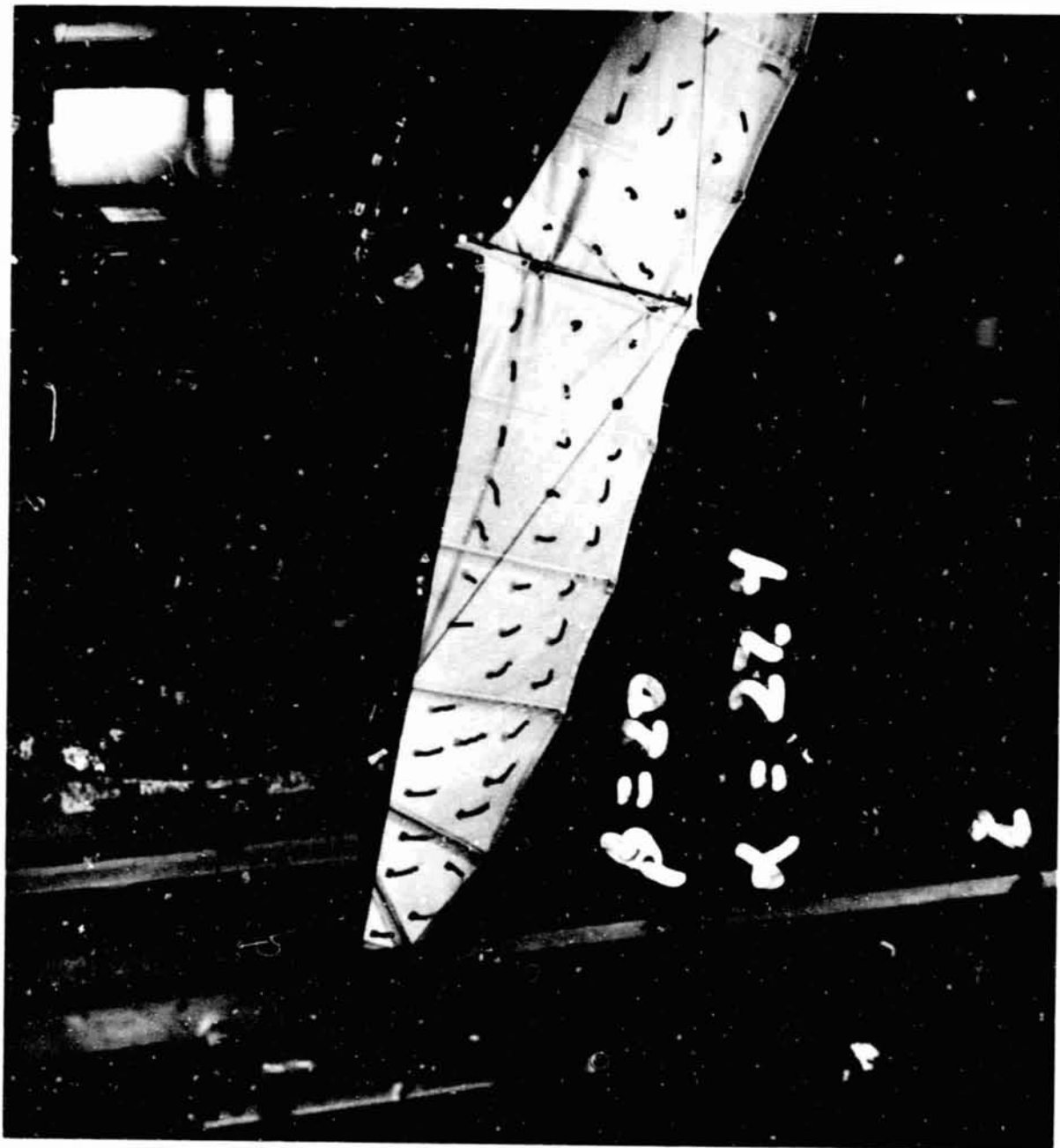
(a) Leading (left) wing half; $\alpha = 27.4°$, $\beta = 20°$.

Figure 17.- Tuft pattern, configuration 31.

52

(b) Trailing (right) wing half; $\alpha = 22.4°$, $\beta = -20°$.

Figure 17.- Concluded.
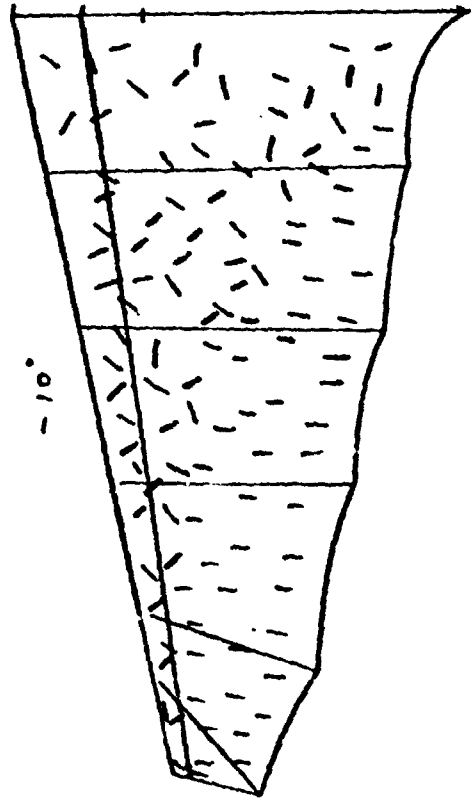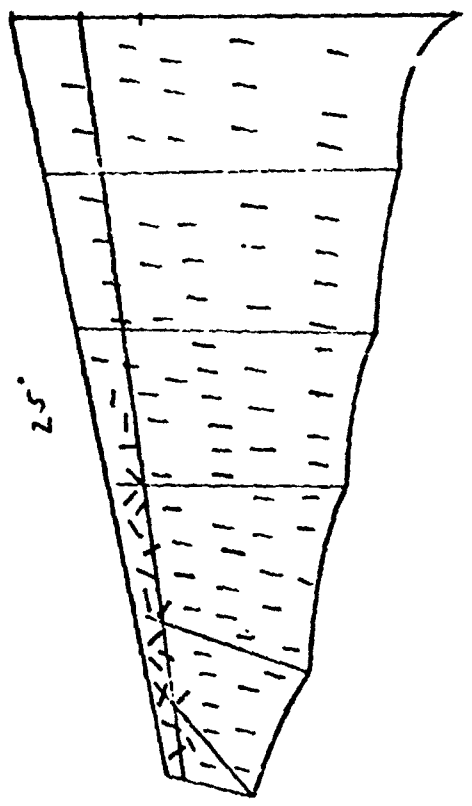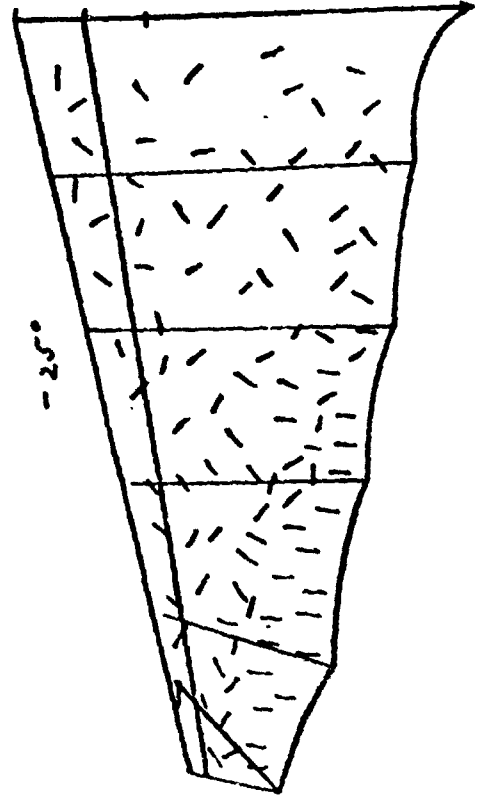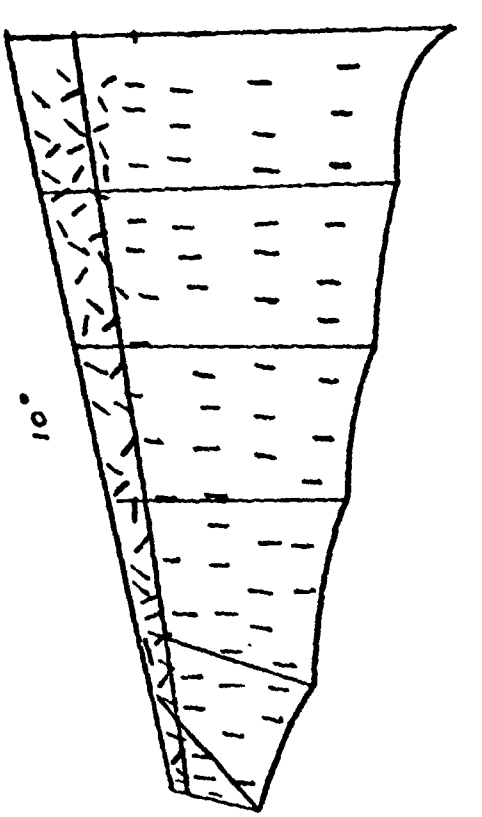
Figure 18.- Model 3 lower-surface tuft pattern.
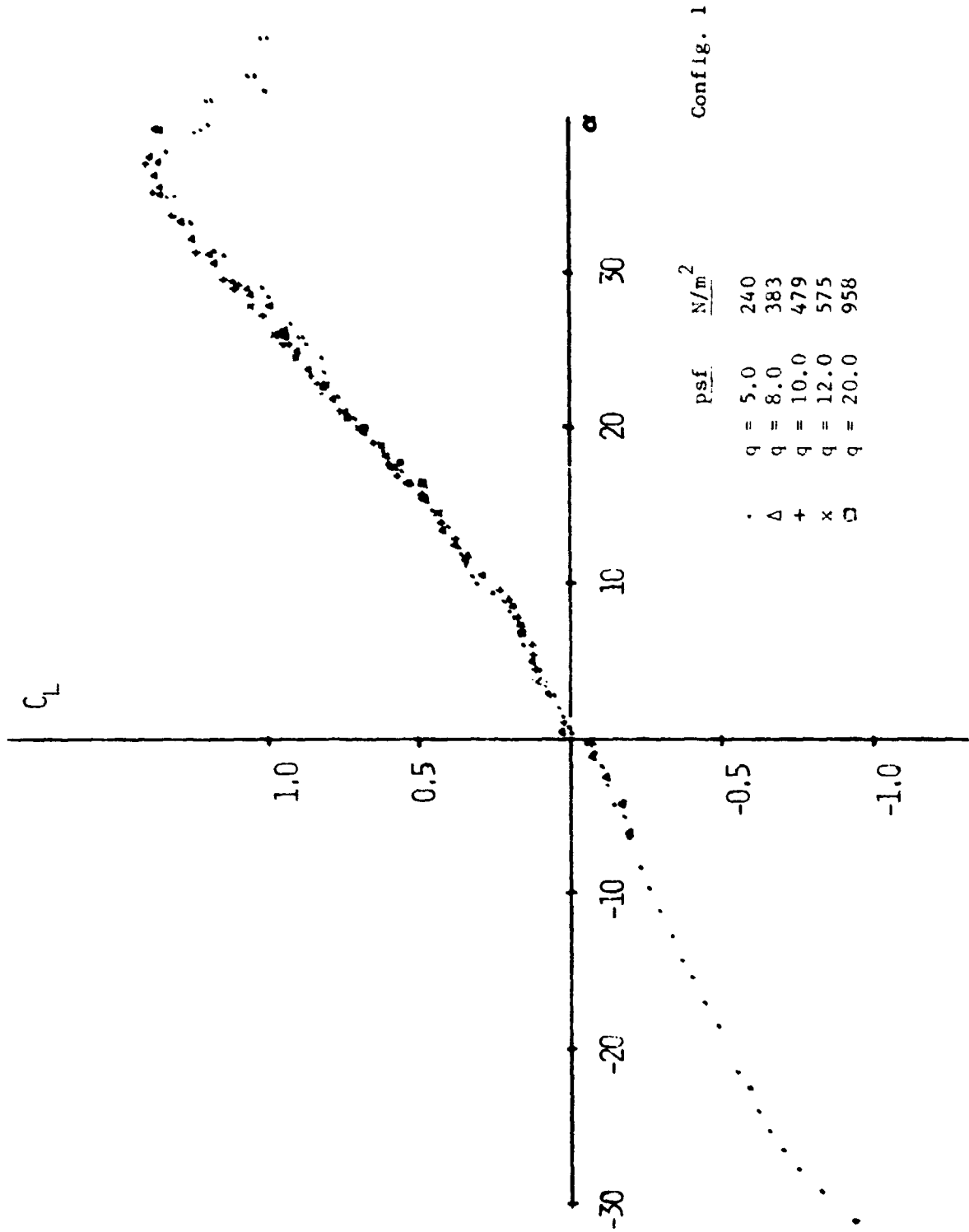
Figure 19.- Effect of dynamic pressure on C_L vs α, configuration 1.
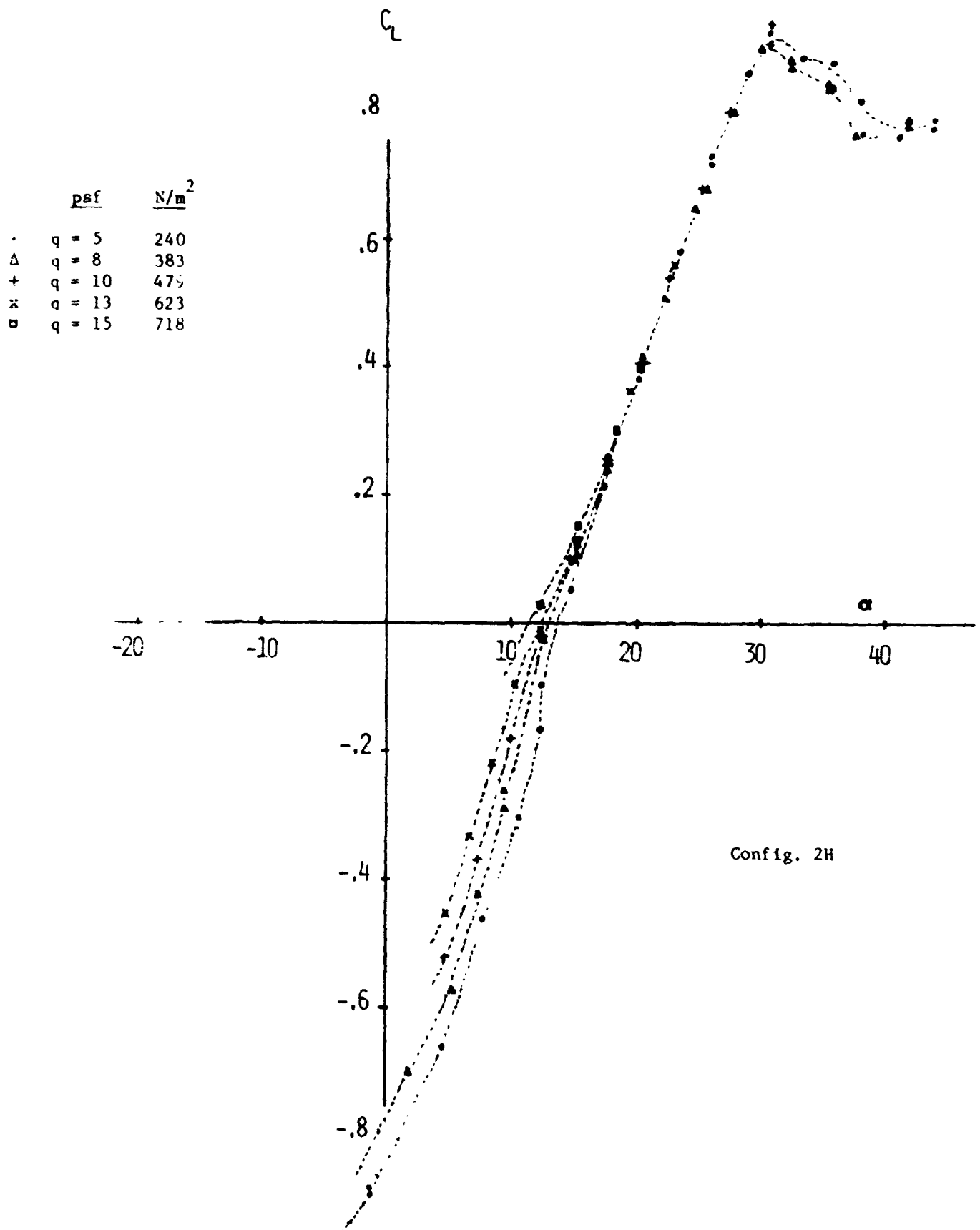
Figure 20.- Effect of dynamic pressure on C_L vs α, configuration 2H.
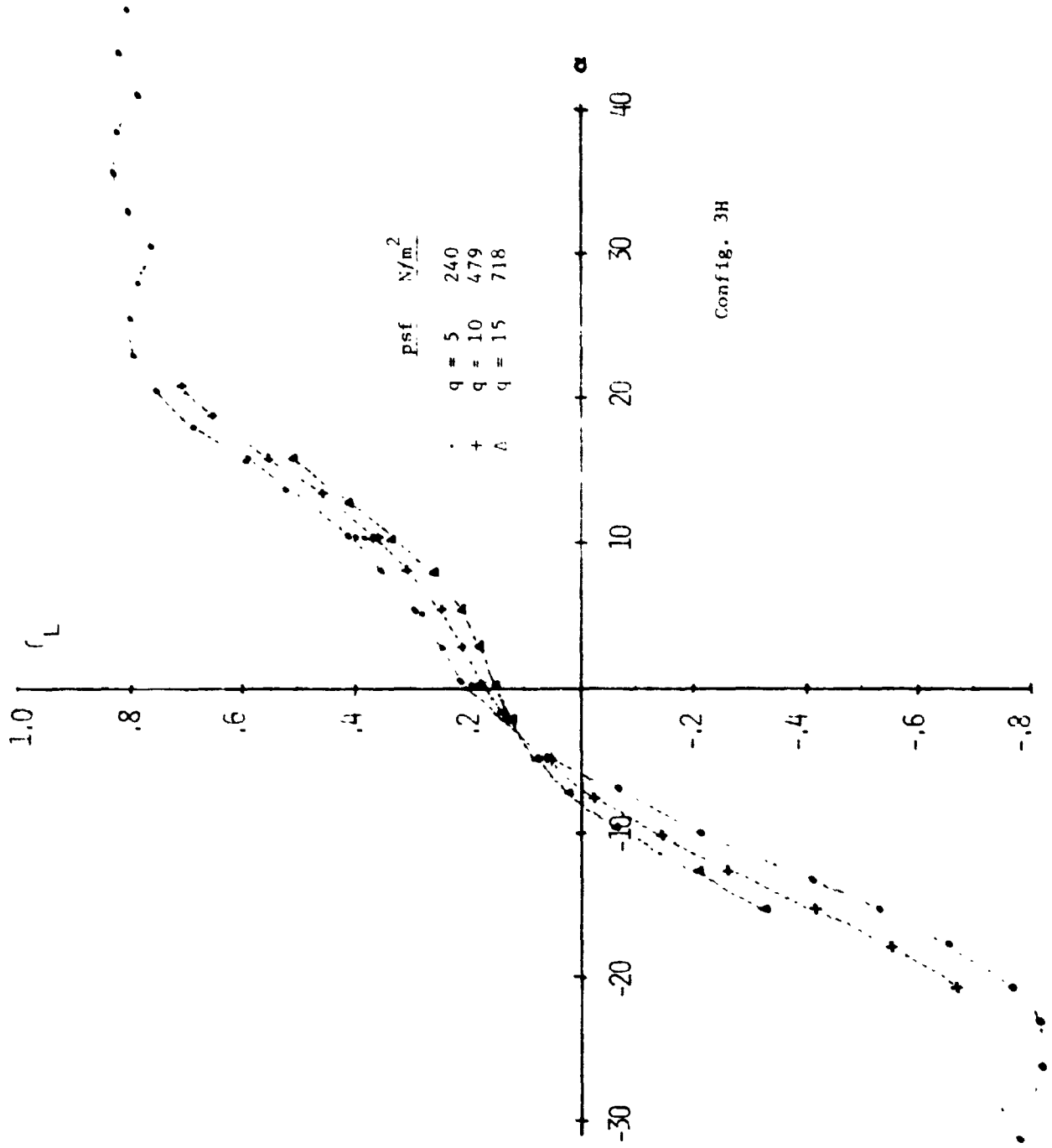
Figure 21.— Effect of dynamic pressure on C_L vs α, configuration 3H.

Figure 22.- Effect of q on drag, configuration 1.
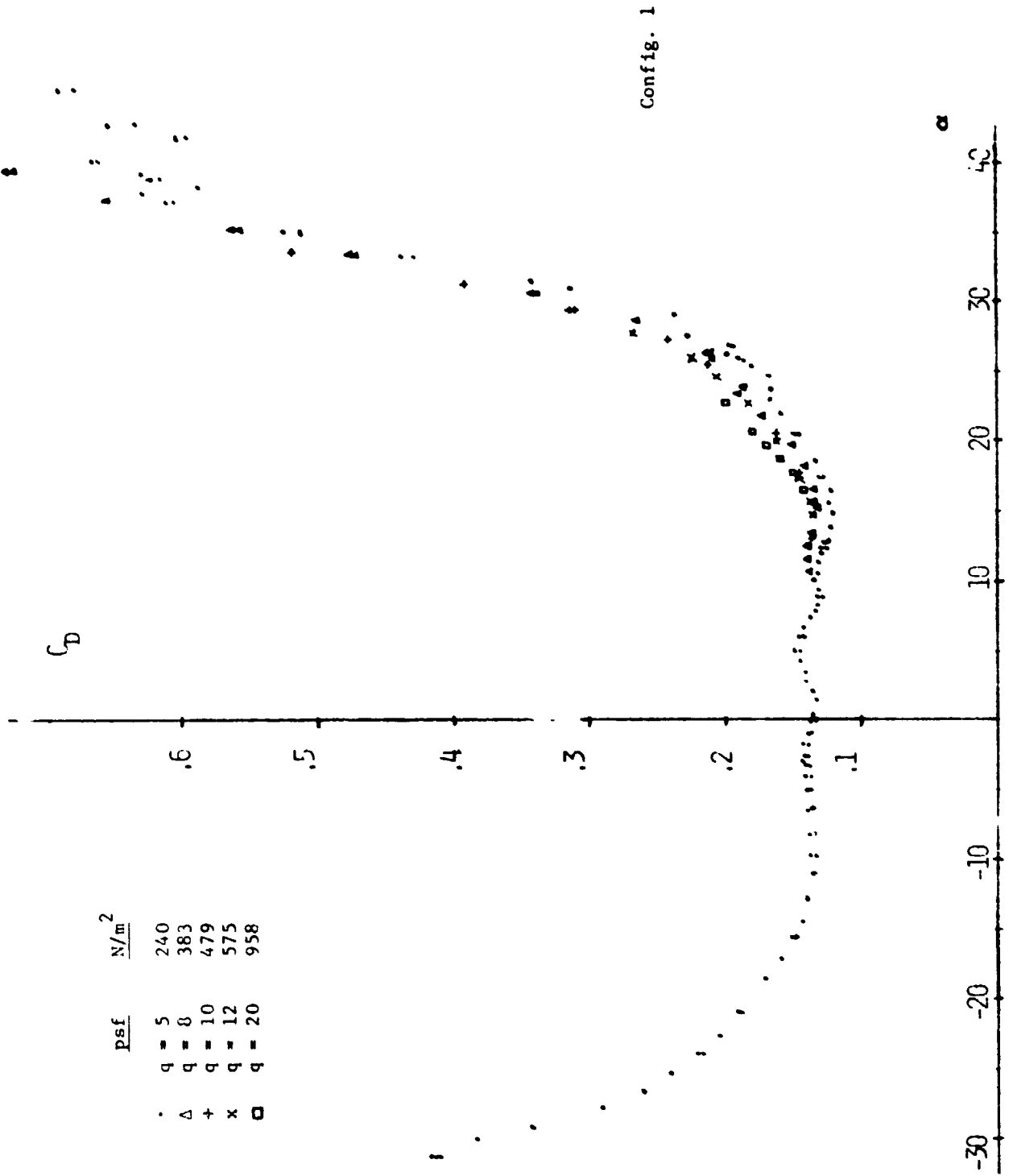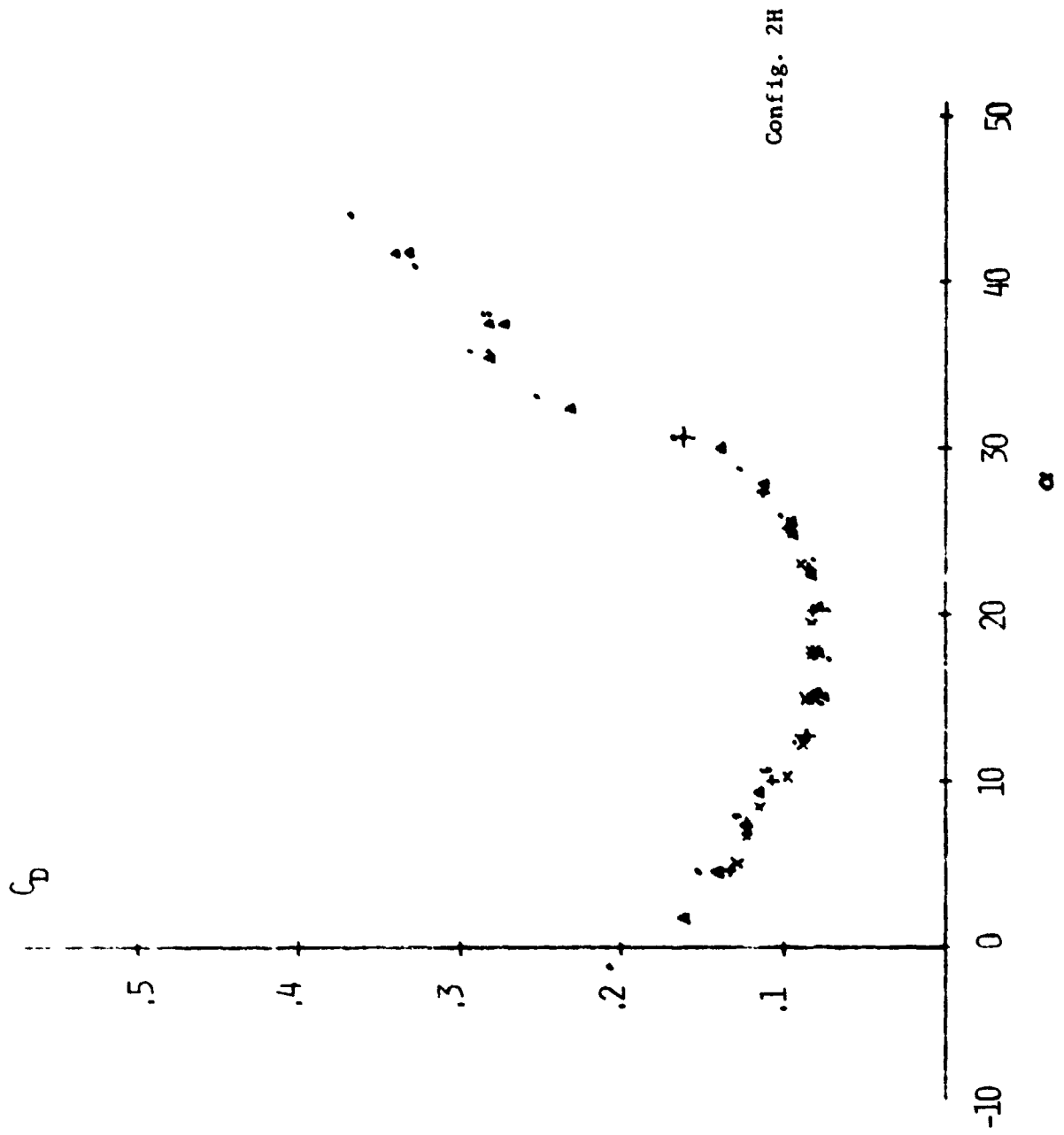
Figure 23.- Effect of q on drag, configuration 2H.

Config. 2H

psf	N/m²
q = 5	240
q = 8	383
q = 10	479

· + △
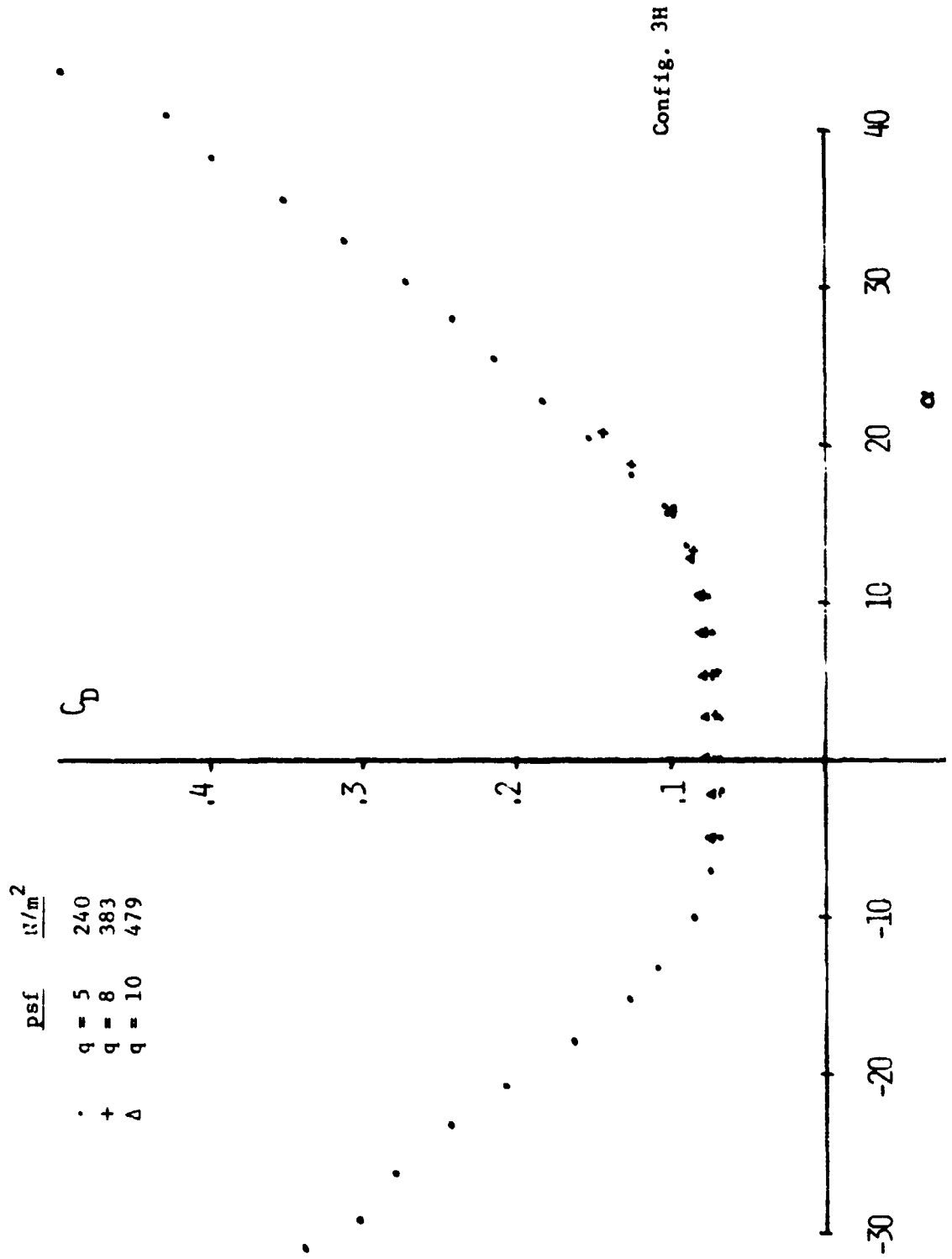
Figure 24.– Effect of q on drag, configuration 3H.
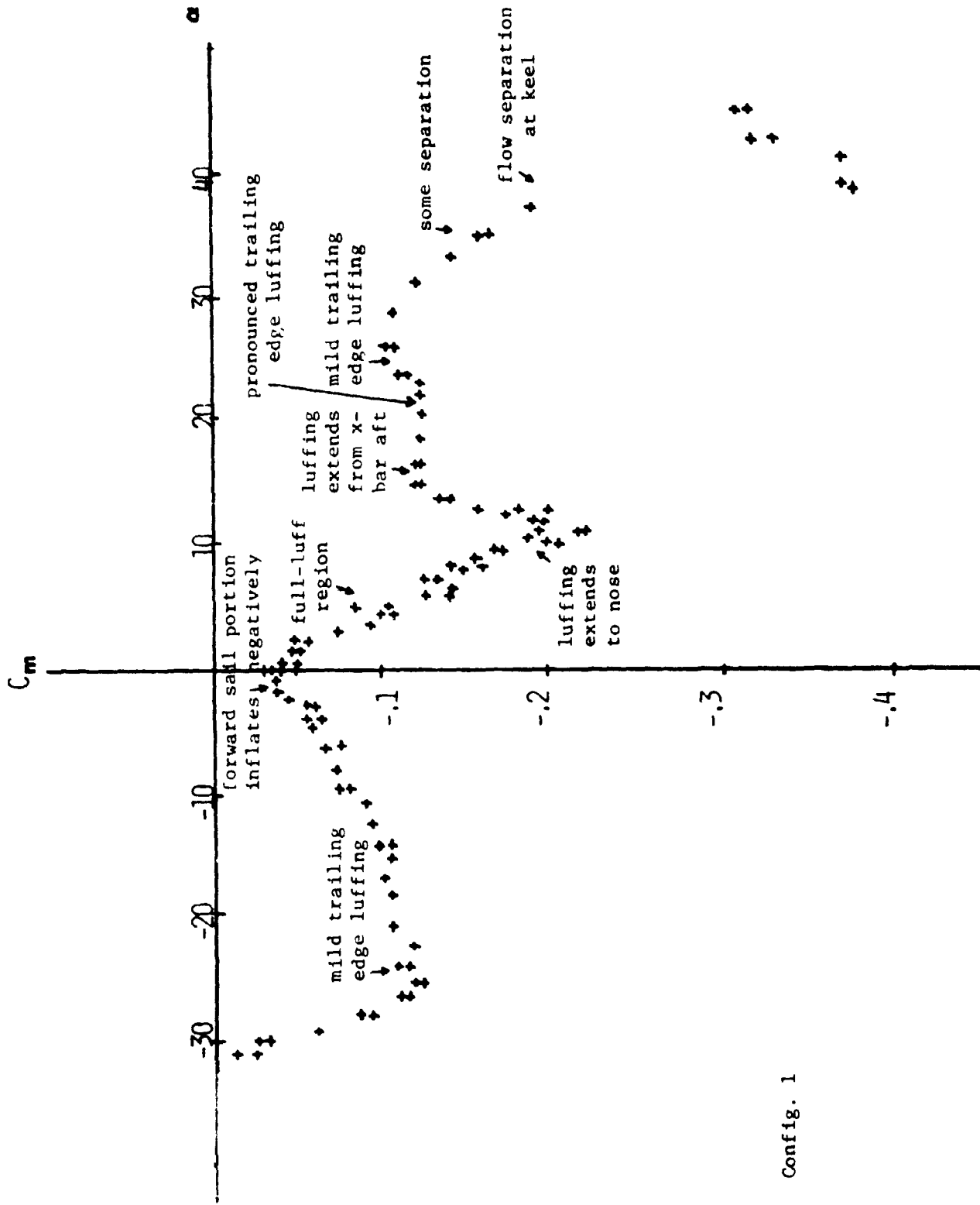
Figure 25.- Features of C_m vs α; q = 240 N/m² (5 psf).
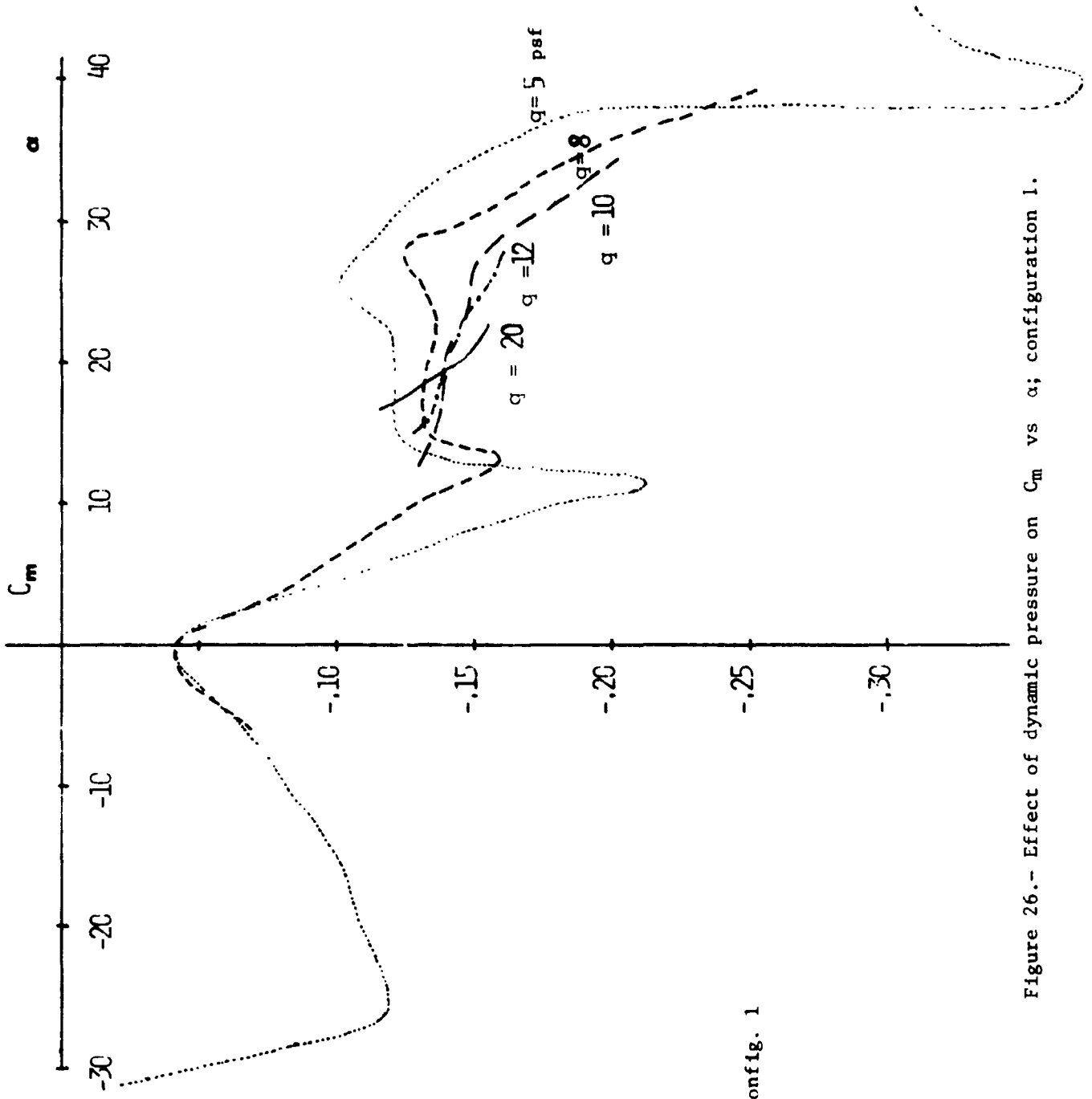
Config. 1

61

Figure 26.— Effect of dynamic pressure on C_m vs α; configuration 1.
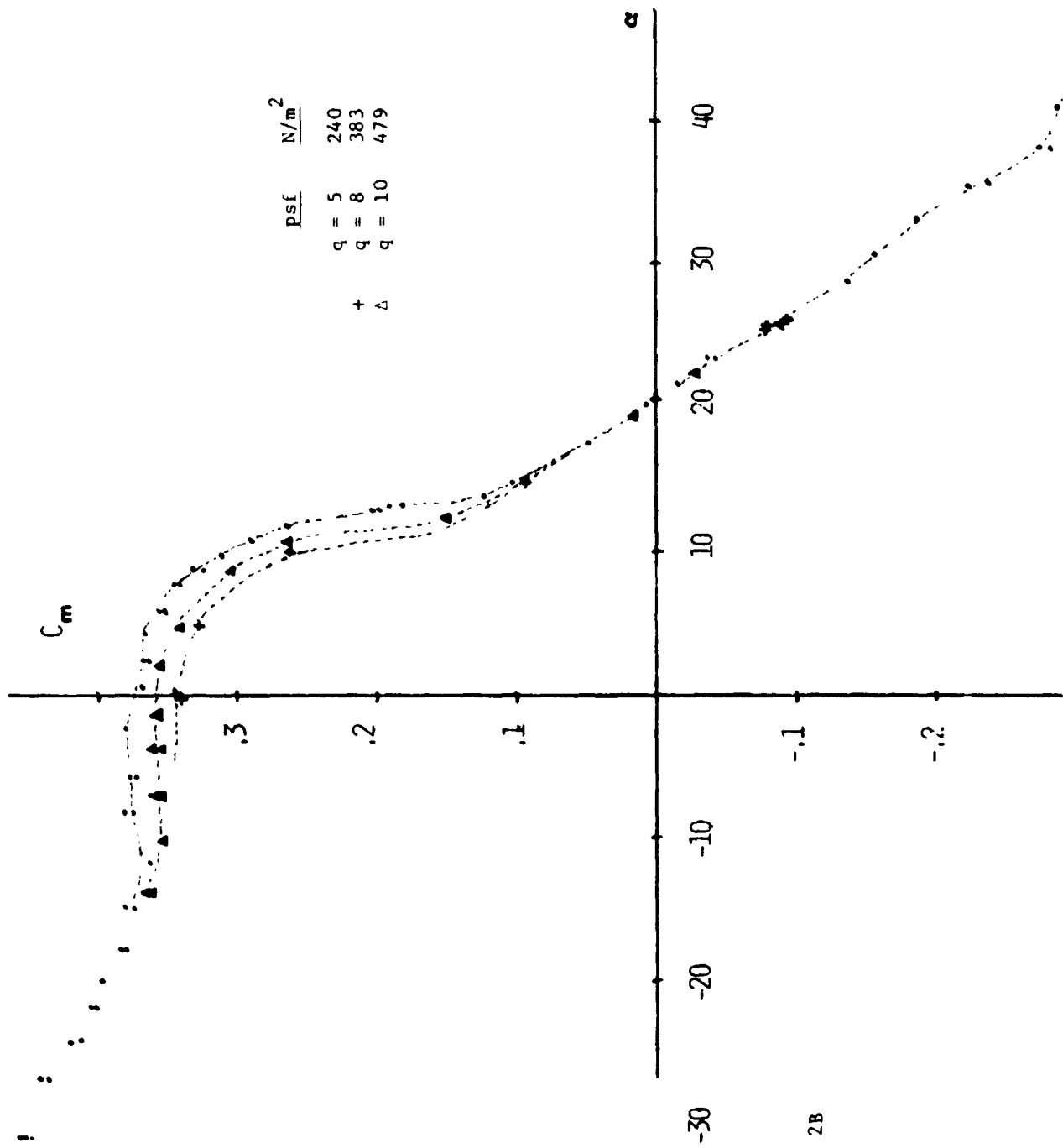
Config. 1

Figure 27.— Effect of dynamic pressure on C_m vs α; configuration 2B.
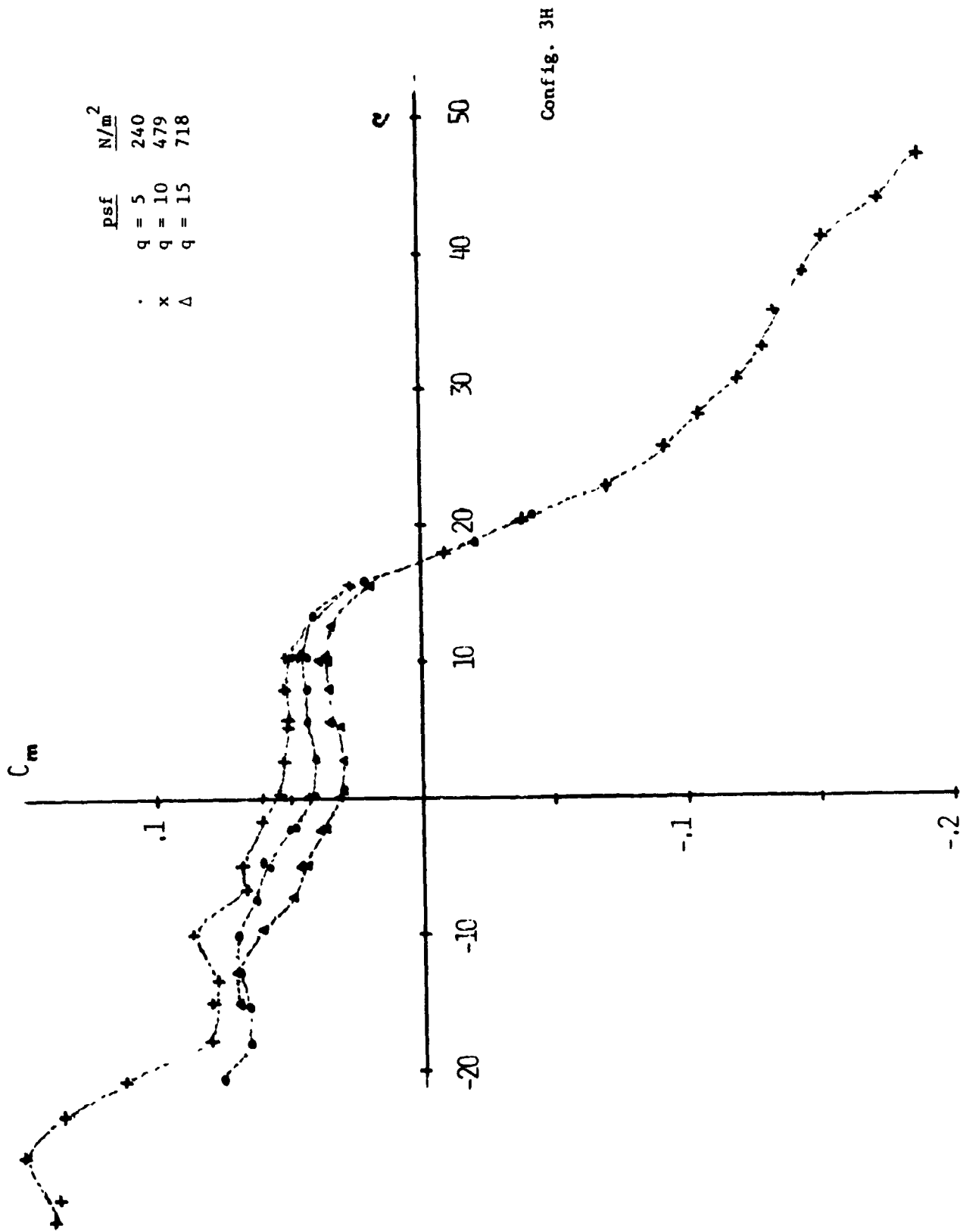
Config. 2B

Figure 28.- Effect of dynamic pressure on C_m vs α; configuration 3H.

64
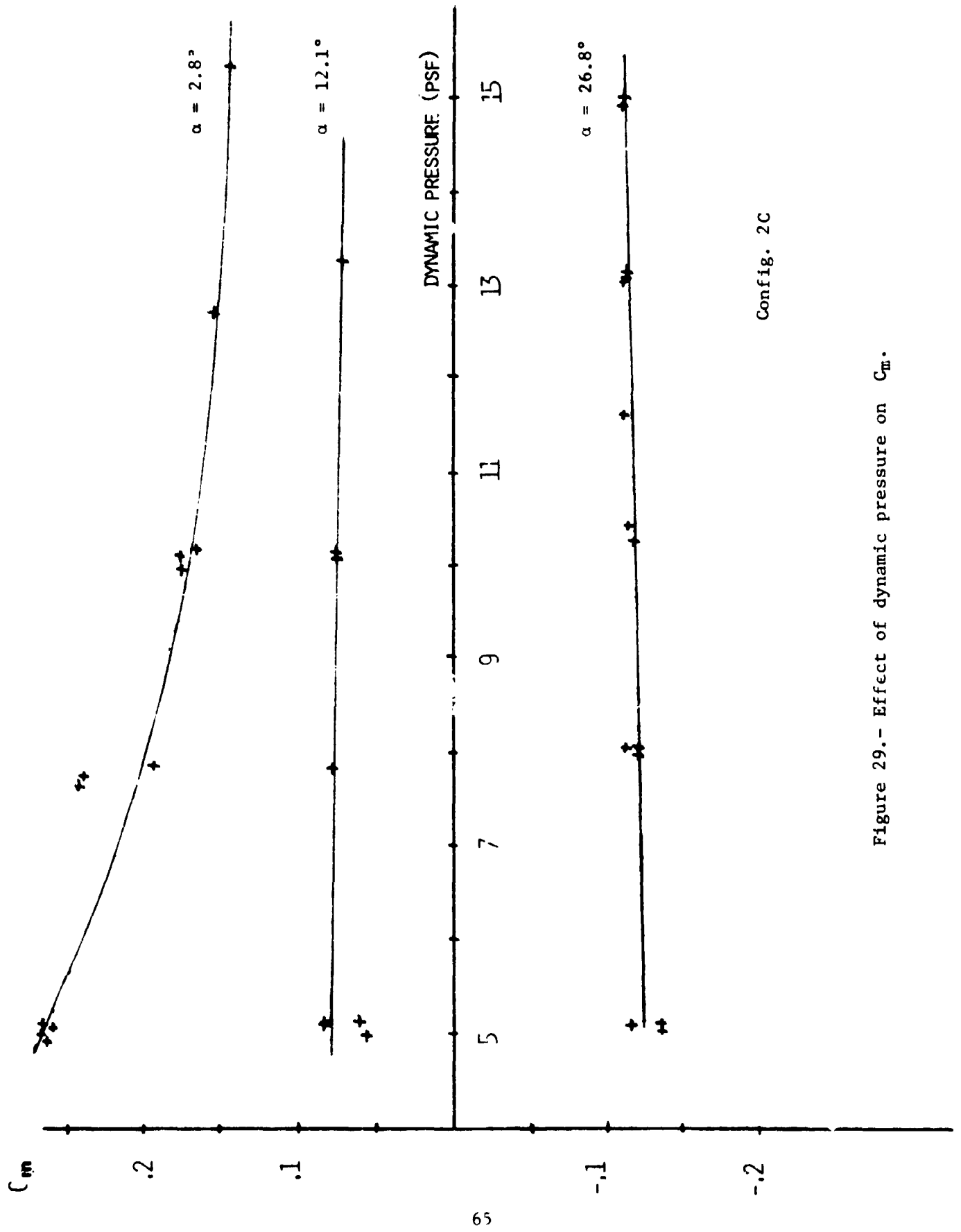
Figure 29.- Effect of dynamic pressure on C_m.
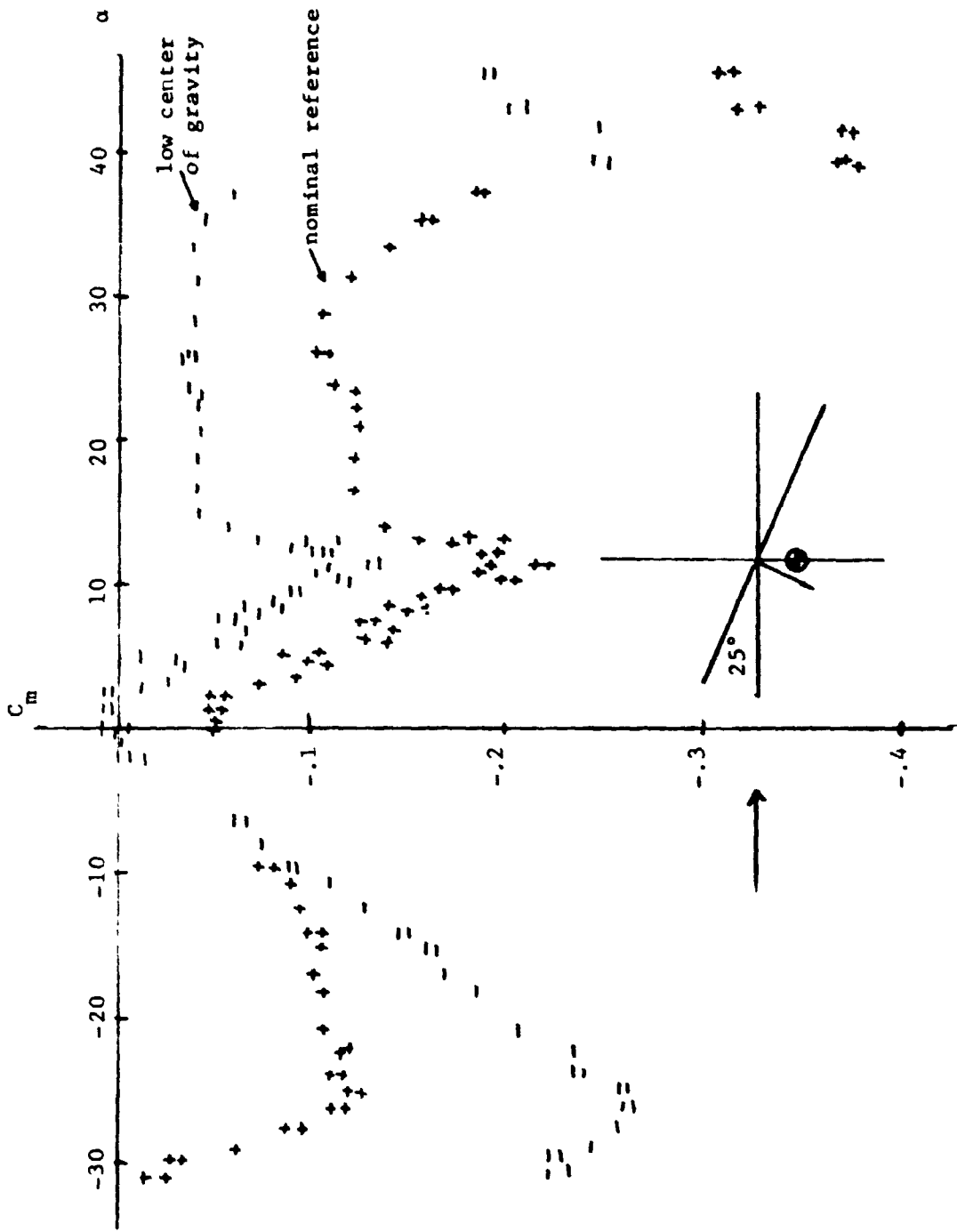
Figure 30.- Effect of center-of-gravity location, model 1.
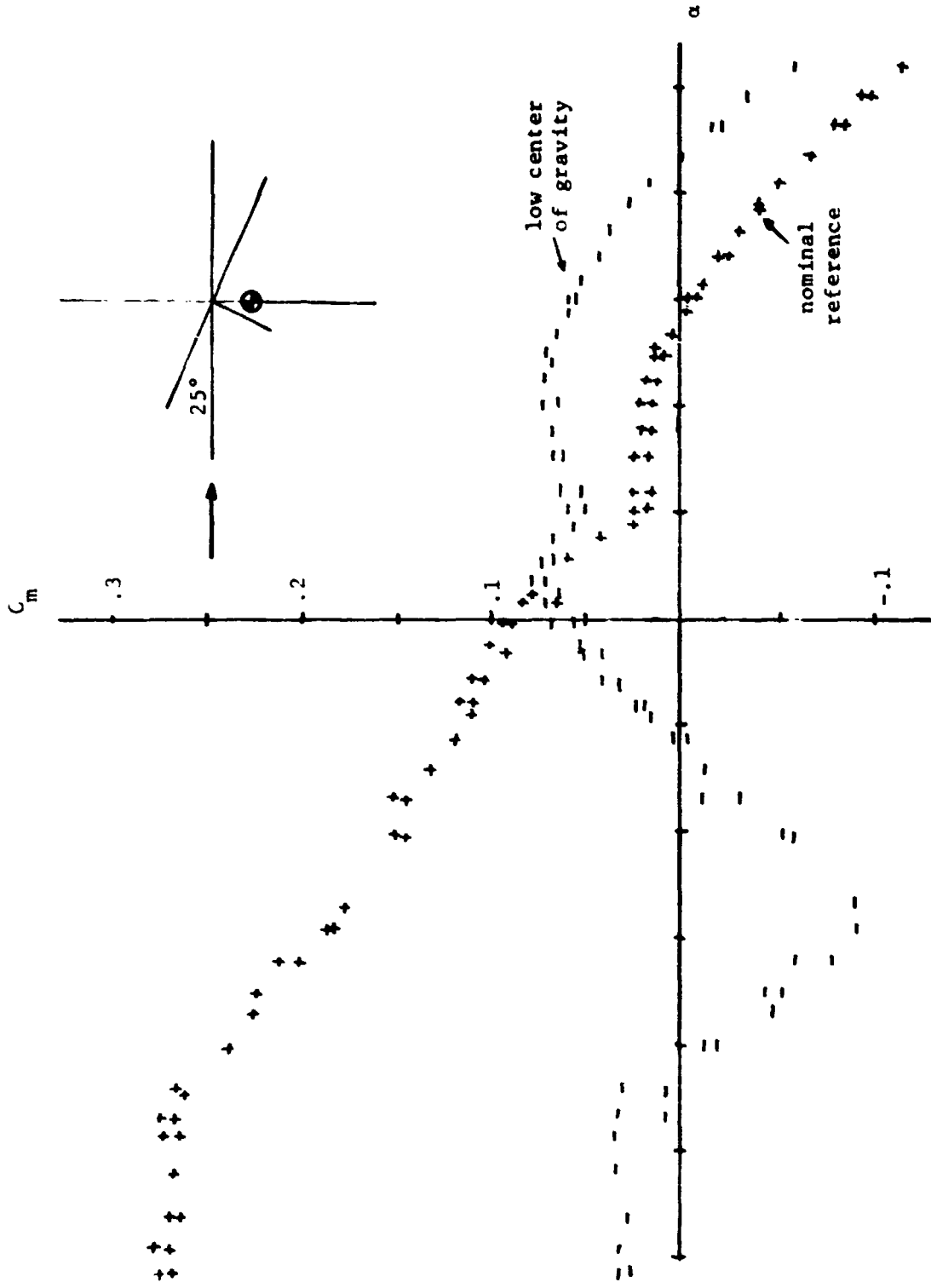
Figure 31.- Effect of center-of-gravity location, model 2E.
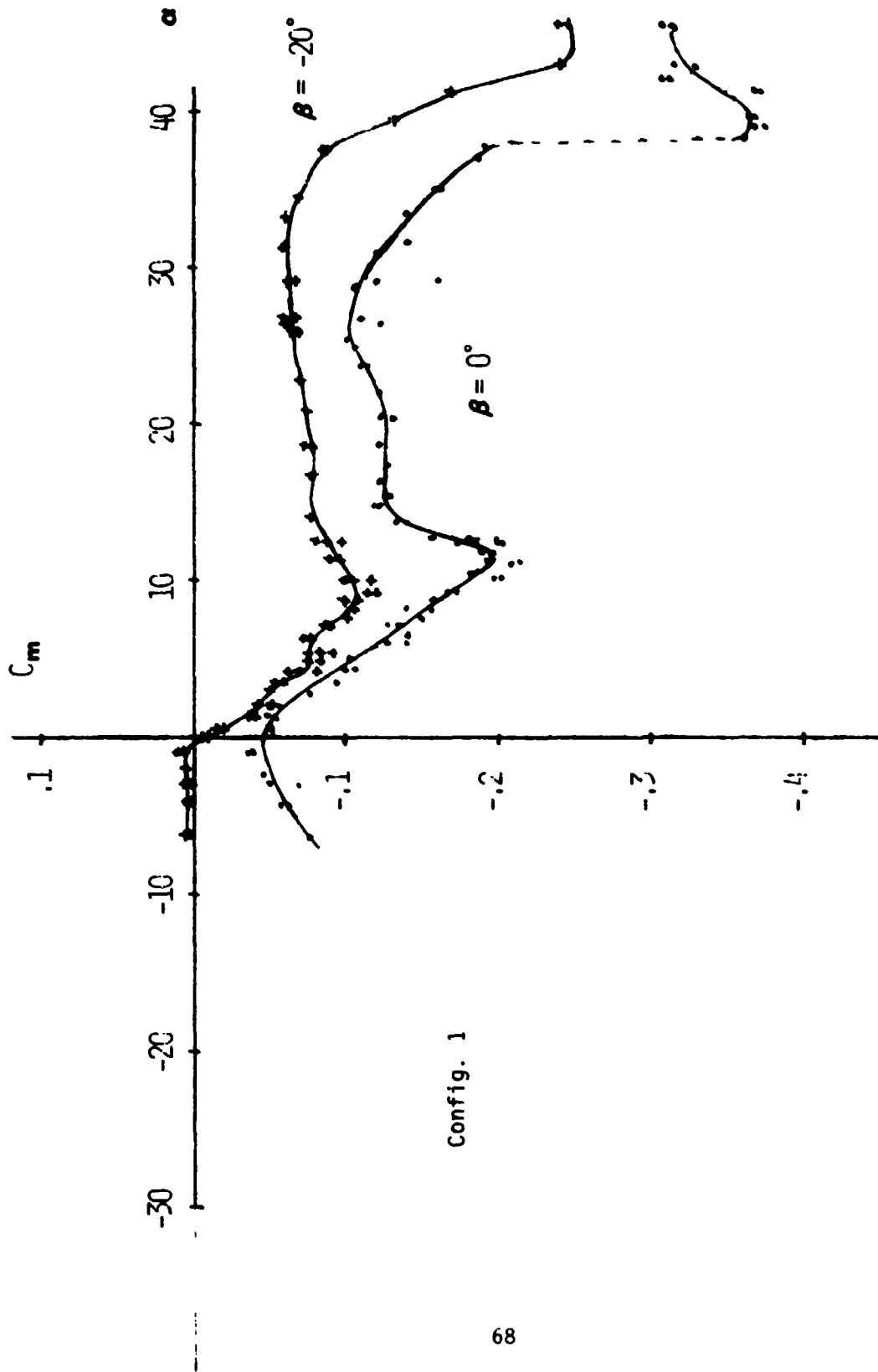
Figure 32.- Effect of sideslip on C_m vs α, configuration 1.
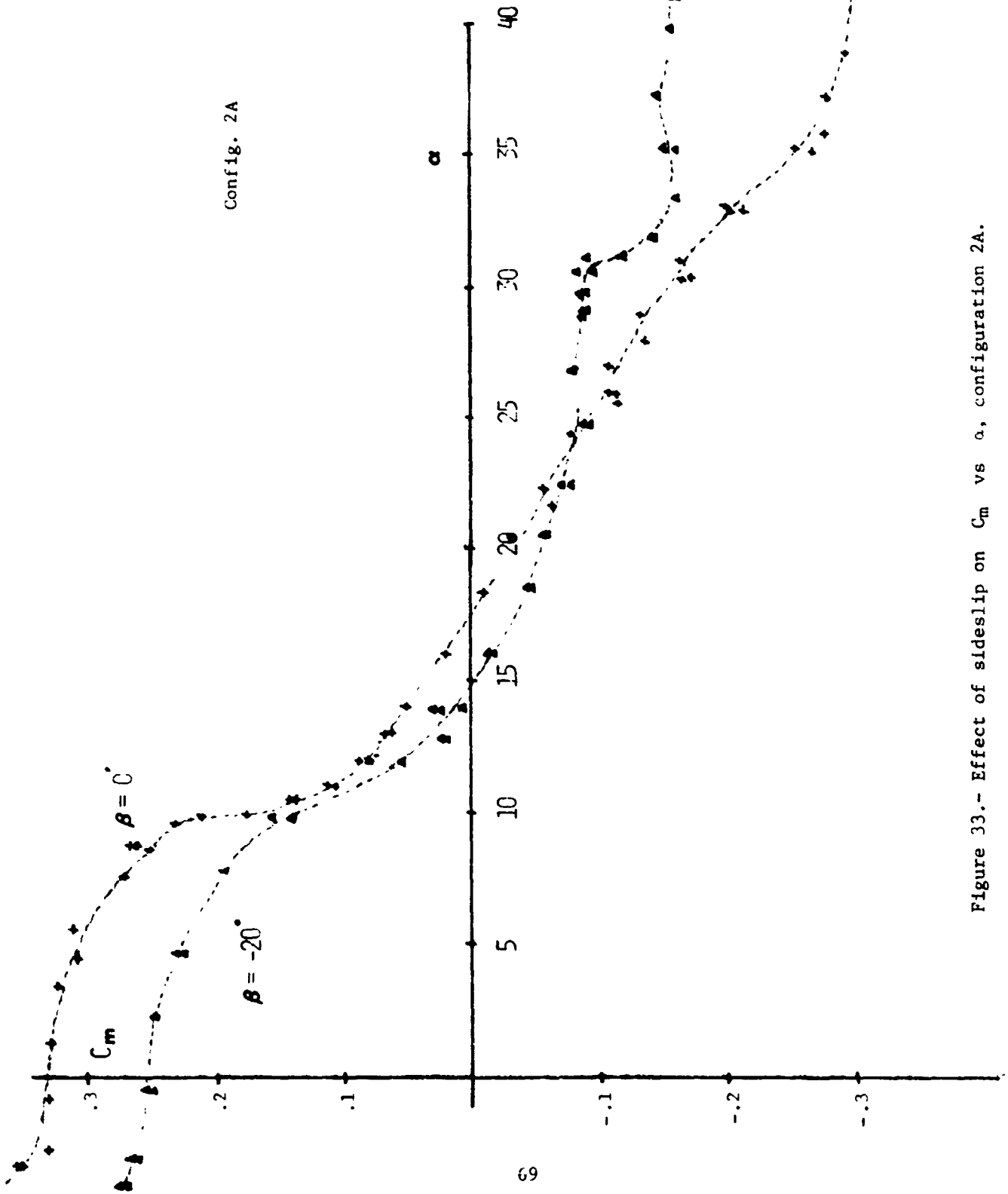
Figure 33.- Effect of sideslip on C_m vs α, configuration 2A.

Figure 34.- Effect of sideslip on C_m vs α, configuration 3H.
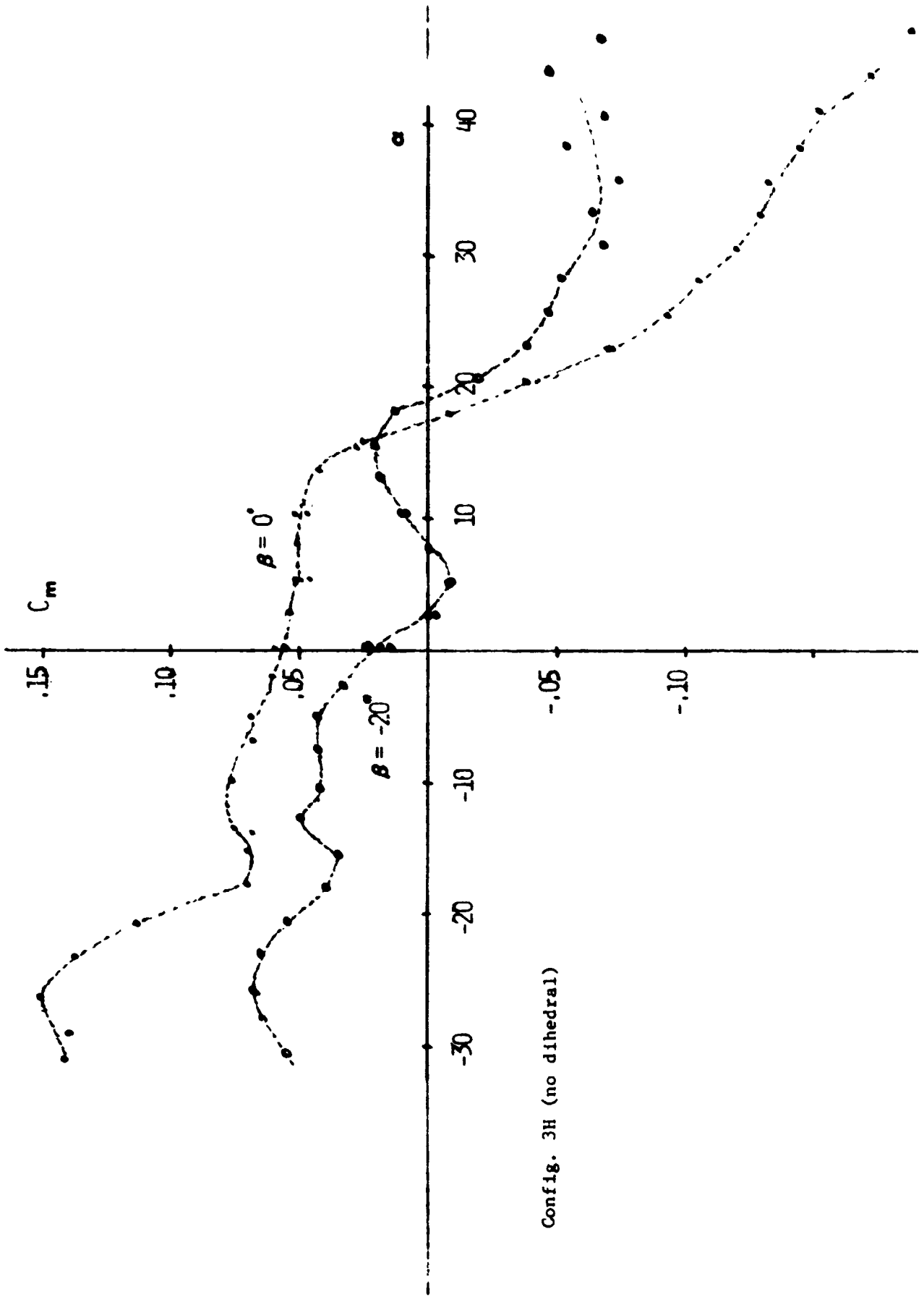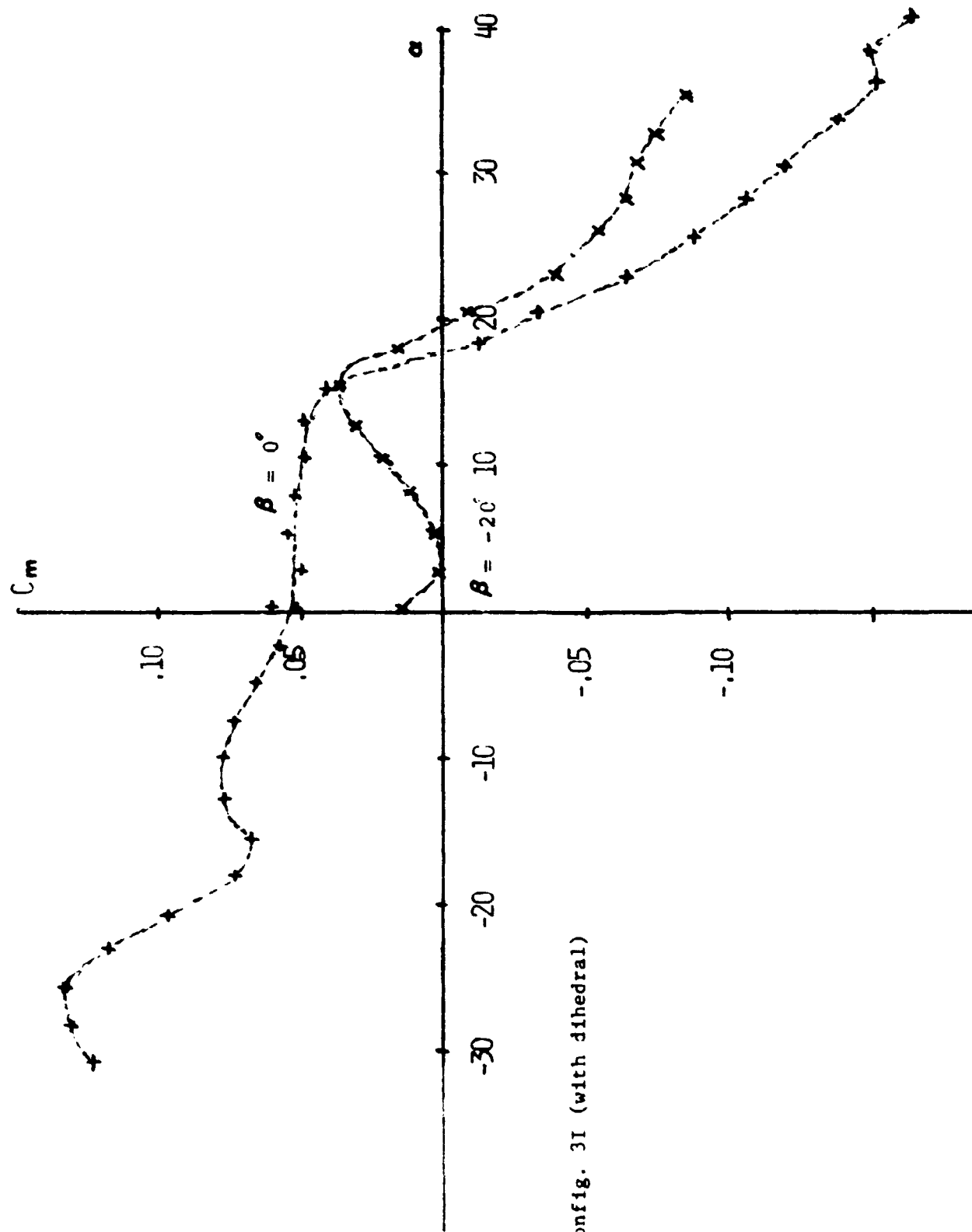
Config. 3H (no dihedral)

Figure 35.- Effect of sideslip on C_m vs α, configuration 3I.

Config. 3I (with dihedral)

71
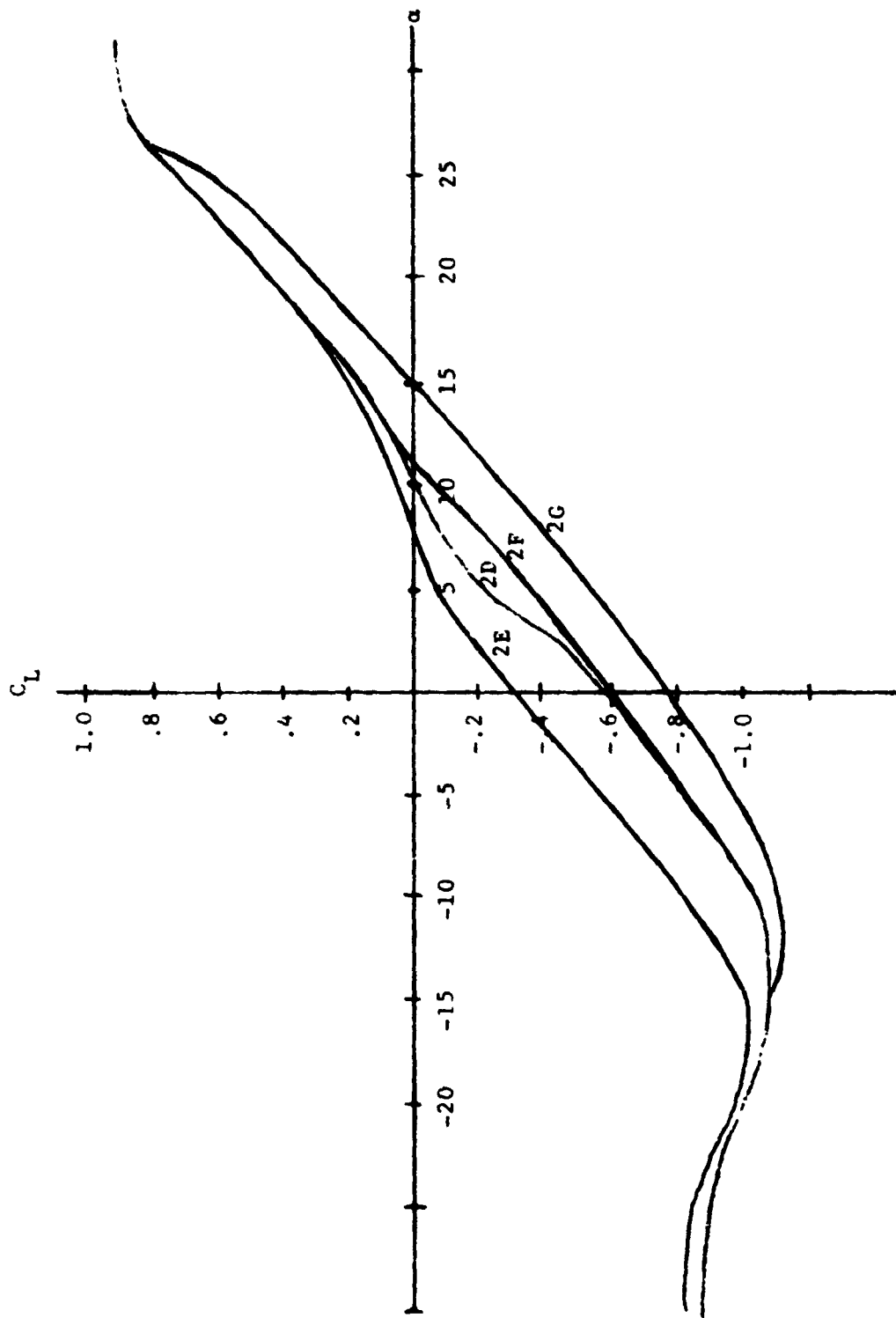
Figure 36.- Effect of luff lines.

(a) C_L vs α

Config. 2L,M,N,O,P

Figure 37.

73
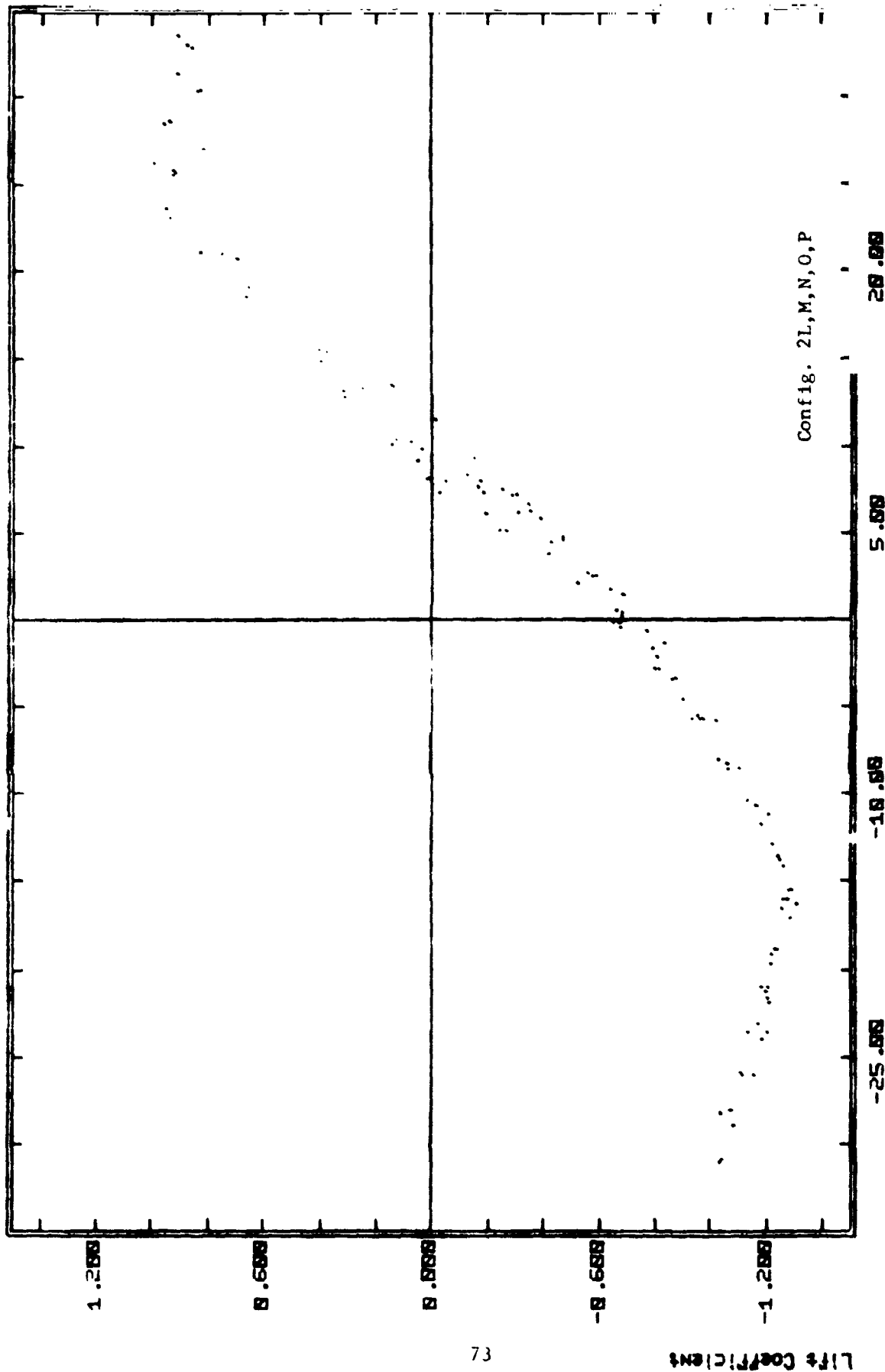
CL vs. alpha BATTEN FLEXIBILITY

+ Config. 2I
- Config. 2J
o Config. 2B
x Config. 2K

ANGLE OF ATTACK (deg.)

LIFT COEFFICIENT
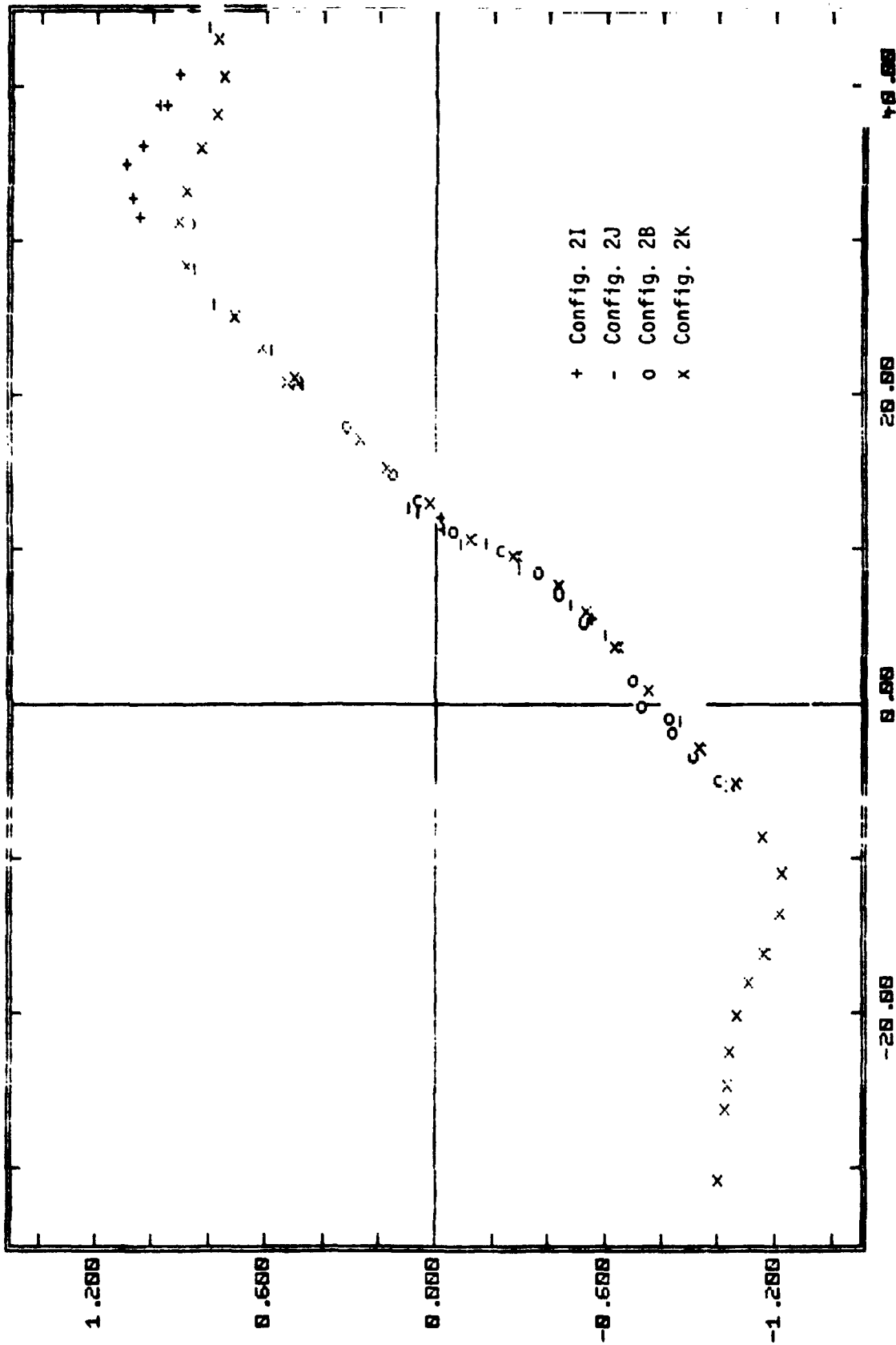
(b) Effect of batten flexibility.

Figure 37.- Concluded.

74
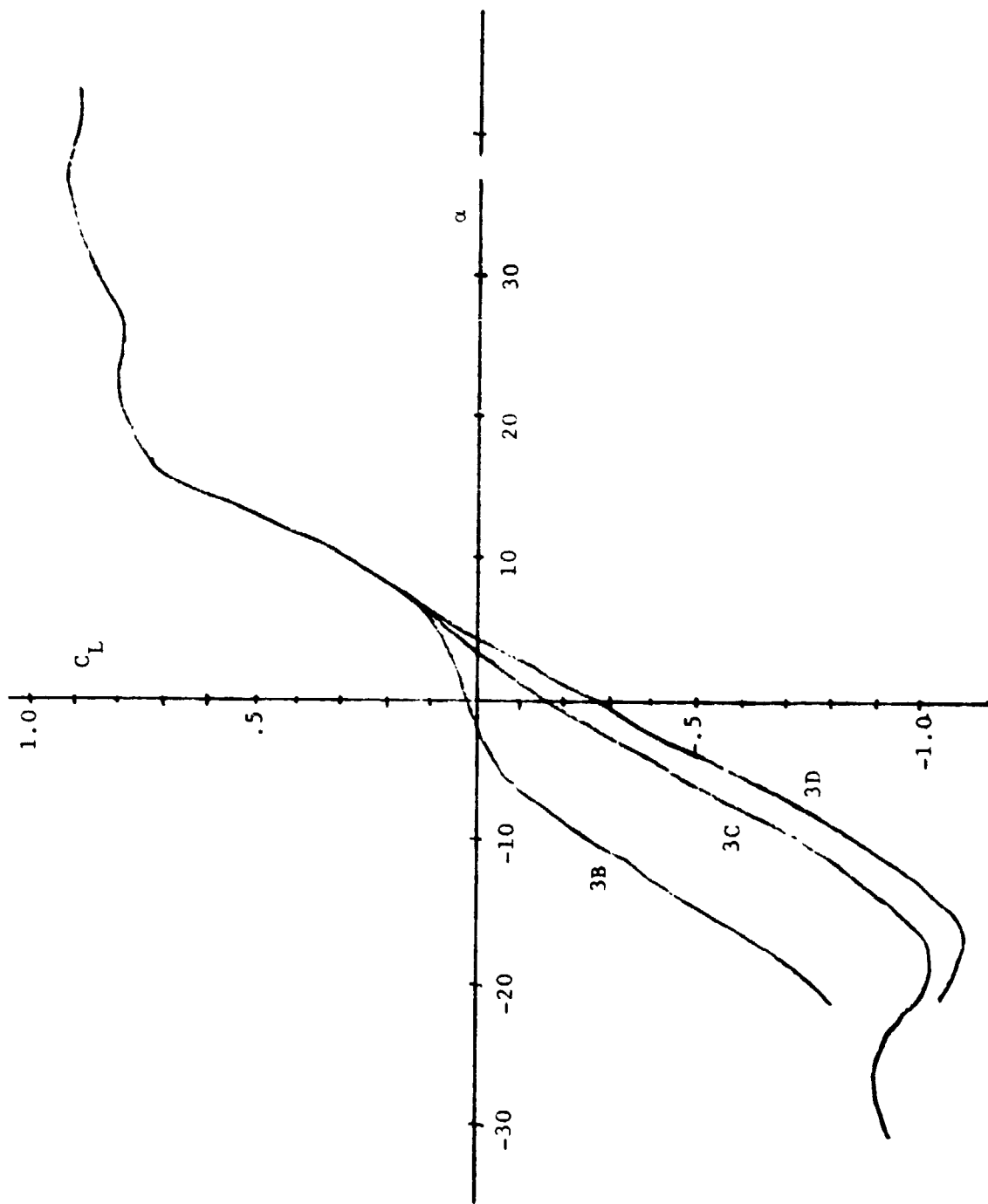
Figure 38.- Effect of luff lines.
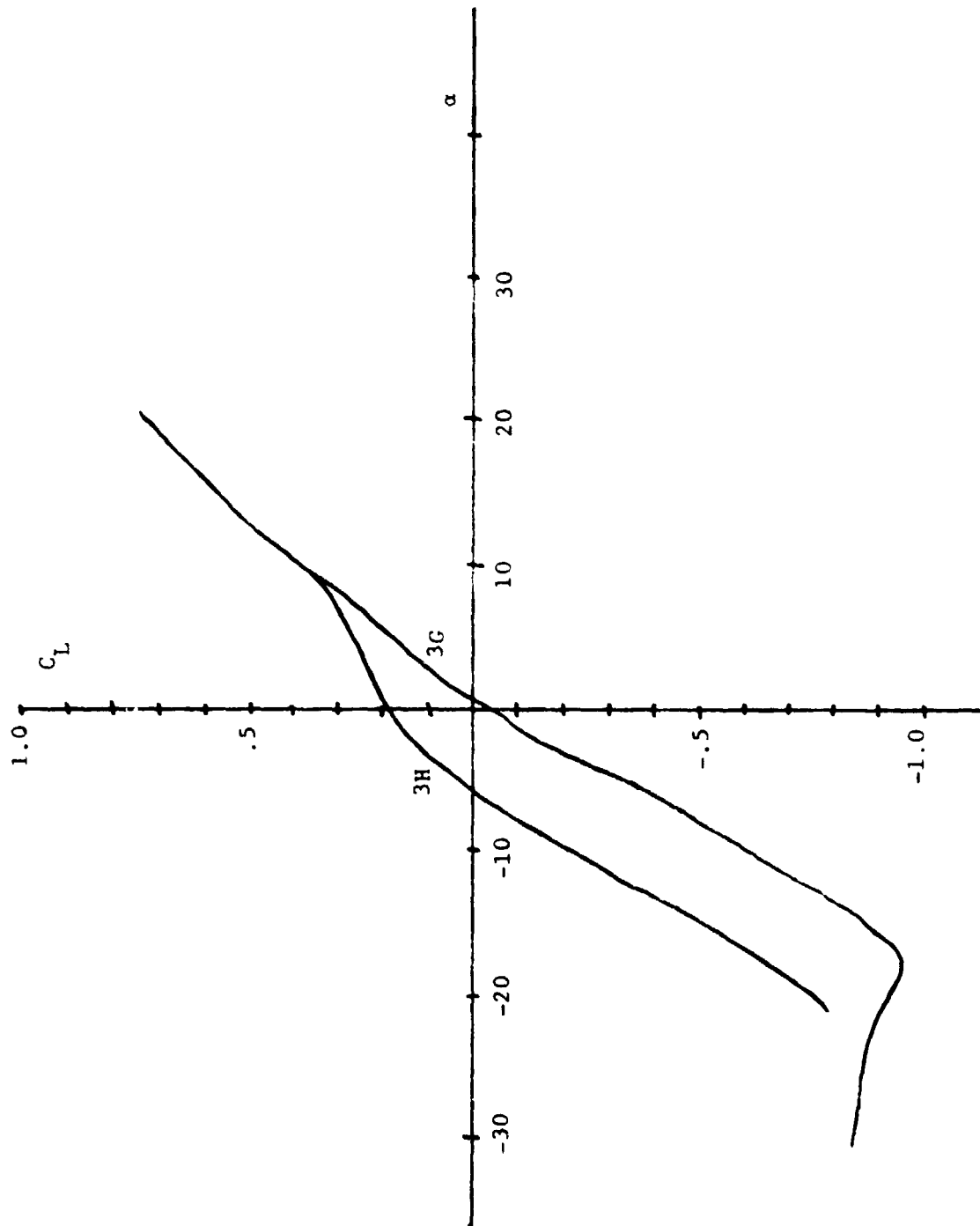
Figure 39.- Effect of luff lines.
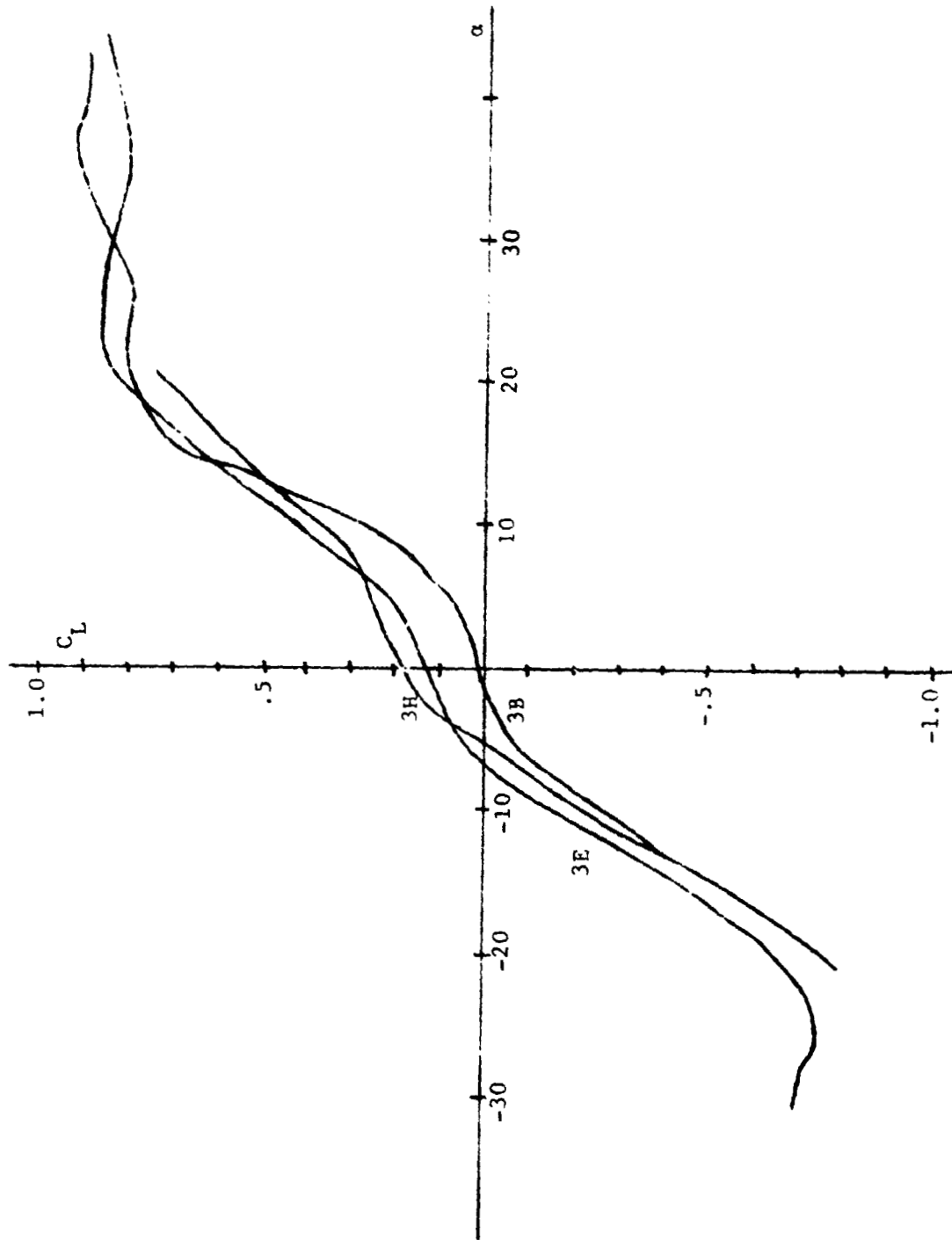
Figure 40.- Effect of batten camber.
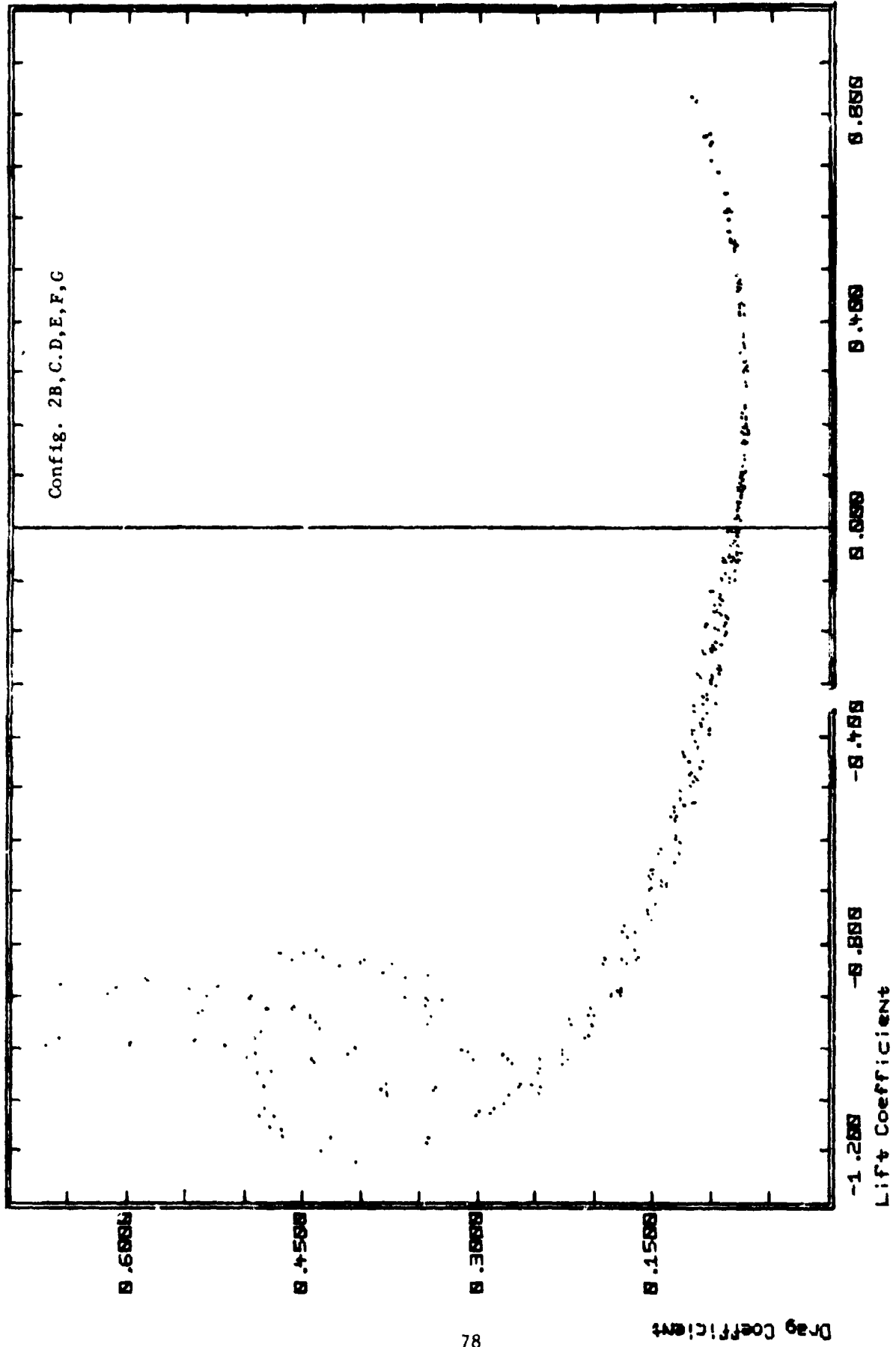
Figure 41.- Combined drag data, configurations 2B,C,D,E,F,G.

Config. 2B,C.D,E,F,G

Lift Coefficient

Drag Coefficient

0.6000

0.4500

0.3000

0.1500

-1.200

-0.800

-0.400

0.000

0.400

0.800

78
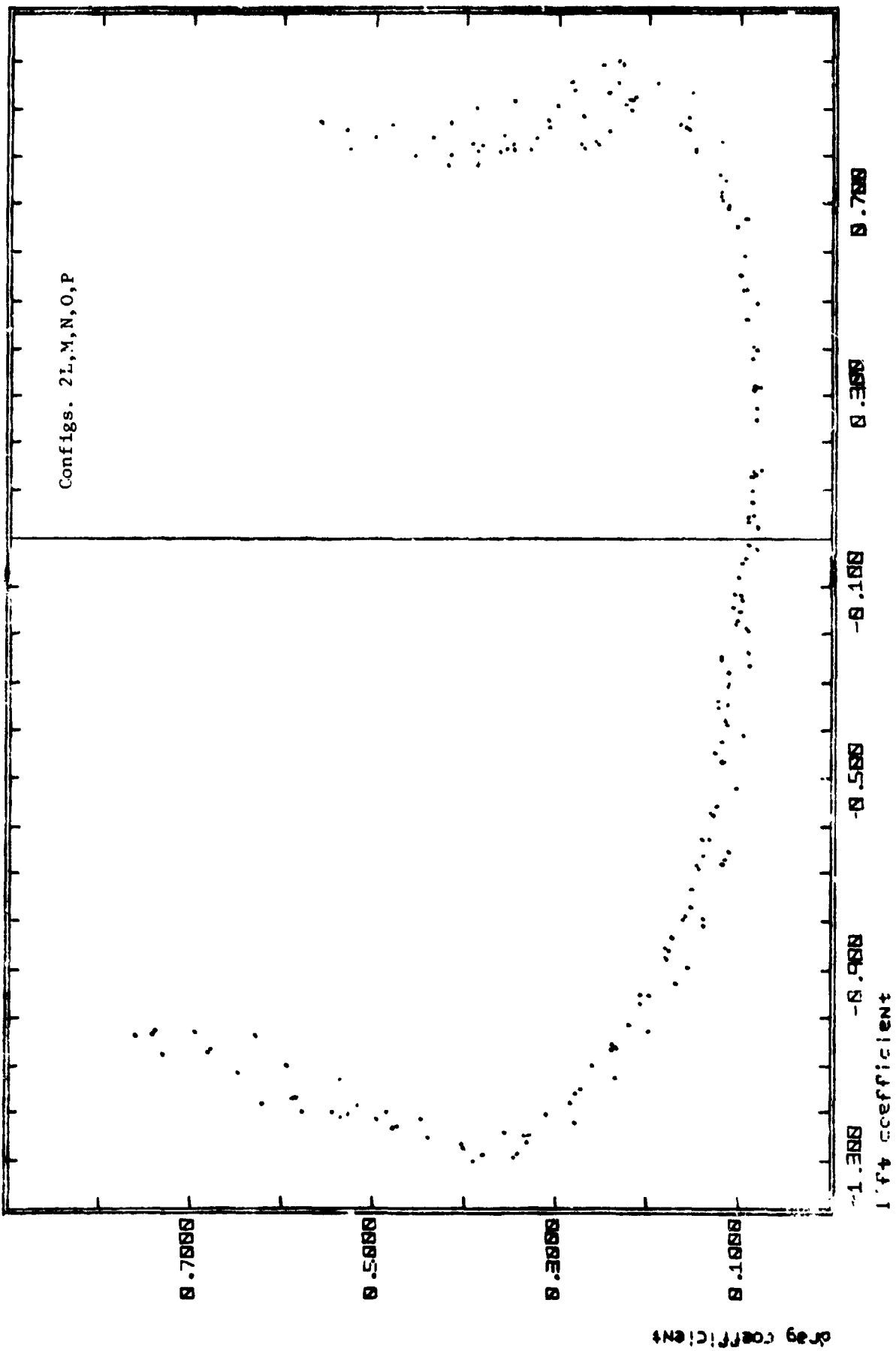
Figure 42.— Combined drag data, configurations 2L,M,N,O,P

Configs. 2L,M,N,O,P

lift coefficient

drag coefficient
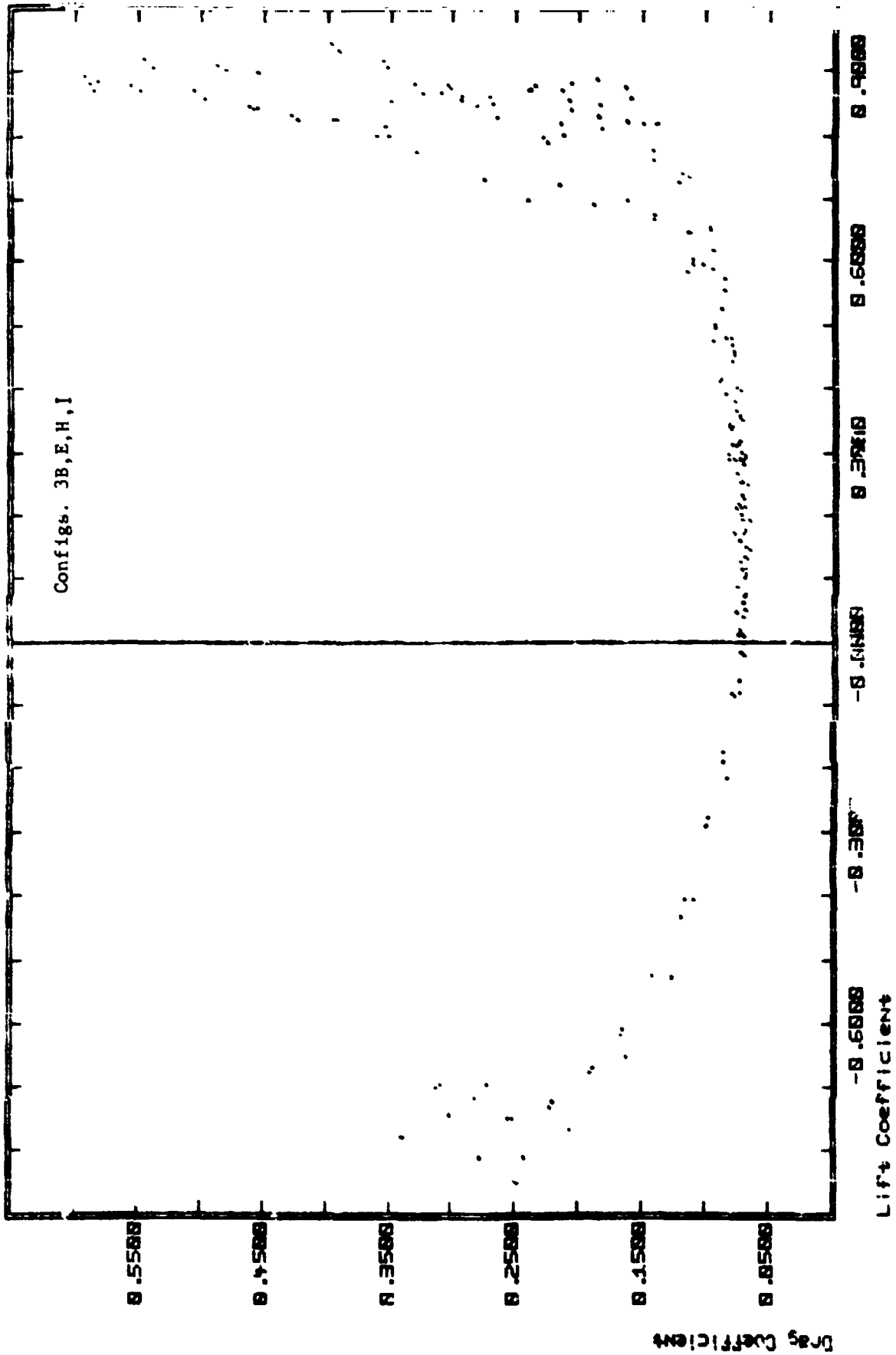
Figure 43.- Combined drag data, configurations 3B,E,H,I.

MODEL 2

+ – Configuration 2B
x – Configuration 2L
o – Configuration 2P

Figure 44.– C_D vs C_L^2

Figure 45.- Example of fitted drag data; configuration 1.
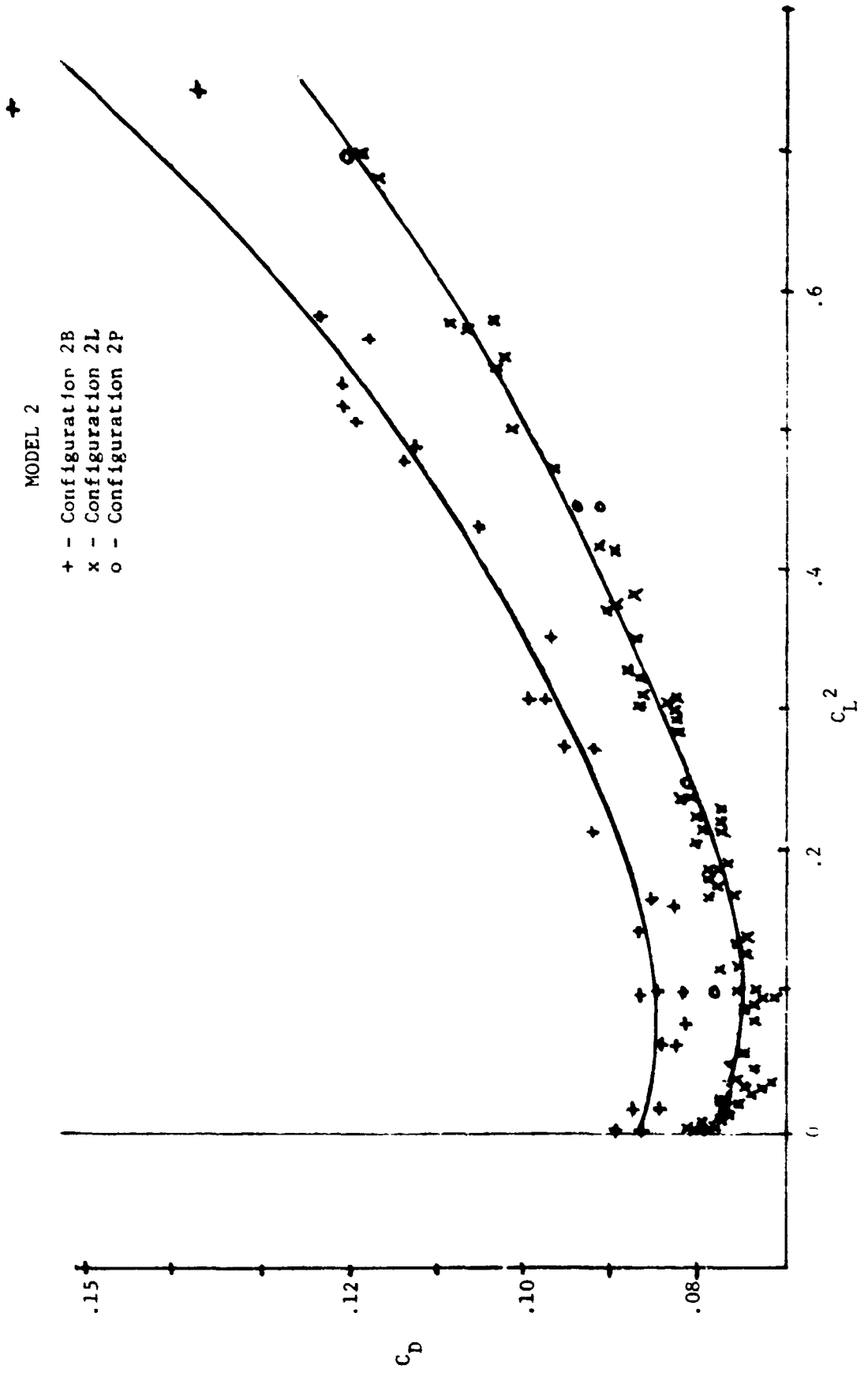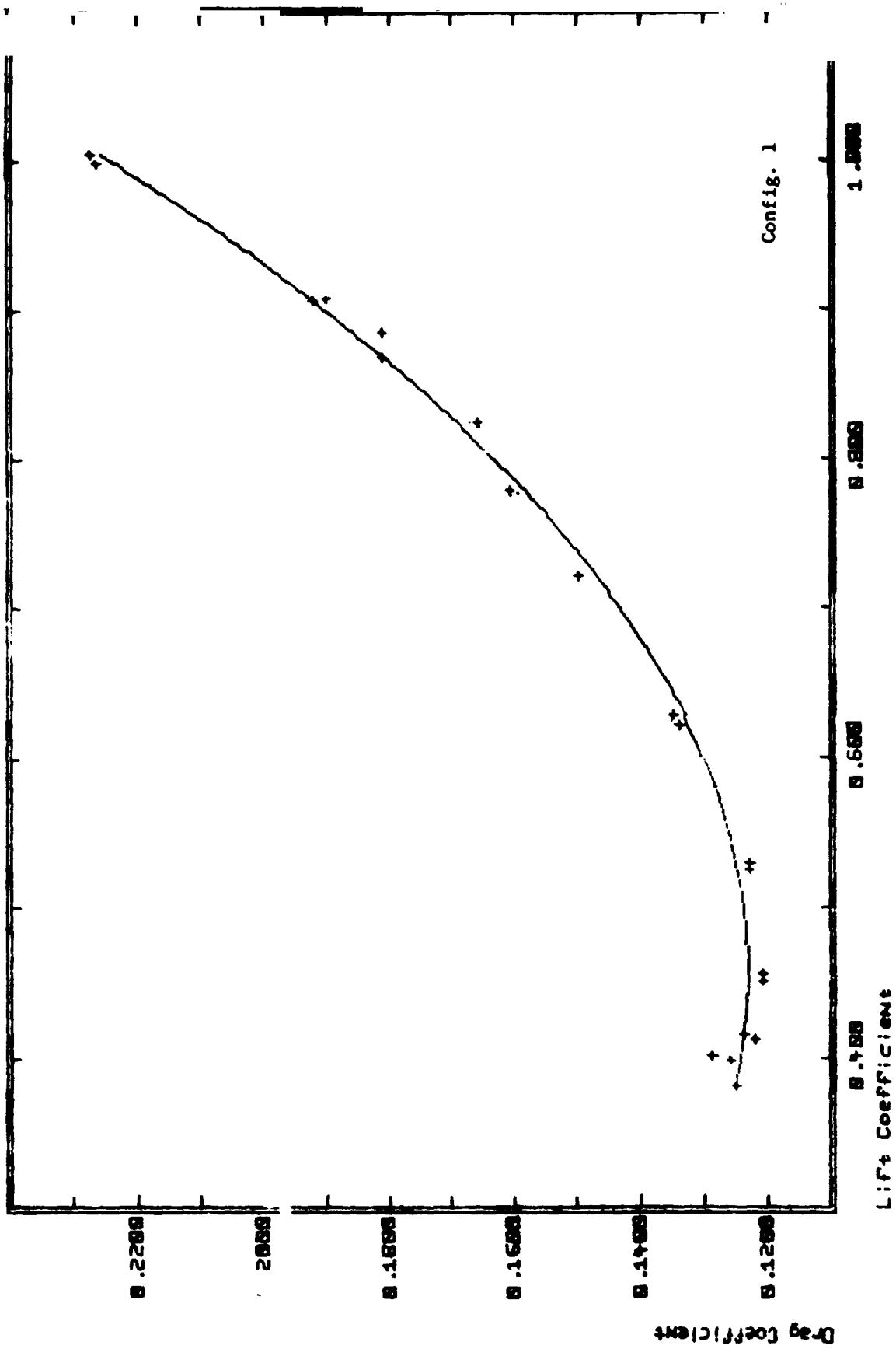
$$C_D \approx .122 + .321\ (C_L - .44)^2$$
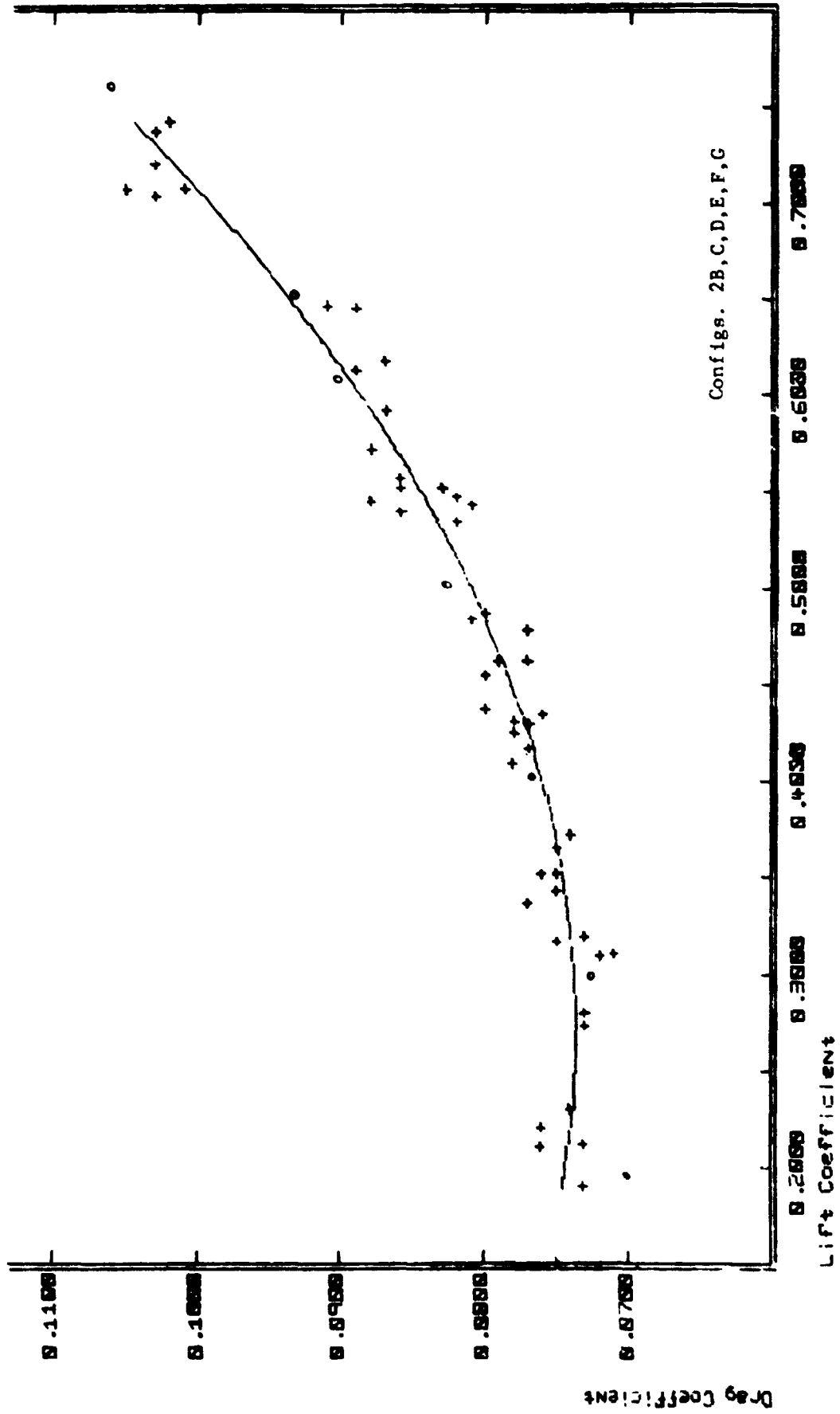
Figure 46.- Example of fitted drag data; configurations 2B,C,D,E,F,G.

$C_D \approx .073 + .138 \ (C_L - .27)^2$

Configs. 2B,C,D,E,F,G

Lift Coefficient

Drag Coefficient

$$C_D \approx .073 + .148 \ (C_L - .30)^2$$
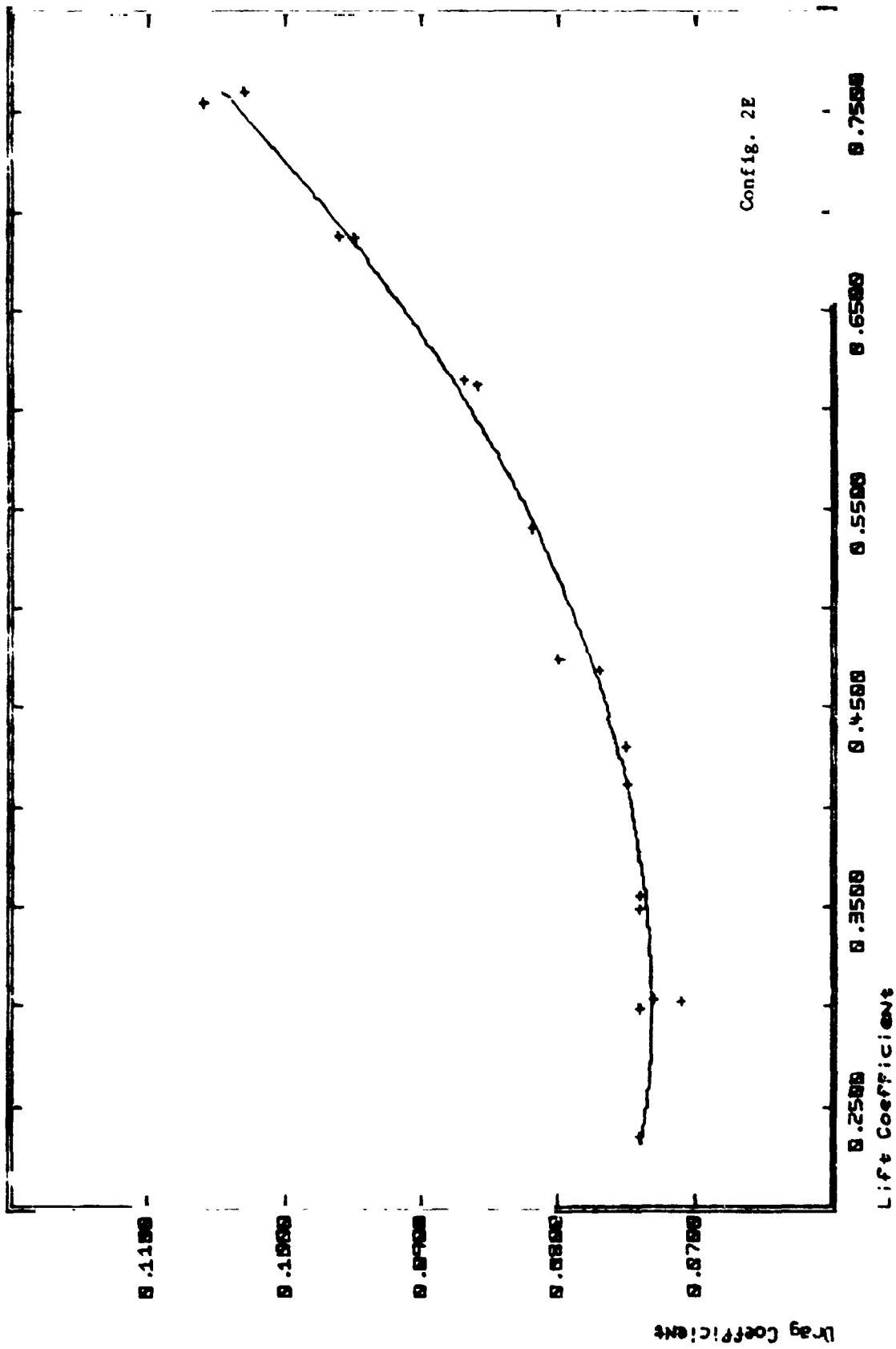
Figure 47.- Example of fitted drag results; configuration 2E.

84
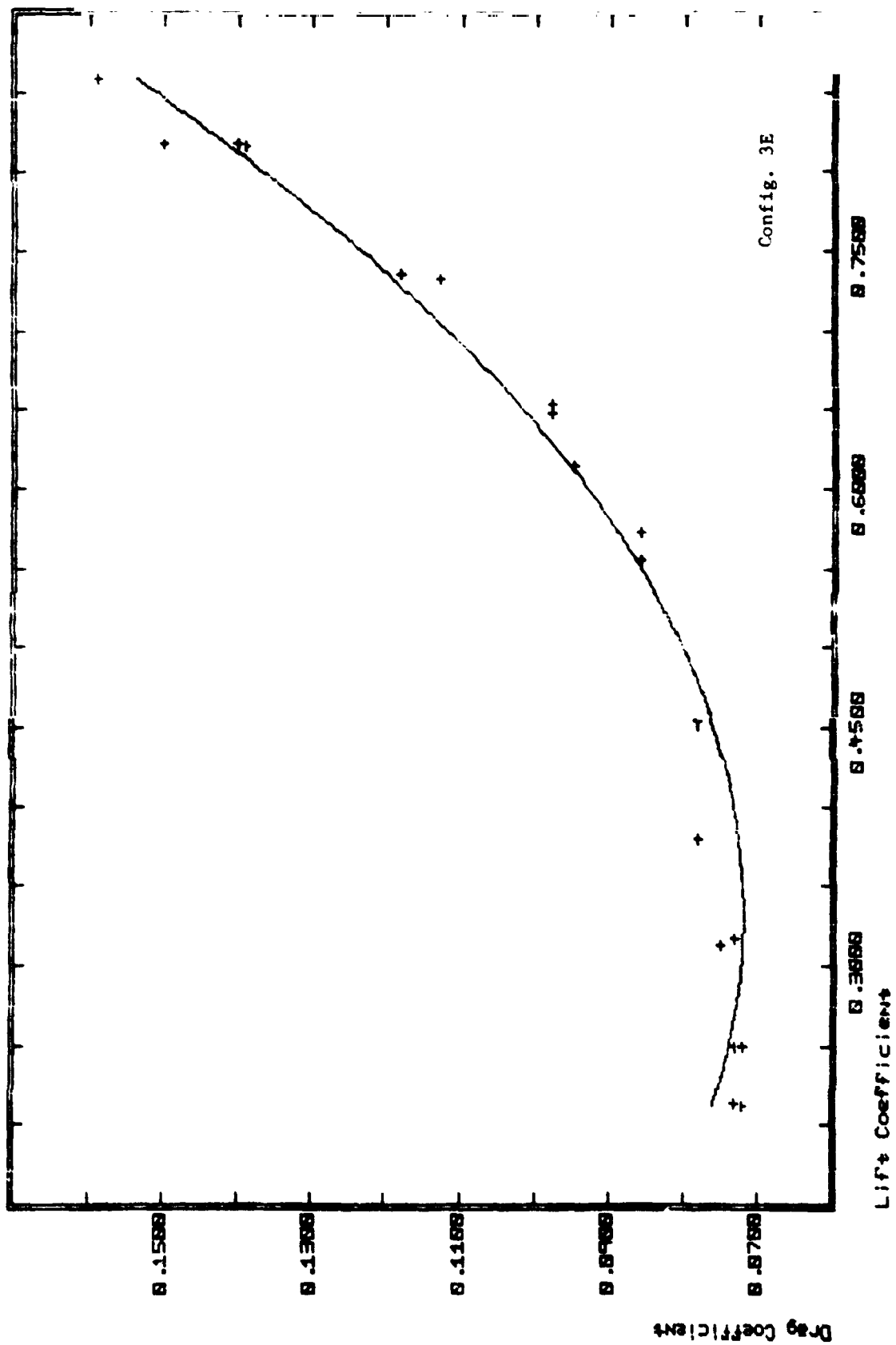
Figure 48.- Fitted drag data; configuration 3E.
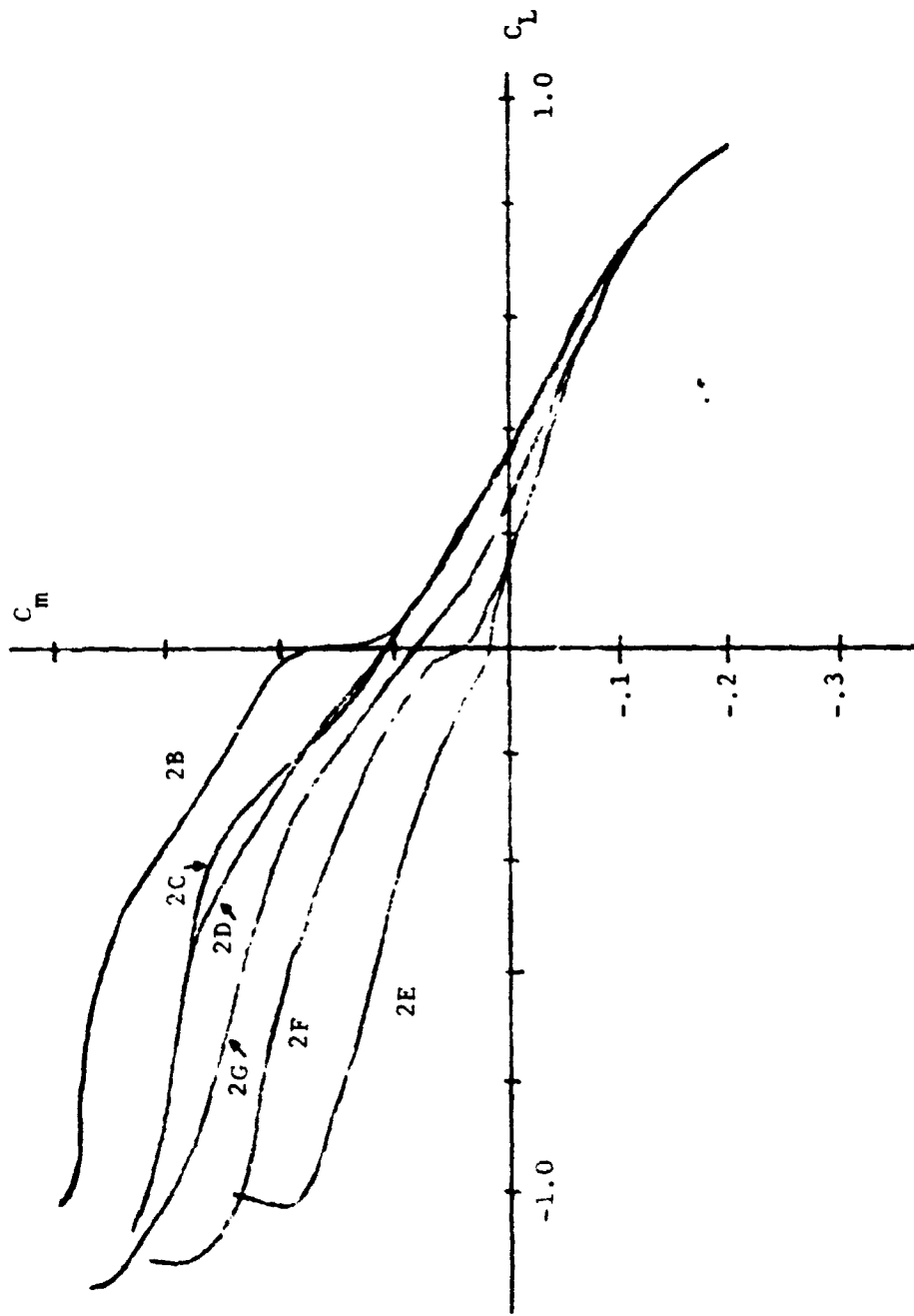
(a) Fixed tips.

Figure 49.- Effect of luff lines.
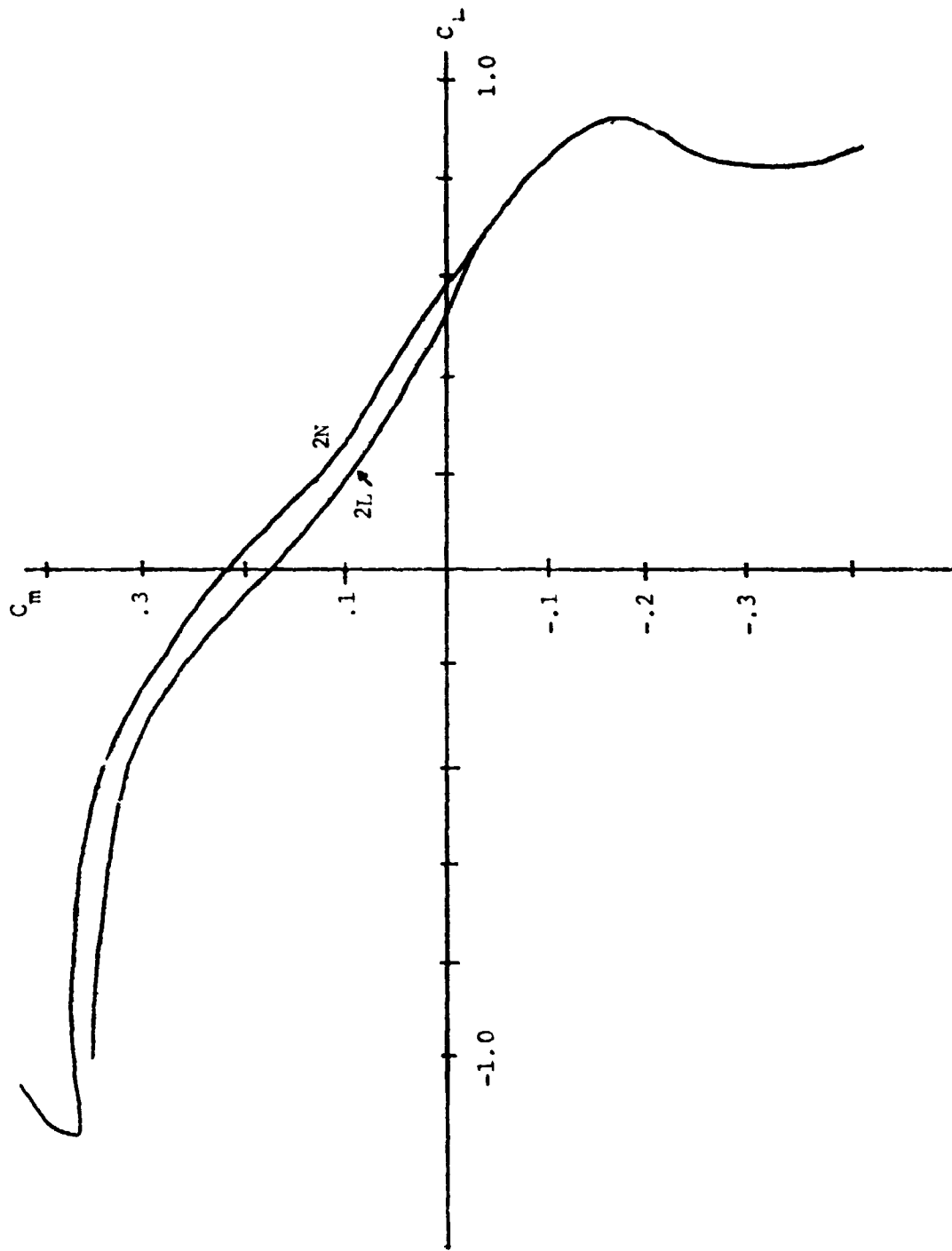
(b) Effect of "extended" luff lines.

Figure 49.- Concluded.
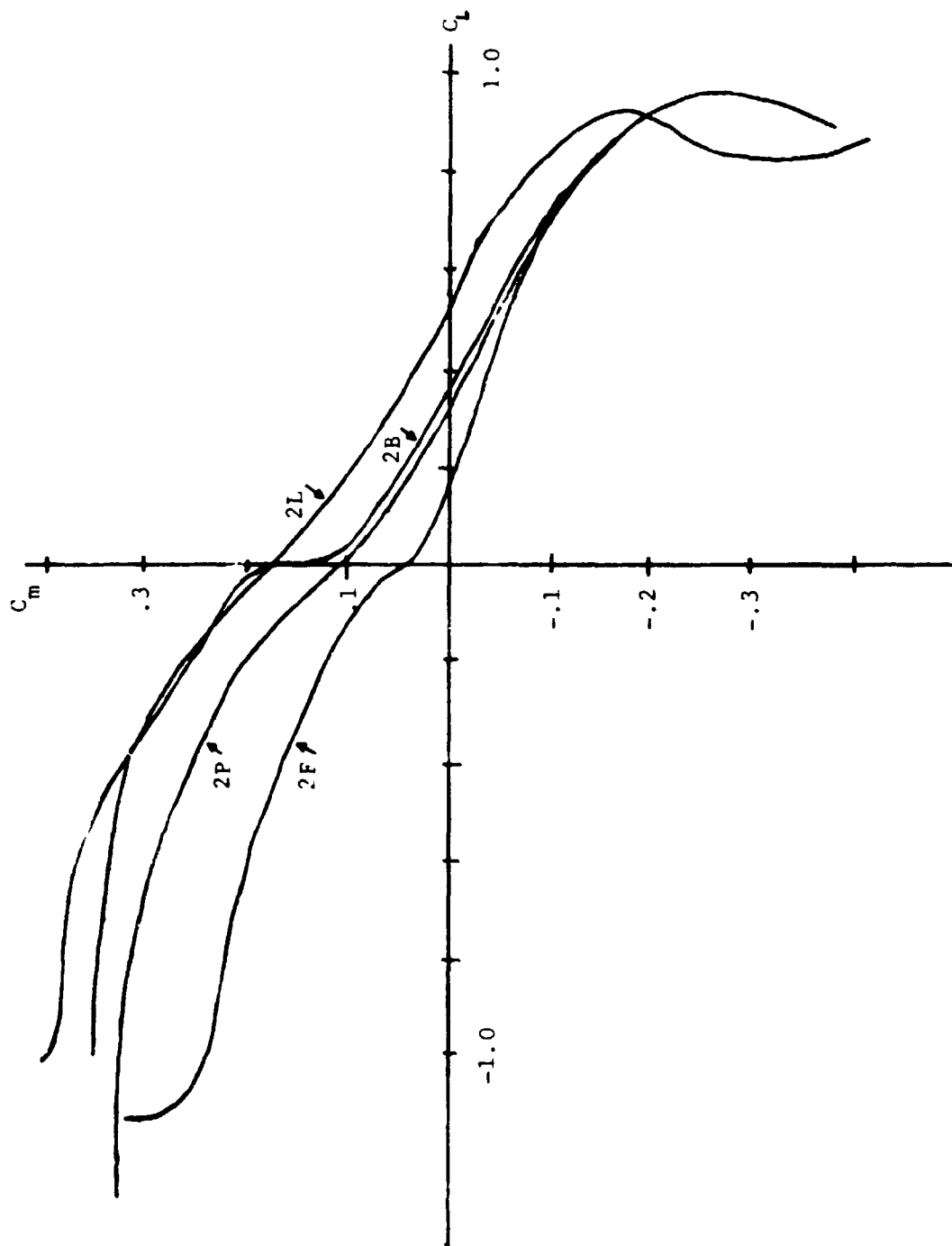
Figure 50.- Effect of fixed tips.
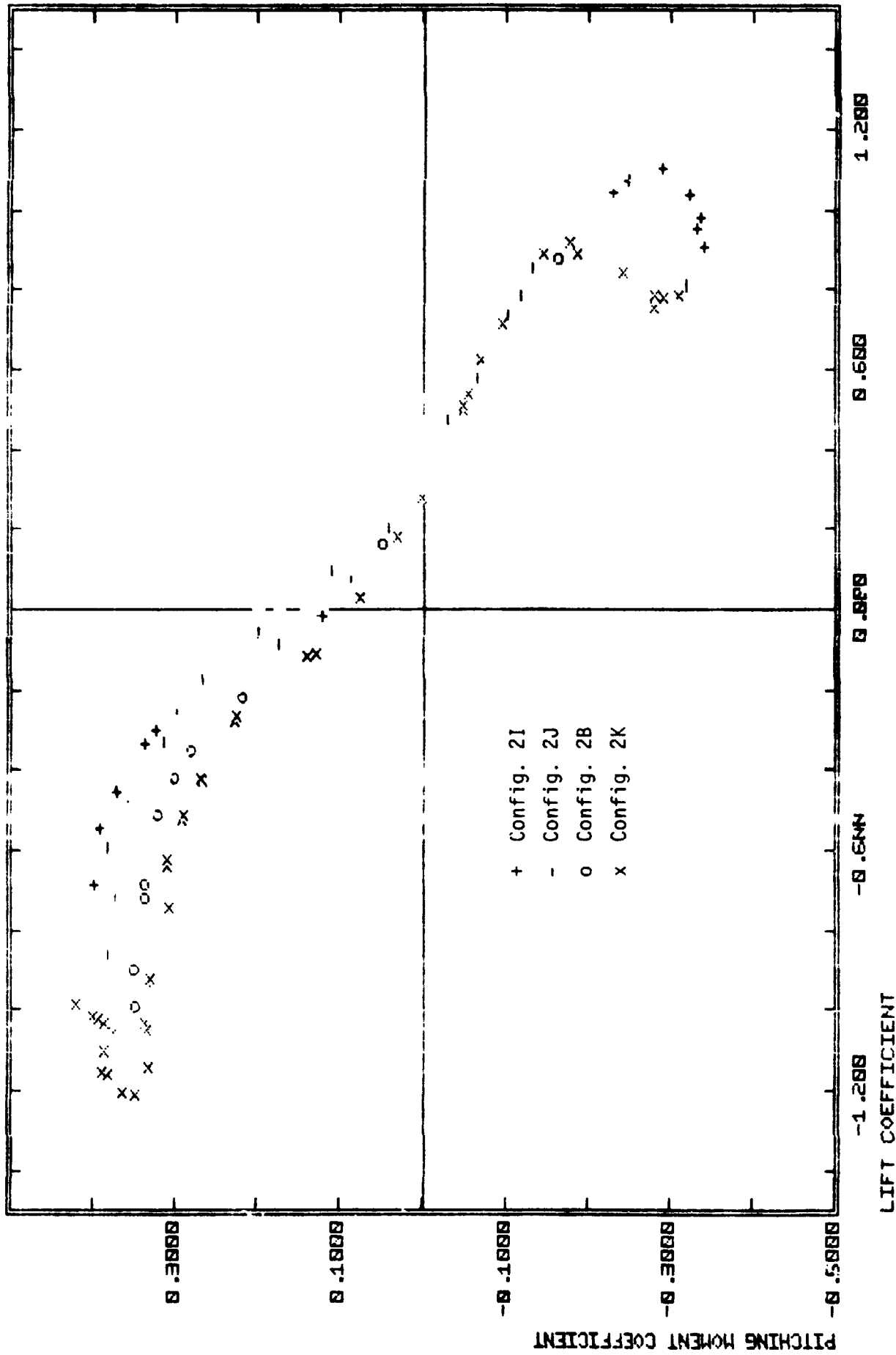
Figure 51.- Effect of batten flexibility.
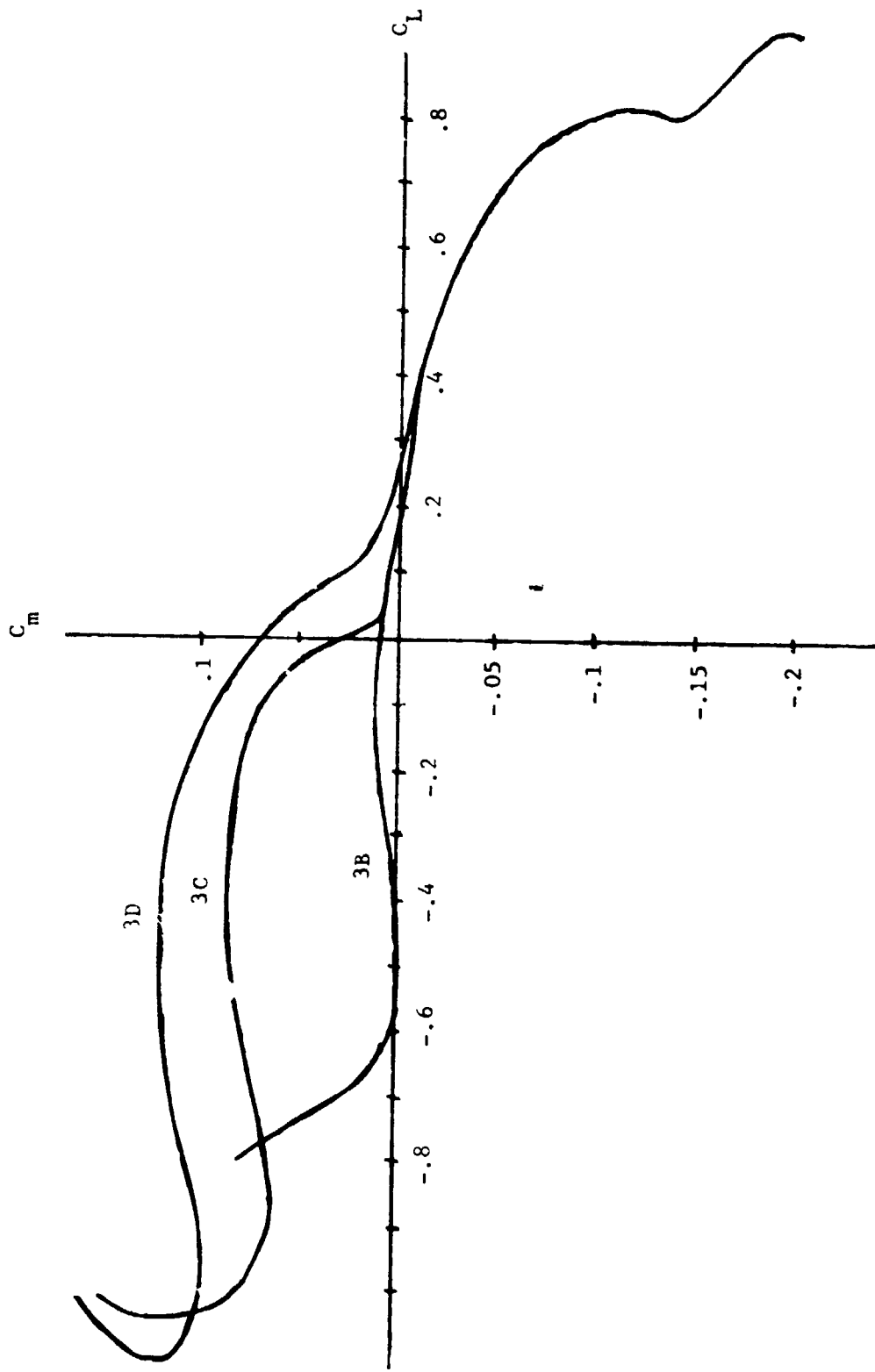
Figure 52.- Effect of luff lines with flexible (spruce) battens.
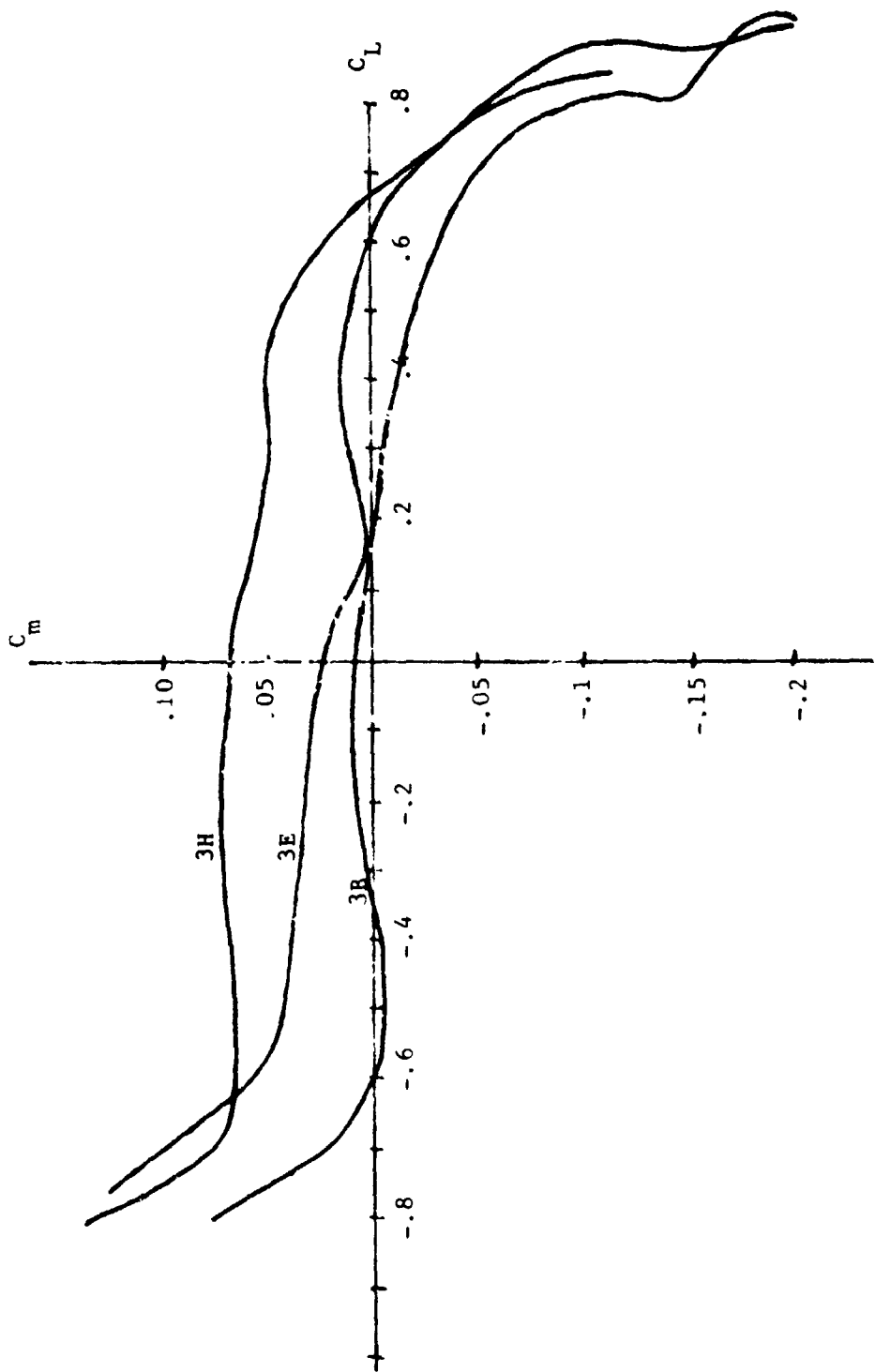
Figure 53.- Effect of batten camber.
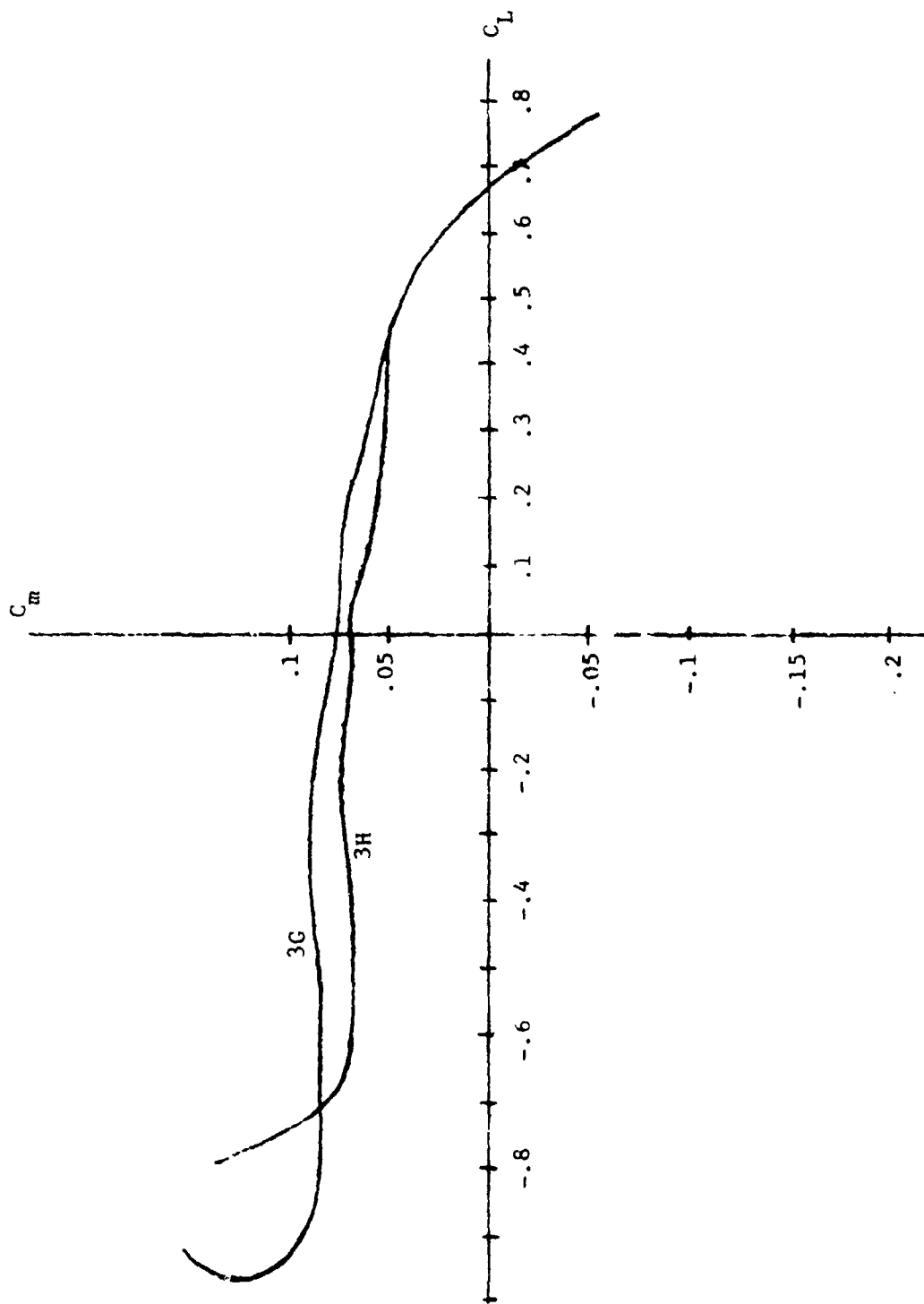
Figure 54.- Effect of luff lines on outboard battens.
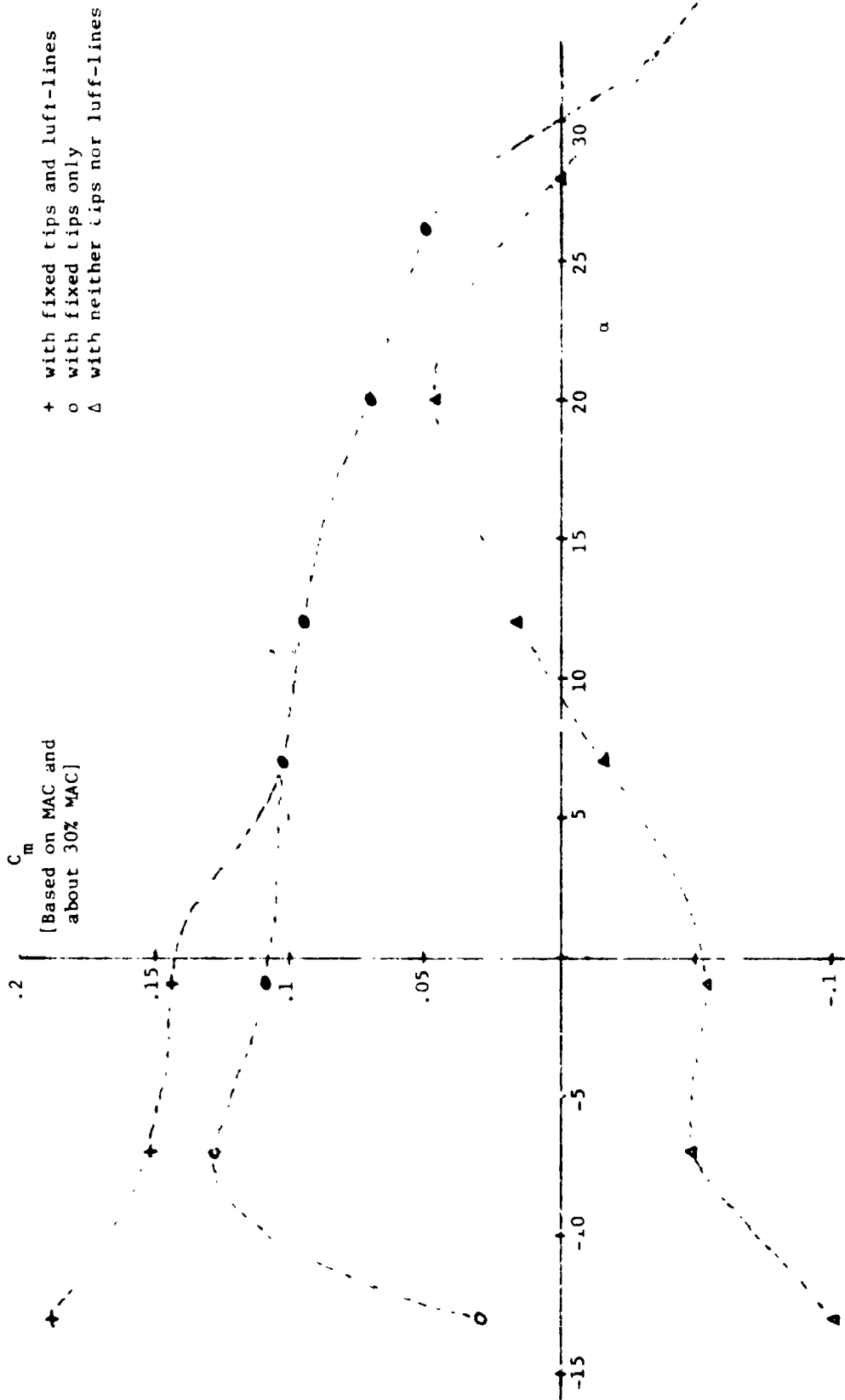
Figure 55.- Test vehicle results.

Figure 56.- Comparison of lateral data with previous work.
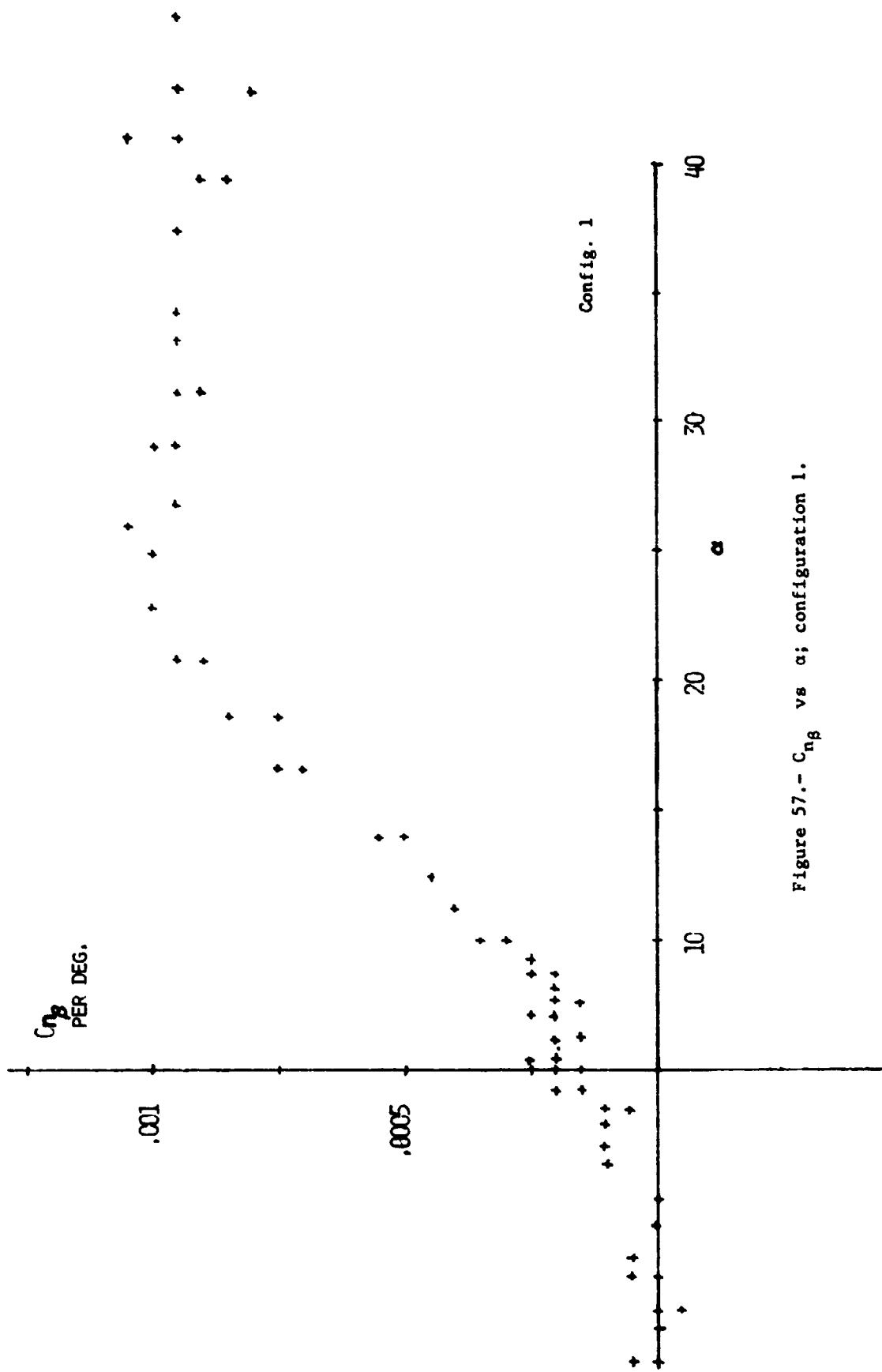
Figure 57.- C_{n_β} vs α; configuration 1.

Figure 58.- C_{l_β} vs α; configuration 1.

Config. 1

Figure 59.- C_{n_β} vs α; configuration 2A.

97
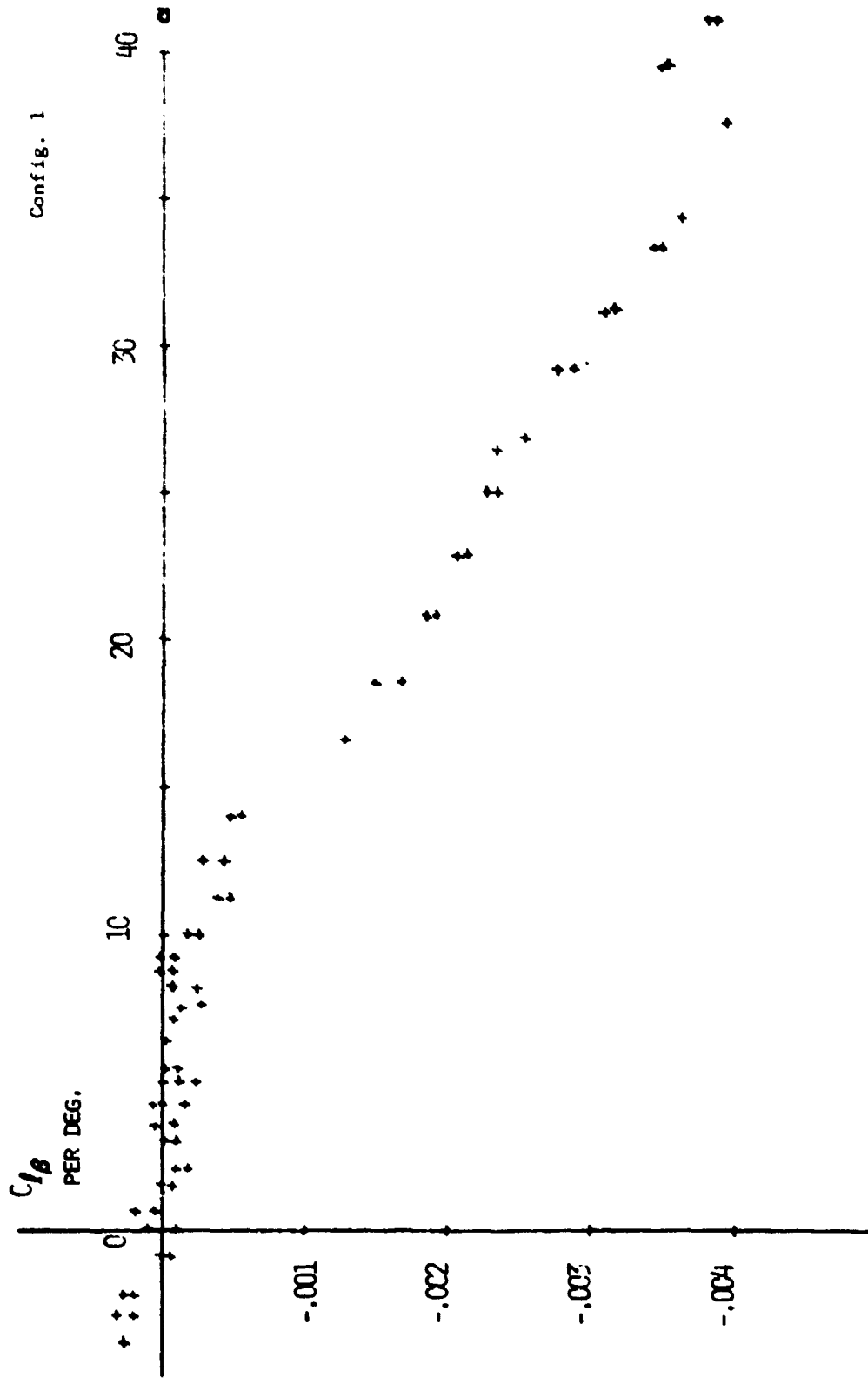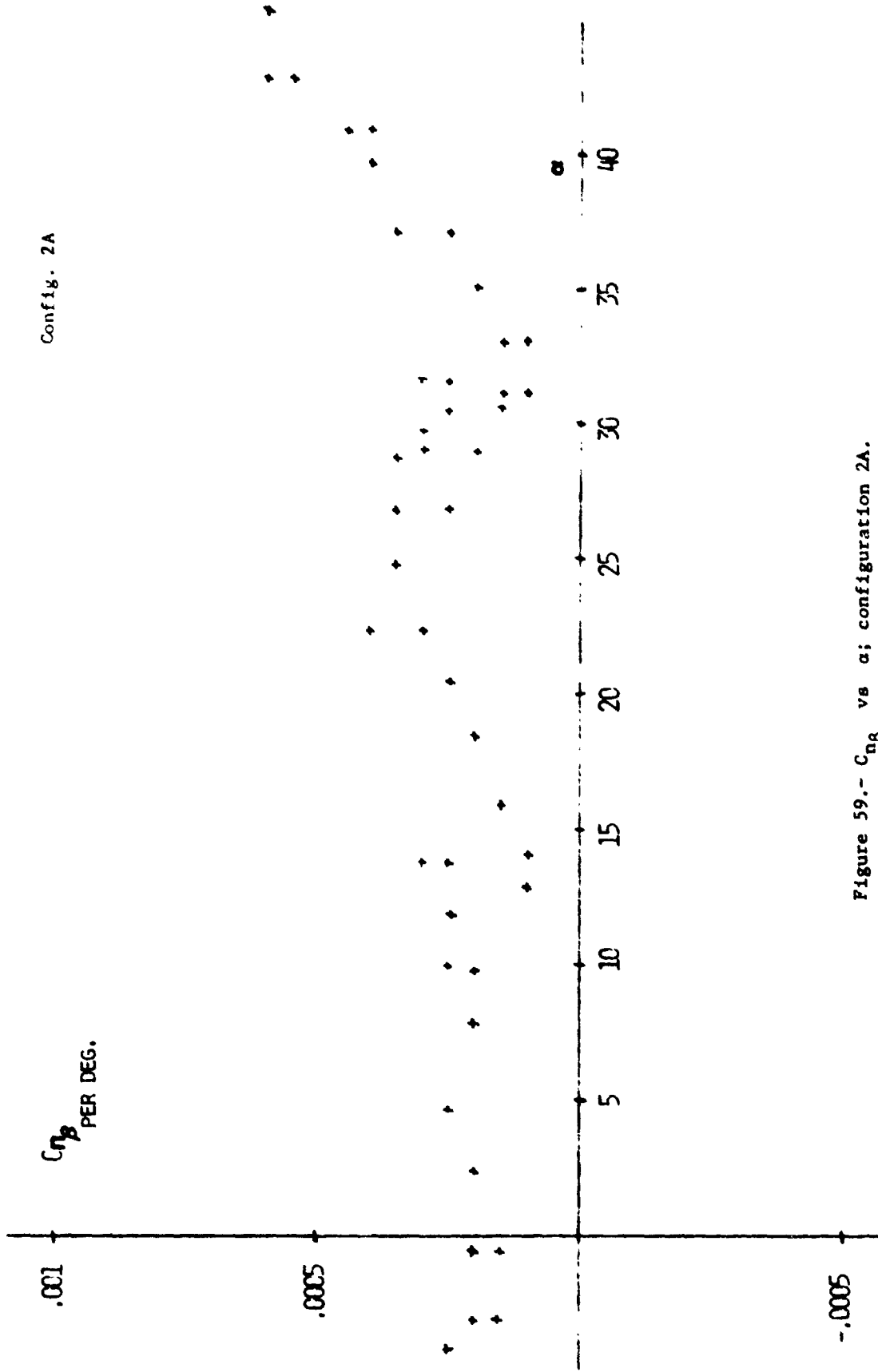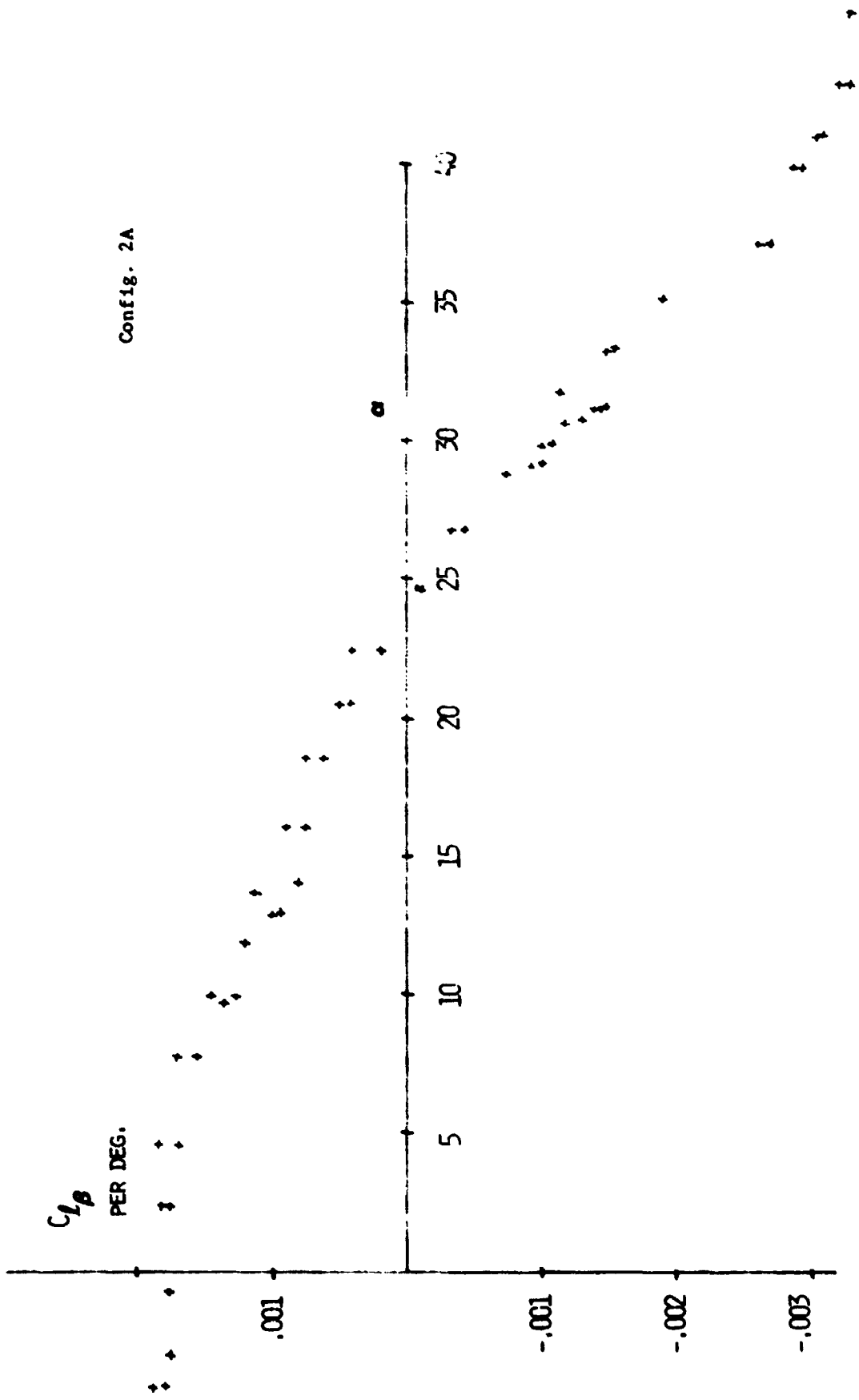
Figure 60.- C_{l_β} vs α; configuration 2A.
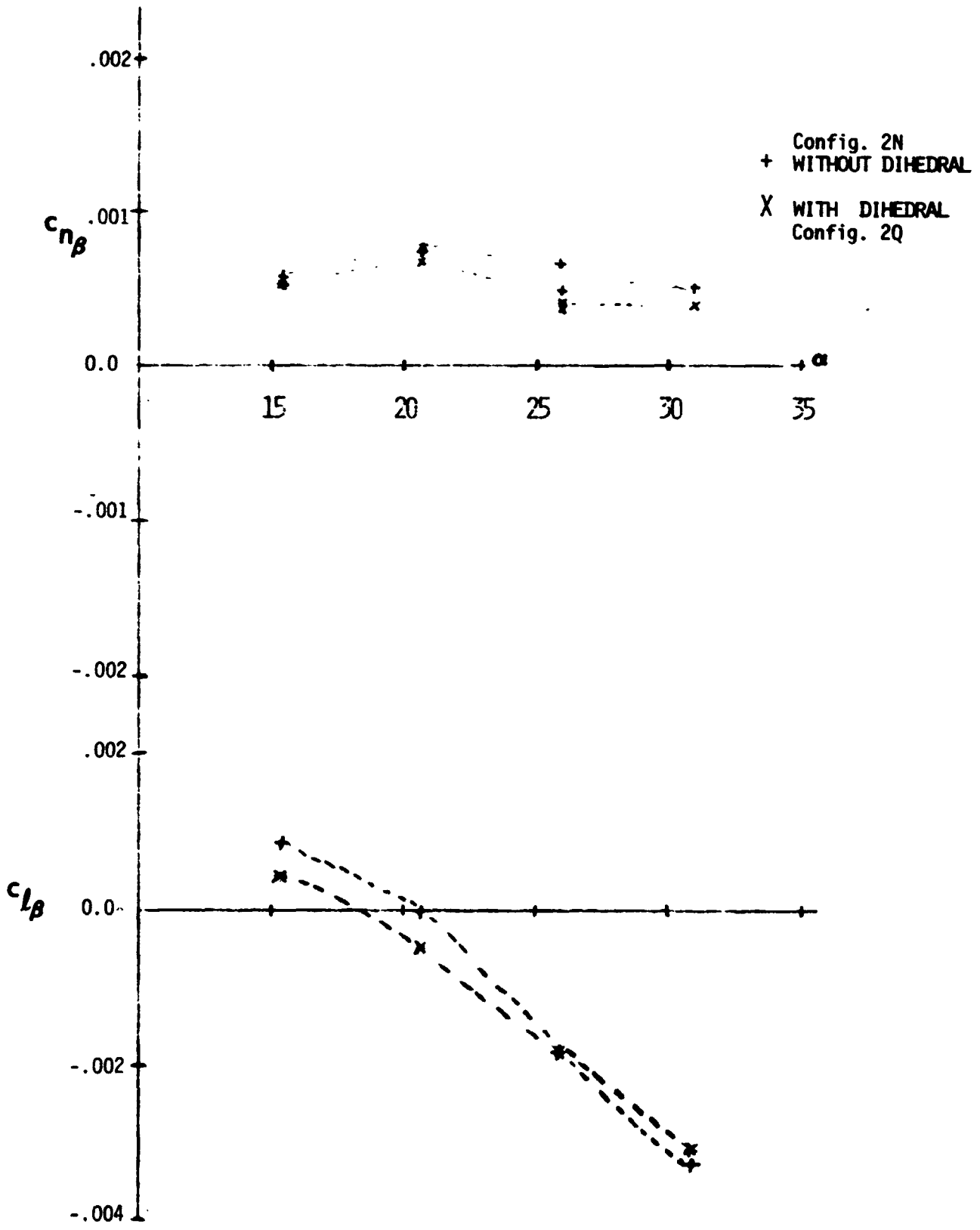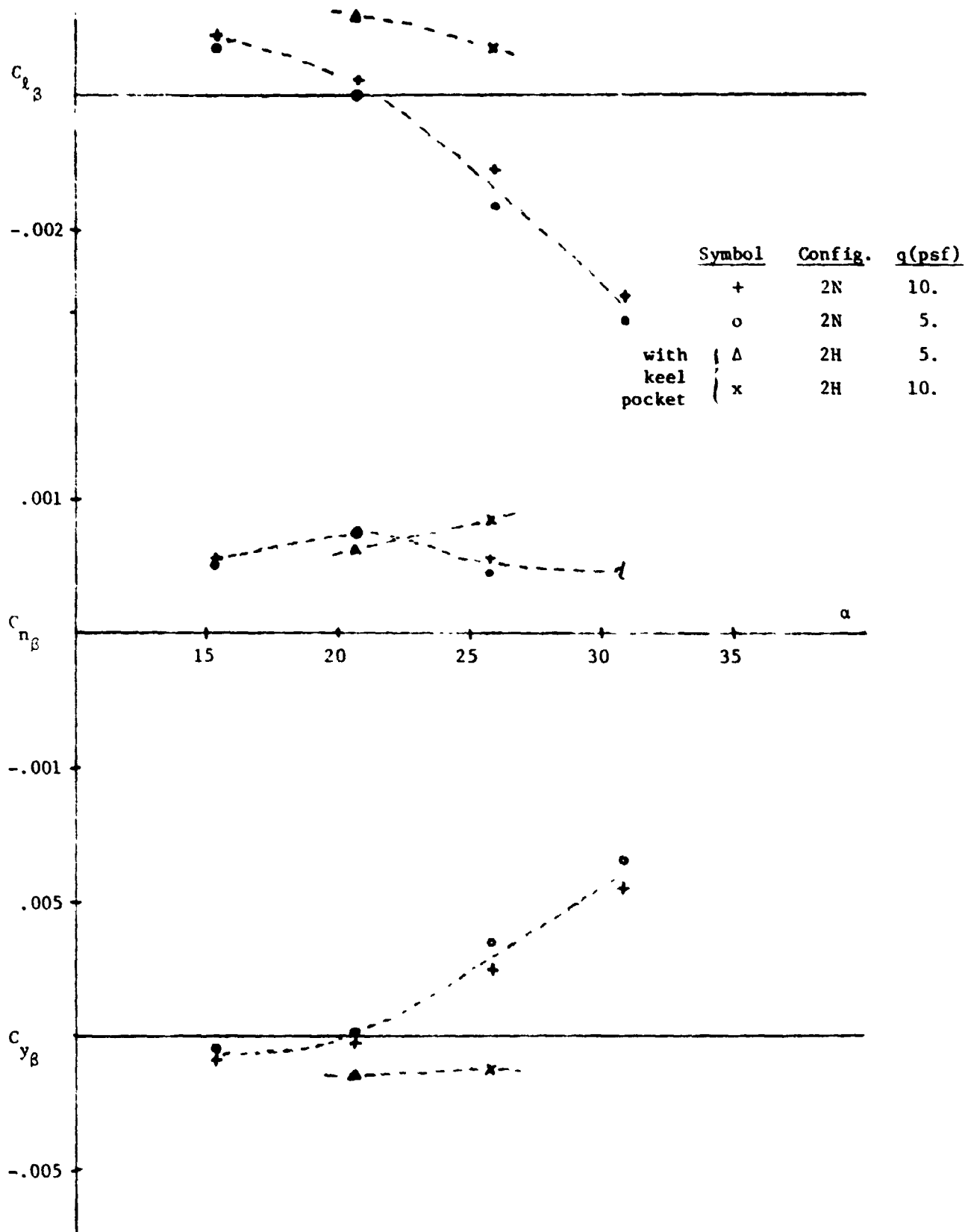
Figure 61.- Effect of dihedral on lateral derivatives.

Figure 62.- Effect of keel pocket on lateral characteristics. (Derivatives from yaw sweeps.)
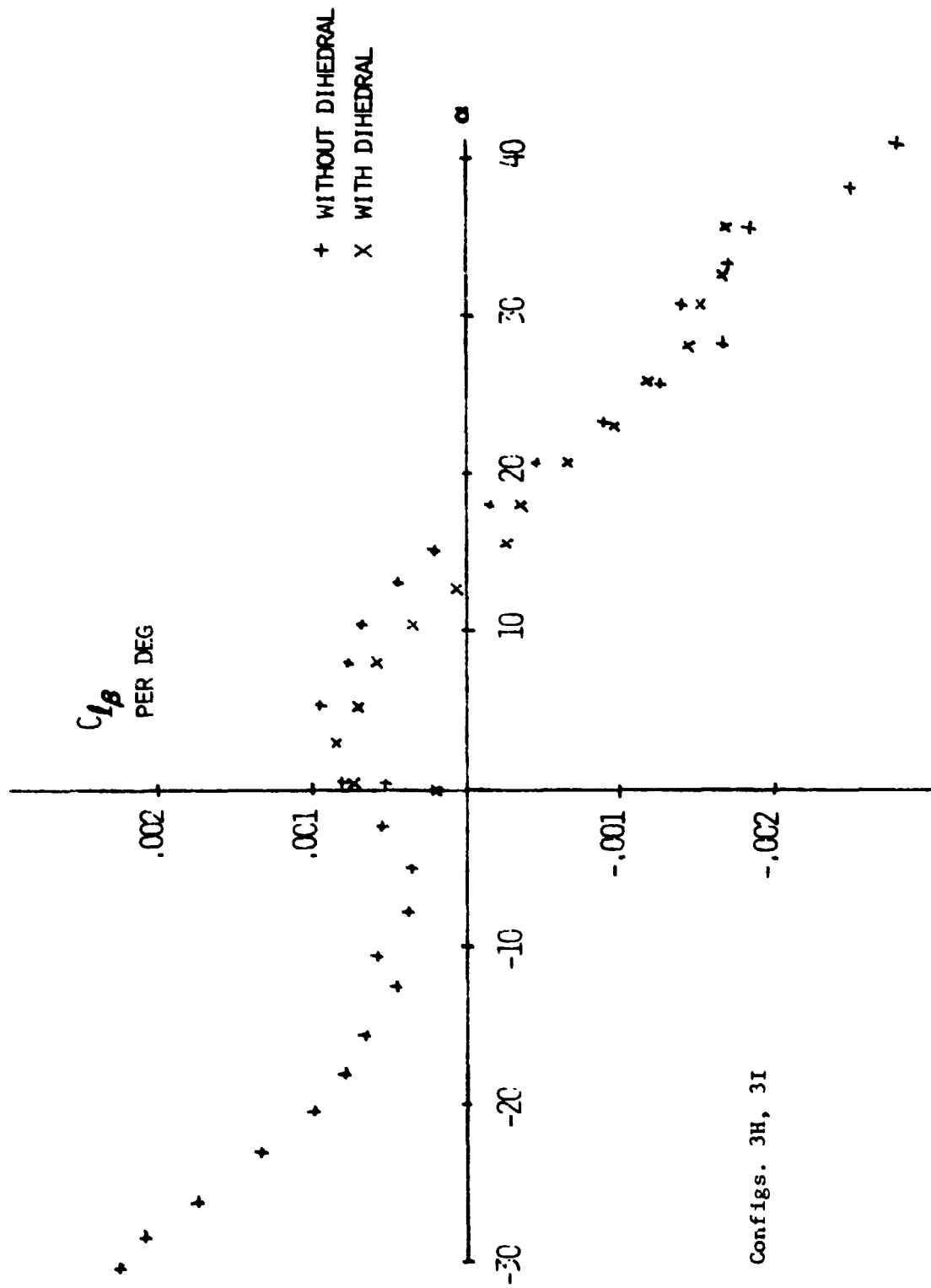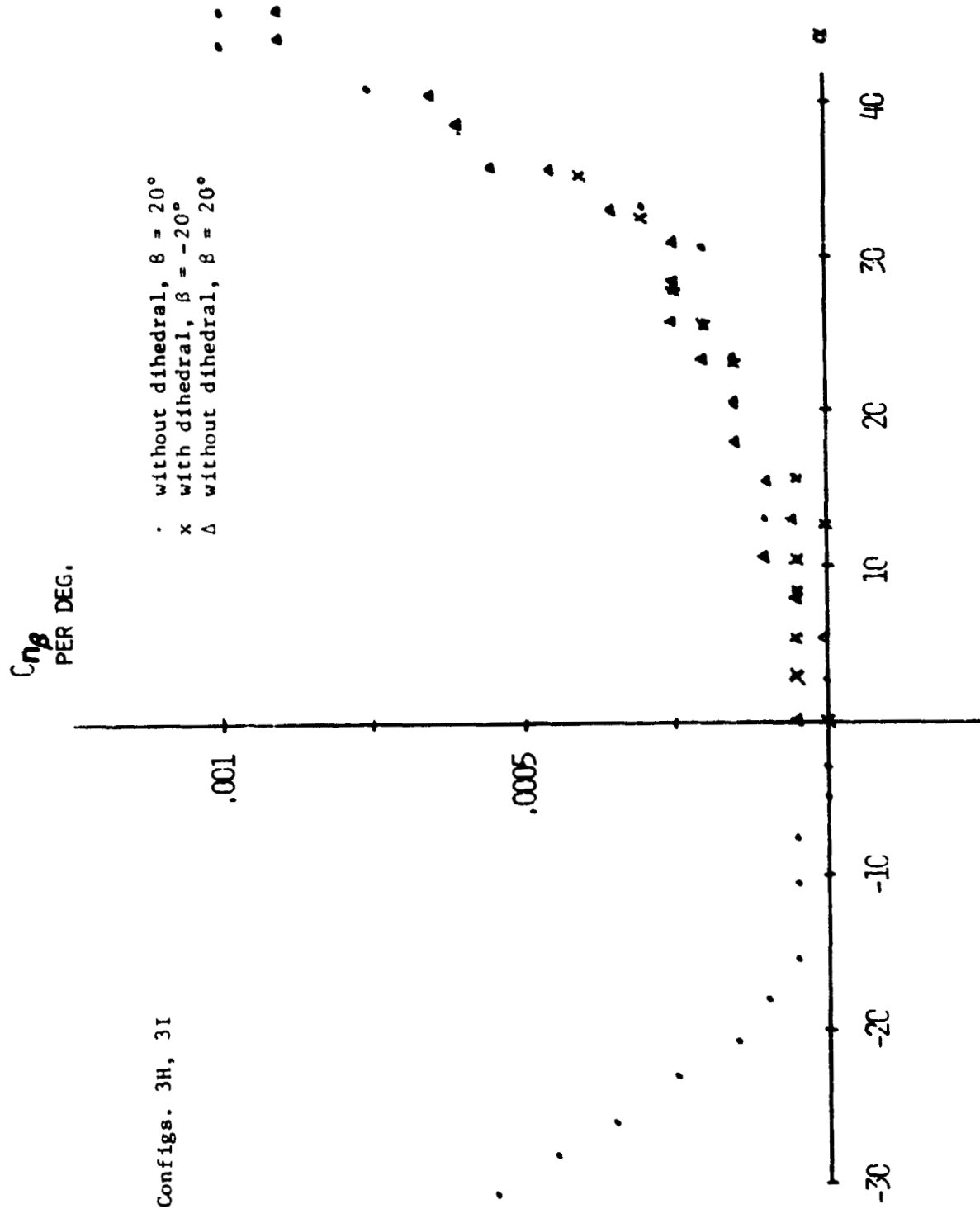
Figure 63.- C_{ℓ_β} vs α.

Configs. 3H, 3I

Figure 64.– C_{n_β} vs α.

Configs. 3H, 3I

Legend:
- without dihedral, $\beta = 20°$
- × with dihedral, $\beta = -20°$
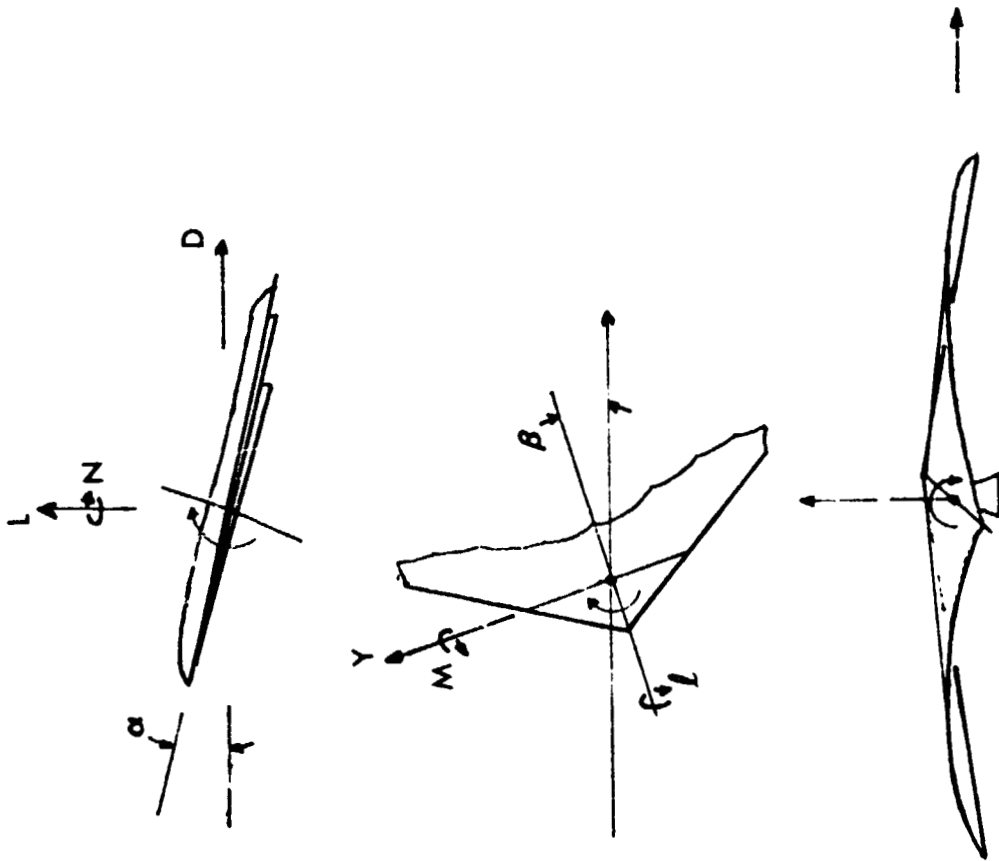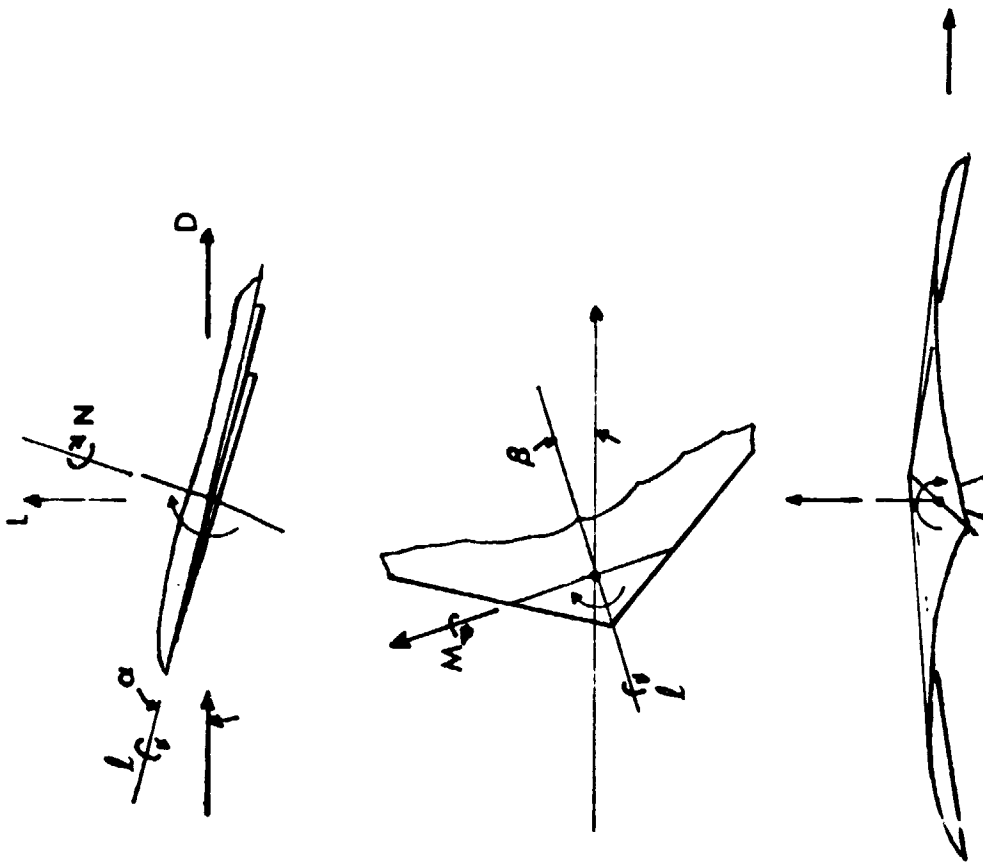- △ without dihedral, $\beta = 20°$

C_{n_β} PER DEG.

Figure 65.- Stability axes system.

103

Figure 66.- Body axes system.